jacking system control strategies

during the seabed penetration phase
of a wind turbine installation vessel

tom scheeper

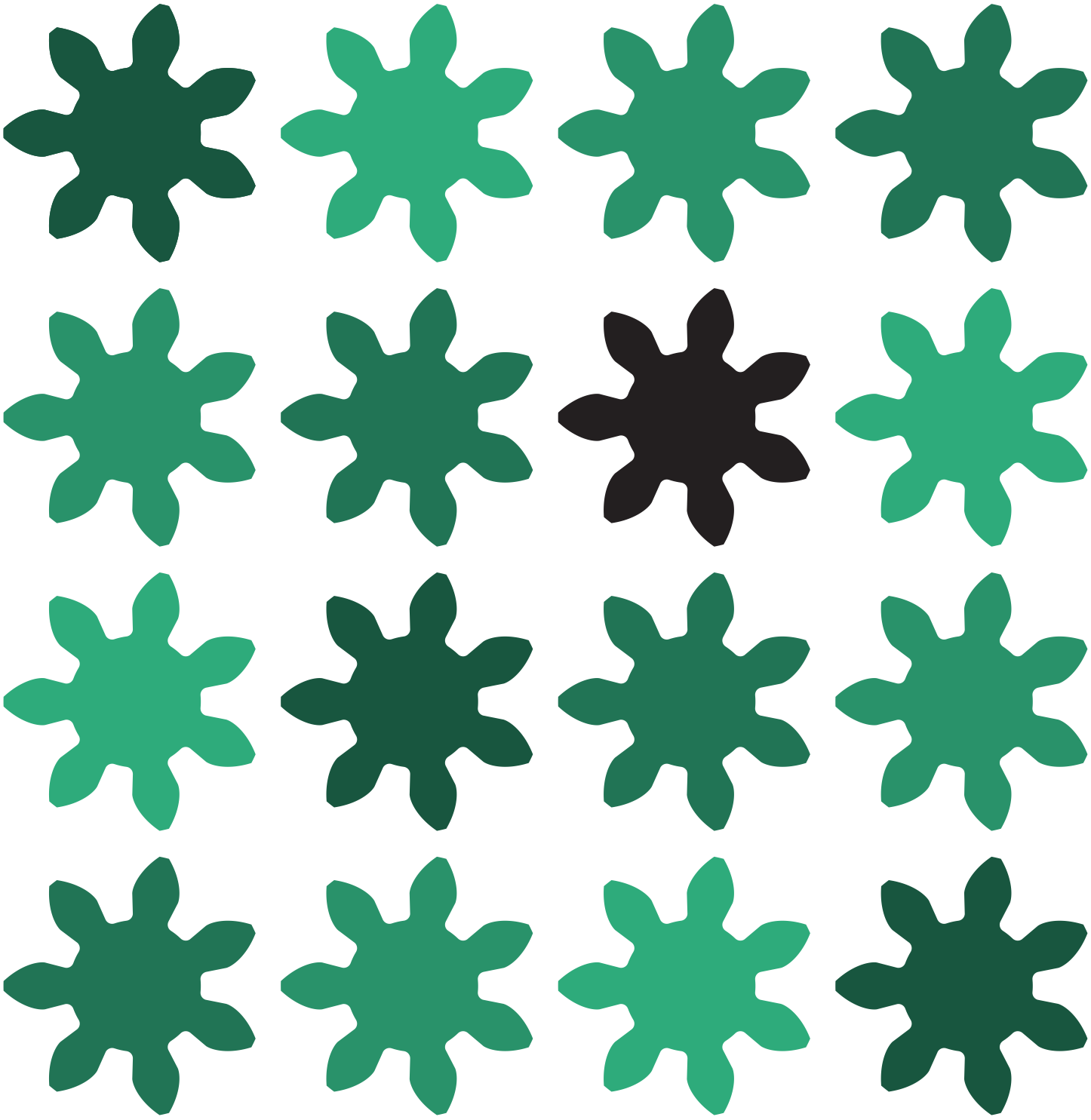

Technische Universiteit Delft

Master's Thesis

Jacking system control strategies

during the seabed penetration phase of a wind turbine installation vessel

A Thesis submitted in partial fulfilment of the requirements for the degree of

Master of Science

in Offshore and Dredging Engineering at

Technische Universiteit Delft

to be publicly defended on Friday 27 October 2023 at 15:00 by

Tom Scheeper

student number 4553055

Graduation committee

Member	Function	Representing
dr.ir. A. Tsouvalas	chair	TU Delft
dr.ir. P.C. Meijers	supervisor	TU Delft
ir. J. van Lammeren	supervisor	GustoMSC - NOV
dr.ir. S.P. Mulders	advisor	TU Delft

TU Delft

GustoMSC | NOV

Sailin' away on the crest of a wave, it's like magic

Jeff Lynne

Preface

This thesis is publicly available via the Delft University of Technology repository. As such, information, data and methods deemed confidential by the research partner GustoMSC, have been omitted in this publication. Certain sections and paragraphs are therefore not publicly available as well as for certain figures, the vertical axis has been omitted.

Acknowledgements

This thesis is written to conclude the Master Offshore and Dredging Engineering, specialisation Structural Design and Analysis at the Delft University of Technology. This graduation assignment is performed in corporation with GustoMSC.

I would like to extend my gratitude towards the members of the graduation committee who have helped me throughout the process. First and foremost, Jasper van Lammeren, my daily supervisor at GustoMSC with whom I weekly discussed the progress and results of the thesis. Our discussion on the model helped me greatly with the interpreting and understanding the results. I also would like to thank my daily supervisor at the TU Delft, Peter Meijers, for providing me with feedback on the report and the simulation model. I also would like to extend my gratitude towards Apostolos Tsouvalas for chairing my graduation committee and providing critical feedback during progress meetings and Sebastiaan Mulders for helping me with understanding and tuning of control systems.

I also want to acknowledge the help of my colleagues at GustoMSC. Most notably Sander Baars for helping me in understanding the dynamics and control systems of jacking systems, Raluca Toma for helping me with the seabed model and Andries Hofman for providing me with this interesting graduation assignment. My gratitude also goes out to Peter Naaijen of the TU Delft, who helped with the hydrodynamics and recommended the use of Python package `Capytaine`.

Lastly, I want to thank my parents for their continued support during my graduation, my sisters for their patience in conversations on my graduation topic and my friends to ensure not all times are spent working on this report.

Tom Scheeper
Den Haag, October 2023

Abstract

Wind turbine installation vessels (WTIVs) are ships that are specifically designed to install offshore wind turbines. These WTIVs have four or six large truss-like legs that are lowered towards the seabed by means of jacking systems. These jacking systems are regulated by control systems to ensure the leg is lowered with a constant velocity regardless of external disturbances. The bottom of these legs are outfitted with spudcans, which have a conical shape to allow for penetration into the seabed. When these spudcans have settled in the seabed, the hull is lifted above the waves. Consequently, wave-exciting forces on the hull are prevented and the motions of the hull are near-zero so that the on-board crane can perform the installation operations with minimised disturbances.

The objective of this thesis is to develop and analyse a model that is able to describe and simulate the dynamics of these jacking systems in great detail in response to external loads and the dynamics of the WTIV. The control systems of the jacking systems are included in this model to simulate and evaluate the interaction between the control system and the dynamics of the WTIV. Two conventional control systems are considered: the Volts-per-Hertz (V/Hz) and the direct torque control (DTC) method. In the process of lowering the legs and subsequent platform lifting, a transient phase can be identified during which the spudcans are penetrating the seabed. Due to the periodical motions of the ships, multiple impacts with the seabed are expected. Additionally, the jacking systems and the leg undergo a change of load direction as initially the leg is in tension and the jacking systems are generating power, and afterwards the leg is in compression and the jacking systems are consuming power. This thesis is focused on this seabed penetration phase as this phase introduces complicated dynamics. In literature, no model is available that has the abilities to simulate the WTIVs and its jacking systems with control systems in such level of detail.

This research gap is addressed by developing such a simulation model. This model is written in Python and developed using finite element (FE) techniques and solved using numerical time integration. Seabed characteristics are derived using a detailed coupled Eulerian-Lagrangian (CEL) FE models. Multiple control strategies are simulated and evaluated, each differentiating how the velocity and torque setpoints of the jacking systems are calculated. From the simulation model, it is found that in order to achieve load sharing between jacking systems, torque and velocity require to be independently controlled which only the DTC method has the ability to. Furthermore, each of the jacking systems should be provided with its own power supply. Best performance and stability was achieved when each chord of the leg is given a common torque and velocity setpoint, which is equivalent to a common torque and setpoint per leg in reality. Moreover, load sharing can be improved without a control system by increasing the relative stiffness ratio between the chord and the mechanical contact between rack and pinion.

Table of contents

Preface vi

Acknowledgements vii

Abstract viii

Table of contents ix

List of figures xii

List of tables xiv

List of abbreviations xv

List of definitions xvi

List of symbols xvii

I Introduction 1

1 Introduction 3
- 1.1 The need, design and function of wind turbine installation vessels . . . 3
  - 1.1.1 The need for wind turbine installation vessels . . . 4
  - 1.1.2 The design of wind turbine installation vessels . . . 4
  - 1.1.3 The design and function of jacking systems . . . 5
  - 1.1.4 The design of rack-and-pinion jacking systems . . . 6
  - 1.1.5 The complicated dynamics in jacking systems . . . 7
- 1.2 Problem statement . . . 7
- 1.3 Research objective . . . 8
- 1.4 Scope of this thesis . . . 9
- 1.5 Structure of the thesis . . . 9

II Literature research 11

2 A general procedure to model the dynamics of structures 13
- 2.1 Discretisation of structures into finite elements . . . 13
- 2.2 The equation of motion . . . 14
- 2.3 Structural elastic forces . . . 14
- 2.4 Structural inertia forces . . . 15
  - 2.4.1 Consistent element mass matrix . . . 15
  - 2.4.2 Lumped element mass matrix . . . 16
- 2.5 Structural damping forces . . . 16
- 2.6 External forces . . . 16
- 2.7 Procedures to represent a structure with multiple beam elements . . . 17
  - 2.7.1 Composition of the global vectors and matrices . . . 17
  - 2.7.2 Transformation for elements with an arbitrary orientation . . . 17
- 2.8 Procedures to solve the equation of motion . . . 19

3 Modelling the dynamics of wind turbine installation vessels 21
- 3.1 Discretisation of wind turbine installation vessels . . . 21
  - 3.1.1 Discretisation of the legs . . . 21
  - 3.1.2 Discretisation of the hull . . . 22
- 3.2 Structural elastic forces . . . 22
  - 3.2.1 Structural elastic forces of the legs . . . 22

3.2.2 Structural elastic forces of the hull . . . 24
3.2.3 Force transfer between the leg and hull . . . 24
3.2.4 Force transfer between the spudcan and seabed . . . 25
3.3 Structural inertia forces . . . 26
3.4 Structural damping forces . . . 26
3.5 Environmental actions . . . 26
3.5.1 Metocean data . . . 27
3.5.2 Wave actions on legs . . . 27
3.5.3 Wave actions on hull . . . 28

4 Modelling and regulating the dynamics of three-phase induction machines 31
4.1 Electric machines and three-phase induction machines . . . 31
4.1.1 Difference between electric machines, motors and generators . . . 31
4.1.2 The design of electric machines . . . 31
4.1.3 Alternating-current electric machines . . . 32
4.1.4 Three-phase power electronics . . . 33
4.2 Dynamics of three-phase squirrel-cage induction machines . . . 35
4.3 The need, design and function of control systems . . . 36
4.3.1 The need for control systems . . . 36
4.3.2 The design of control systems . . . 37
4.3.3 The function of control systems or control laws . . . 39
4.4 Control systems of induction machines . . . 42

III Simulation model 43

5 A detailed description and derivation of the simulation model 45
5.1 Top level description of the simulation model . . . 45
5.2 Detailed description and derivation of the simulation model . . . 45
5.2.1 Sea model . . . 46
5.2.2 Hull model . . . 46
5.2.3 Leg model . . . 47
5.2.4 Leg-and-hull interface . . . 50
5.2.5 Spudcan-and-seabed interface . . . 50
5.3 Implementation of control systems into the simulation model . . . 50

6 Results of the simulation model 51
6.1 Global dynamics of the simulation model . . . 51
6.1.1 Global dynamics of the the hull . . . 51
6.1.2 Global dynamics of the leg . . . 52
6.1.3 Seabed reaction forces . . . 54
6.1.4 Leg bending moment . . . 54
6.2 Dynamics of the jacking systems . . . 55
6.3 Sensitivity of the model to parameters changes . . . 55

IV Discussion and conclusion 57

7 Discussion and recommendations 59
7.1 The sea model . . . 59
7.2 Wind turbine installation vessel design: hull and leg . . . 59
7.3 The spudcan-and-seabed model . . . 60
7.4 The control systems . . . 60

8 Conclusion 62

References **63**

V Appendices **67**

A Derivation of the element matrices **69**
A.1 Derivation of the element stiffness matrix . . . 69
A.2 Derivation of the consistent element mass matrix . . . 72

B Model methodology **76**
B.1 Modelling philosophy . . . 76
B.2 The software of the simulation model . . . 76
B.3 Running the simulation . . . 78

C Validation of the model **80**
C.1 Validation of the internal FE model . . . 80
C.1.1 Validation of the element mass and element stiffness matrices . . . 80
C.1.2 Validation of the procedure to represent a structure with multiple beam elements . . . 80
C.2 Validation of the induction motor model . . . 80
C.2.1 Validation of the equation of motion of the induction motor . . . 80
C.2.2 Validation of the induction motor parameters . . . 82
C.3 Validation of the internal BEM model . . . 82

List of Figures

1.1 Historic development of wind capacity installations. Created with data from Hutchinson & Zhao (2023) . . . 3
1.2 Schematic overview of main components of a WTIV . . . 5
1.3 Overview of leg-handling operations involving the jacking system in chronological order . . . 5
1.4 Design and function of pin-and-yoke jacking systems . . . 6
1.5 Design of a rack-and-pinion jacking system . . . 6
1.6 Transfer of leg bending moment M to the hull via force couples and the resulting RPD . . . 7

2.1 Overview of the procedure to model the dynamics of structures . . . 13
2.2 Three types of one-dimensional elements and their nodal displacements . . . 14
2.3 Three methods to map the external forces onto the nodes with decreasing accuracy . . . 17
2.4 Principle of superposition to obtain the global matrices . . . 17
2.5 Definition of the local X-axis . . . 19
2.6 Two equally valid orientations of the local cross-section . . . 19

3.1 Levels of complexity of leg discretisation . . . 22
3.2 Levels of complexity of hull discretisation . . . 22
3.3 The P-δ effect: increasing deformations due to axial loads . . . 23
3.4 Relative importance of $P-\delta$ effects as function of load ratio q^2 . . . 24
3.5 Principle of superposition applied to evaluate wave actions on hull . . . 29

4.1 General design of an electric machine . . . 31
4.2 Single-phase AC electricity . . . 32
4.3 Three-phase AC electricity . . . 32
4.4 Torque-velocity or torque-slip characteristics of induction machines . . . 32
4.5 Three-phase rectifier circuit with inductive filter . . . 34
4.6 DC voltage output from three-phase rectifier . . . 34
4.7 Three-phase inverter circuit with switch state 101 . . . 34
4.8 Comparison between reference and carrier signal . . . 34
4.9 Resulting state of the switch in the inverter . . . 34
4.10 Three-phase switch states . . . 35
4.11 Three-phase phase-to-phase voltage . . . 35
4.12 Three-phase phase-to-neutral voltage . . . 35
4.13 Clarke's transformation from abc to $\alpha\beta$ . . . 36
4.14 General design of an induction machine . . . 36
4.15 General design of control systems . . . 37
4.16 General design of closed-loop control systems . . . 38
4.17 Influence of control systems on inherently unstable systems . . . 39
4.18 Influence of control systems on inherently stable systems . . . 39
4.19 Equivalent open-loop control system . . . 40
4.20 Influence of the type of PID-controller on a step response for a mass-spring-damper system . . . 41
4.21 Characteristics of the response of a control system . . . 41

5.1 Three-dimensional overview of the model including its global coordinate system . . . 45
5.2 Two-dimensional overview of the model showing the sub-models . . . 45
5.3 Overview of the sea model and its parameters . . . 46
5.4 Model of the barge with the Capytaine package . . . 47
5.5 General design and parameter definition of the leg for $n_{\text{bay}} = 4$ . . . 48
5.6 First six modes of the leg and their natural frequencies . . . 50

6.1 Surge of the hull . . . 51

6.2 Heave of the hull . . . 51
6.3 Pitch of the hull . . . 51
6.4 Yaw of the hull . . . 51
6.5 Heave of the leg nodes . . . 52
6.6 Downwards vertical leg extension . . . 52
6.7 Three-dimensional time-trace of the position of the legs . . . 53
6.8 Axial loads of the chords . . . 53
6.9 Surge of the spudcan . . . 54
6.10 Surge reaction force of the seabed . . . 54
6.11 Heave of the spudcan . . . 54
6.12 Heave reaction force of the seabed . . . 54
6.13 Roll leg-bending moment m_x . . . 55
6.14 Pitch leg-bending moment m_y . . . 55

7.1 Difference in chord and leg loads between this simulation model and reality . . . 59
7.2 Difference between an inverter frequency of 5000 Hz (left) and 25 000 Hz (right) . . . 61

B.1 Structure and flow of the Python code of the model . . . 78

C.1 Electromagnetic torque generated by the induction motor, and the external load . . . 81
C.2 Motor velocity in rpm. Slight drop in velocity visible due to the external load . . . 81
C.3 Currents in the rotor . . . 81
C.4 Currents in the stator . . . 81
C.5 Torque-velocity characteristics during the change in external load . . . 81
C.6 Diagonal terms of the added mass matrix $\mathbf{M}_\mathrm{h}$ . . . 82
C.7 Diagonal terms of the damping matrix $\mathbf{C}_\mathrm{h}$ . . . 82
C.8 Wave-exciting force amplitudes $\mathbf{f}_\mathrm{h}$ . . . 82

List of Tables

1.1 Qualitative comparison between WTIVs of type jack-up and floating 4
1.2 Design considerations for WTIVs 4

5.1 Parameters of the sea model 46
5.2 Parameters of the hull 47
5.3 Parameters of the general leg design 48
5.4 Parameters of structural steel used for the leg 49
5.5 Parameters of the chord design 49

B.1 Overview of software used 77
B.2 Overview of Python packages used 77
B.3 Overview of settings for the simulation procedure 78

C.1 Overview of the validation methods of sub-models 80
C.2 Induction motor parameters (Krause et al., 2013) 82

List of abbreviations

AC alternating current.

BEM boundary element method.

CEL coupled Eulerian-Lagrangian.

CSI current source inverter.

DC direct current.

DOF degrees of freedom.

DTC direct torque control.

EOM equation of motion.

FE finite element.

LCOE levelised cost of electricity.

LTI linear time-invariant.

ODE ordinary differential equation.

PID proportional integral derivative.

PWM pulse-width modulation.

RPD rack phase difference.

V/Hz Volts-per-Hertz.

VSI voltage source inverter.

WTIV wind turbine installation vessel.

List of definitions

capex Capital expenditures: costs of initialising a project.

dynamic positioning A system of thrusters overseen by a control system that provide active station keeping of a vessel.

fixation system Mechanical interface between the leg and the hull that transfers horizontal and vertical forces, used as a mechanical brake to prevent motion of the legs.

guide Mechanical interface between the leg and the hull that transfers horizontal forces.

ide Integrated Development Environment: application for software development; editing, debugging and running.

jack-up A vessel consisting of a hull and at least three legs (in practice three, four, six, eight) capable of elevating itself above the waterline by means of a jacking system.

jacking system Mechanical interface between the leg and the hull that transfers vertical forces and is responsible for leg-handling: leg lowering and lifting, pre-loading, and platform lowering and lifting.

metocean A set of meteorological and oceanographic characteristics of an area at sea, like water depth, wave height or wind velocity that describe to describe the weather and sea state.

opex Operational expenditures: costs of operating, maintaining and repairing a project.

spudcan Conical structure attached to the bottom of the legs that penetrates the seabed to provide firm foundation and stability.

stationkeeping Maintaining a fixed position of a vessel on water, often done by means of mooring or dynamic positioning systems.

List of symbols

Roman scalars

Symbol	Description	Unit
a_0,a_1	coefficients for Rayleigh damping	s^{-1} or s
A	(cross-sectional) area	m^2
A_s	shear area	m^2
b	width	m
d	water depth	m
D	diameter	m
E	Young's modulus	$N\,m^{-2}$
f	force	N
g	gravitational acceleration	$m\,s^{-2}$
G	shear modulus	$N\,m^{-2}$
h	height	m
H	wave height	m
H_s	significant wave height	m
$i_{\alpha r}$,$i_{\beta r}$	rotor currents in the $\alpha\beta$ reference frame	A
$i_{\alpha s}$,$i_{\beta s}$	stator currents in the $\alpha\beta$ reference frame	A
I	second moment of area	m^4
j	mass moment of inertia	$kg\,m^2$
J	torsion constant	m^4
K	wave number	$rad\,m^{-1}$
K_p,K_i,K_d	proportional, integral and derivative gains for PID-controller	N/A
l	length	m
L_m	mutual inductance between the rotor and the stator	H
L_r,L_s	self-inductance of the rotor and the stator	H
m	mass	kg
n	number of	-
p	number of poles	-
r	radius	m
R	resistance	Ω
R_r,R_s	resistance of the rotor and the stator	Ω
s	slip	-
t	time	s
T	wave period	s
T_{moor}	mooring period	s
T_n	natural period	s
T_p	wave peak period	s
u,v,w	nodal translational displacements in global directions x, y and z	m
$\bar{u}$,$\bar{v}$,$\bar{w}$	element translational displacements in global directions x, y and z	m
v_{as},v_{bs},v_{cs}	stator voltage in the *abc* reference frame	V
v_{DC}	DC voltage	V
$v_{\alpha s}$,$v_{\beta s}$	stator voltage in the $\alpha\beta$ reference frame	V
V	volume	m^3
x,y,z	coordinates in the global coordinate system	m
X,Y,Z	coordinates in the element coordinate system	m

Greek scalars

Symbol	Description	Unit
α_h	wave phase	rad
β	ratio of bending moment transferred by the jacking system	-
ζ	damping ratio	-
ϑ,φ,ψ	nodal rotational displacements around global directions x, y and z	rad
ϑ_mr	rotor mechanical angular displacement	rad
Θ	shear correction factor	-
ν	Poisson's ratio	-
ρ	density	$\mathrm{kg\,m^{-3}}$
ρ_w	water density	$\mathrm{kg\,m^{-3}}$
τ	torque	$\mathrm{N\,m}$
τ_im	induction machine electromagnetic torque	$\mathrm{N\,m}$
φ_h	wave potential function	$\mathrm{m^2\,s^{-1}}$
ψ_h	wave direction	rad
ω	angular frequency	$\mathrm{rad\,s^{-1}}$
ω_e	electrical angular frequency	$\mathrm{rad\,s^{-1}}$
ω_h	wave angular frequency	$\mathrm{rad\,s^{-1}}$
ω_mr	rotor mechanical angular frequency	$\mathrm{rad\,s^{-1}}$
ω_n	natural frequency	$\mathrm{rad\,s^{-1}}$
ω_rr	rotor electrical angular frequency	$\mathrm{rad\,s^{-1}}$

Roman vectors

Symbol	Description	Unit
$\hat{\mathbf{e}}_\mathrm{X}$,$\hat{\mathbf{e}}_\mathrm{Y}$,$\hat{\mathbf{e}}_\mathrm{Z}$	unit vectors expressing element coordinate system XYZ in global coordinates xyz	m
$\mathbf{f}$	force vector	N
$\mathbf{f}_\mathrm{e}$	element force vector	N
$\mathbf{f}_\mathrm{w}$	gravity force vector	N
$\mathbf{f}_\mathrm{h}$	hydrodynamic force vector	N
$\mathbf{f}_\mathrm{rg}$	rack-and-guide interface force vector	N
$\mathbf{f}_\mathrm{rp}$	rack-and-pinion interface force vector	N
$\mathbf{f}_\mathrm{n}$	nodal force vector	N
$\mathbf{f}_\mathrm{ss}$	spudcan-and-seabed interface force vector	N
$\hat{\mathbf{i}}$,$\hat{\mathbf{j}}$,$\hat{\mathbf{k}}$	unit vectors of global coordinate system xyz	m
$\mathbf{i}_{\alpha\beta\mathrm{r}}$	rotor current vector in the $\alpha\beta$ reference frame	A
$\mathbf{i}_{\alpha\beta\mathrm{s}}$	stator current vector in the $\alpha\beta$ reference frame	A
$\mathbf{q}$	eigenvector	m or rad
$\mathbf{u}$	fluid velocity field	$\mathrm{m\,s^{-1}}$
$\mathbf{u}_\mathrm{h}$	wave-induced fluid velocity field	$\mathrm{m\,s^{-1}}$
$\mathbf{u}_\mathrm{n}$	normal fluid velocity vector normal in global coordinate system xyz	$\mathrm{m\,s^{-1}}$
$\mathbf{u}_\mathrm{N}$	normal fluid velocity vector normal in element coordinate system XYZ	$\mathrm{m\,s^{-1}}$
$\mathbf{v}_\mathrm{abcs}$	stator voltage vector in the *abc* reference frame	V
$\mathbf{v}_{\alpha\beta\mathrm{s}}$	stator voltage vector in the $\alpha\beta$ reference frame	V
$\mathbf{x}$	displacement vector	m
$\dot{\mathbf{x}}$	velocity vector	$\mathrm{m\,s^{-1}}$
$\ddot{\mathbf{x}}$	acceleration vector	$\mathrm{m\,s^{-2}}$

Greek vectors

Symbol	Description	Unit
$\boldsymbol{\varepsilon}$	strain vector	$\mathrm{m\,m^{-1}}$
$\boldsymbol{\xi}$	node unit displacement vector	m and rad
$\bar{\boldsymbol{\xi}}$	element unit displacement vector	m

Symbol	Description	Unit
$\boldsymbol{\lambda}_{\alpha\beta \mathrm{r}}$	rotor magnetic flux vector in the $\alpha\beta$ reference frame	A
$\boldsymbol{\lambda}_{\alpha\beta \mathrm{s}}$	stator magnetic flux vector in the $\alpha\beta$ reference frame	A
$\boldsymbol{\sigma}$	stress vector	$\mathrm{N\,m^{-2}}$
$\boldsymbol{\omega}_{\mathrm{n}}$	eigenfrequencies	$\mathrm{rad\,s^{-1}}$

Roman matrices

Symbol	Description	Unit
$\mathbf{C}_{\mathrm{e}}$	element structural damping matrix	$\mathrm{N\,s\,m^{-1}}$
$\mathbf{C}_{\mathrm{h}}$	hydrodynamic damping or radiation damping matrix	$\mathrm{N\,s\,m^{-1}}$
$\mathbf{C}_{\mathrm{s}}$	global structural damping matrix	$\mathrm{N\,s\,m^{-1}}$
$\mathbf{D}$	matrix relating node unit displacements $\boldsymbol{\xi}$ to element unit displacement $\bar{\boldsymbol{\xi}}$	-
$\mathbf{E}$	elasticity matrix relating stresses $\boldsymbol{\sigma}$ to strains $\boldsymbol{\varepsilon}$	$\mathrm{N\,m^{-2}}$
$\mathbf{I}$	identity matrix	-
$\mathbf{K}$	global stiffness matrix	$\mathrm{N\,m^{-1}}$
$\mathbf{K}_{\mathrm{e}}$	element structural stiffness matrix	$\mathrm{N\,m^{-1}}$
$\mathbf{K}_{\mathrm{h}}$	hydrostatic stiffness or restoring stiffness matrix	$\mathrm{N\,m^{-1}}$
$\mathbf{K}_{\mathrm{moor}}$	mooring stiffness matrix	$\mathrm{N\,m^{-1}}$
$\mathbf{K}_{\mathrm{s}}$	global structural stiffness matrix	$\mathrm{N\,m^{-1}}$
$\mathbf{M}$	global mass matrix	kg
$\mathbf{M}_{\mathrm{e}}$	element structural mass matrix	kg
$\mathbf{M}_{\mathrm{h}}$	hydrodynamic mass or added mass matrix	kg
$\mathbf{M}_{\mathrm{s}}$	global structural mass matrix	kg
$\mathbf{Q}$	matrix with as columns eigenvectors $\mathbf{q}$	$\mathrm{N\,m^{-2}}$
$\mathbf{R}$	element transformation matrix	-
$\mathbf{S}$	matrix relating node unit displacements $\boldsymbol{\xi}$ to strains $\boldsymbol{\varepsilon}$	$\mathrm{m^{-1}}$

Greek matrices

Symbol	Description	Unit
$\boldsymbol{\Lambda}$	coordinate transformation matrix	-

part I

Introduction

chapter 1

Introduction

Climate change has caused a shift from environmentally unfriendly energy sources such as oil, gas and coal, to renewable sources such as wind, solar, hydro and geothermal. Of these renewable energy sources, wind energy is a mature technology with a low levelised cost of electricity (LCOE), making it an attractive renewable energy source (Trinomics, 2020). Furthermore, wind energy is of special importance to the offshore industry, as, compared to onshore conditions, the wind energy potential is generally significantly higher offshore. The industry has seen tremendous growth in the last couple of years: from 2019 to 2022 the total worldwide capacity has doubled to a total to 64 GW and it is expected that by 2025, 25 GW of new capacity will be added every year (Hutchinson & Zhao, 2023). The historic development of both on- and offshore wind since 2001 is shown in Figure 1.1.

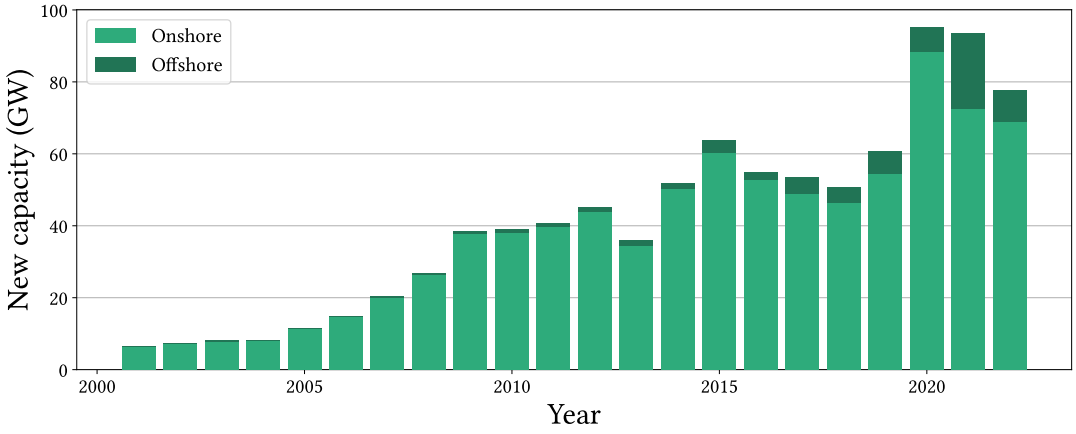

Figure 1.1: Historic development of wind capacity installations. Created with data from Hutchinson & Zhao (2023).

The first commercial offshore wind project was installed in Denmark in 1991: eleven bottom-founded 450 kW wind turbines for a total capacity of 5 MW. With a water depth of 2 m to 4 m and a distance of 1.8 km offshore, the environmental conditions for this project were, by today's standards, relatively mild (Kolios & Lozano-Minguez, 2018). Since then, bottom-founded wind turbines have grown larger in size, from 450 kW to 8 MW, and are placed further offshore in water depths of more than 60 m, as 80 % of the world's offshore wind energy potential is located there (Hutchinson & Zhao, 2023; Kolios & Lozano-Minguez, 2018). The increasing demand pushes the development for even larger wind turbines, with 20 MW turbines expected by 2030 (Hosker & Justus, 2019). Another future development is floating wind: in the last few years, floating wind has seen the first commercial implementations, with a total of 188 MW installed by 2022 (Hutchinson & Zhao, 2023). In the scope of this thesis, floating wind is not relevant as these are installed differently from bottom-founded turbines.

1.1 | The need, design and function of wind turbine installation vessels

Wind turbine installation vessels (WTIVs) are vessels that are specially designed to perform the installation of offshore bottom-founded wind turbines. This section addresses why these vessels are necessary, how they are designed and how they function.

1.1.1 ‖ The need for wind turbine installation vessels

With a higher offshore energy potential also comes an increase in wind and wave loads. Wind turbines are conventionally installed per component in situ; the supporting structure, the tower, the nacelle and the blades are separately lifted in place. Crane ships that lift these components into place need not be hindered by these environmental conditions. WTIVs are vessels that are specially designed for this operation. Conventionally these are jack-ups designs, meaning that the hull is lifted out of the water to minimise wave-exciting loads. Recent developments have also seen floating WTIVs, which uses dynamic positioning to minimise the motions of the ship (Buitendijk, 2022). They differ in design philosophy: whereas the former prevents wave loads, the latter mitigates them. Comparison between the capabilities of these two systems is shown in the table below.

Table 1.1: Qualitative comparison between WTIVs of type jack-up and floating (IMCA, n.d.).

Criterion	Jack-up	Floating
Manoeuvrability	-	+
Water depth	+	+
System complexity	+	-
Station keeping performance	+	-
Speed of setting up	-	+
Capex and opex	+	-
Maintenance frequency	+	-

Floating WTIVs can effectively operate in infinitely deep waters whereas jack-ups are limited to about 175 m (Boswell, 2018). Nevertheless, as the supporting structures of bottom-founded offshore wind turbines are limited to 70 m, both types of WTIV perform equally well in the water depth criterion. Overall jack-ups are more reliable, more cost-effective, require less maintenance and are a well-established design, and are therefore preferred by the industry.

1.1.2 ‖ The design of wind turbine installation vessels

The jack-up WTIVs (hereinafter referred to as *WTIVs*) are vessels with legs that are lowered towards the seabed allowing the hull to be lifted out of the water, so that installation can proceed with minimal interference of waves. This is made possible by jacking systems which are actuators that displace the legs. The bottom of these legs are outfitted with spudcans that penetrate the seabed to provide a stable foundation. There are a few design considerations to take into account for WTIVs, as listed in Table 1.2. The most notable design consideration is the geometry of the legs, which are large cylindrical pillars or truss-like structures.

Table 1.2: Design considerations for WTIVs.

Design consideration	Cylindrical legs	Truss legs
number of legs	three or more	three or more
jacking system	rack-and-pinion or pin-and-yoke	rack-and-pinion
number of chords	N/A	three to four
pinion configuration	radial	opposed or radial
fixation system	yes or no	yes or no
water depth	up to 100 m	up to 200 m

GustoMSC has been one of the leading designers of jack-up type vessels since the 1950s. In the last century, numerous three-legged jack-ups for oil and gas drilling have been designed and GustoMSC has been credited with ground-breaking innovations such as the fixation system (Suyderhoud & Vleugels, 2016). Since the 2000s there has been a shift to design WTIVs intended for offshore renewable energy.

Recent WTIV designs of GustoMSC have triangular truss legs, due to their reduced weight and application in deeper waters. At least three legs are required for stability, but four are chosen so that operations can be performed more efficiently. A schematic overview of a WTIV design is shown in Figure 1.2.

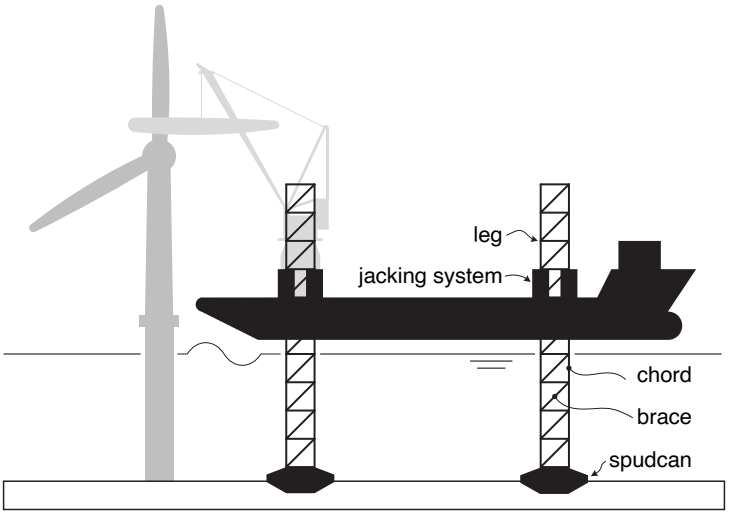

Figure 1.2: Schematic overview of main components of a WTIV.

1.1.3 ‖ The design and function of jacking systems

The jacking systems are the key to the operation of WTIVs. It is responsible for vertically moving the legs relative to the hull, so that operations can proceed. Operations involving the jacking system are schematised in Figure 1.3. Collectively, these operations are hereinafter referred to as *leg-handling*.

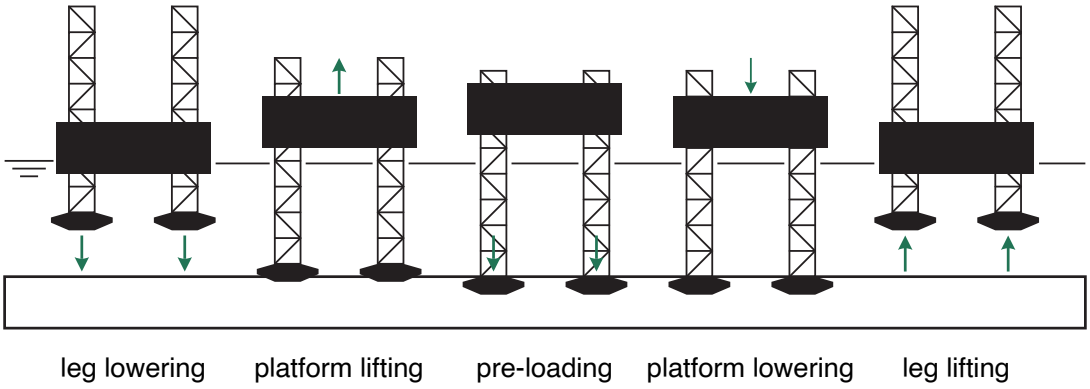

Figure 1.3: Overview of leg-handling operations involving the jacking system in chronological order.

In order to perform these operations, a linear actuator is required. A linear actuator is a mechanism that produces linear motion, i.e., is able to displace another body in a straight, linear line. Its counterpart is the rotary actuator, which produces rotary motion, such as a conventional electric motor. In jack-ups and WTIVs two types of linear actuators are generally considered: hydraulic (pin-and-yoke) and mechanical (rack-and-pinion) (Boswell, 2018). More types of linear actuators exist, such as linear induction or linear synchronous machines that work on the principle of electromagnetism. Such systems have not been implemented in jack-ups or WTIVs, but have seen implementations in systems such as magnetically levitated trains or the hyperloop.

The former is known as *pin-and-yoke* and uses hydraulic cylinders to create linear motion. Figure 1.4 shows the design and working principle of pin-and-yoke jacking systems. Operation of pin-and-yoke jacking systems is performed in stages. The hydraulic cylinders compress alternatingly with the pin inserted into the leg. Essentially, it is like climbing a ladder with alternating use of hands.

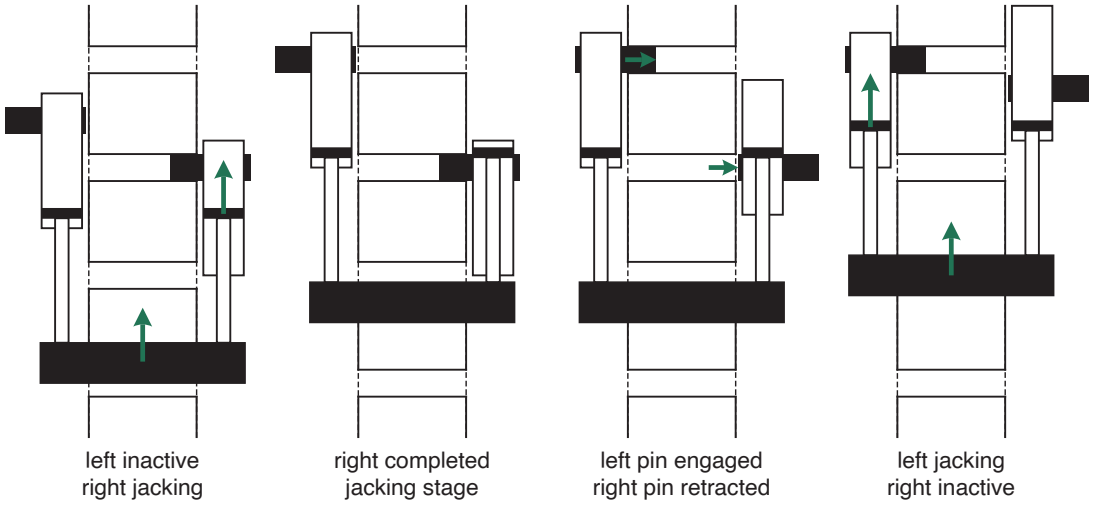

Figure 1.4: Design and function of pin-and-yoke jacking systems.

The second type of jacking system uses mechanical actuation instead of hydraulic. Such systems are known as *rack-and-pinion* and uses the mechanical contact between a rack and a pinion to convert rotary motion into linear motion. Essentially, whereas the pinion is driven by a rotary actuator, the whole assembly acts as a linear actuator. Out of these two types, only rack-and-pinion jacking systems are applicable to truss legs. Therefore, this thesis will focus on rack-and-pinion jacking systems.

1.1.4 ‖ The design of rack-and-pinion jacking systems

The rack-and-pinion jacking systems (henceforth referred to as *jacking systems*) consist of an assembly of pinions, gearboxes and electric machines and is schematised in Figure 1.5. The machine runs at relatively high rotational frequency with a low torque and the gearbox converts this to a relatively low rotational frequency with a high torque, per the law of conservation of energy. The physical contact between the rack and the pinion converts the rotational motion into translational motion, so that the legs are displaced relative to the hull. The torque produced by the machine and its rotational frequency are regulated by control systems. Additionally, whereas the jacking systems mainly transfer vertical forces, lower and upper guides provide transfer of horizontal forces.

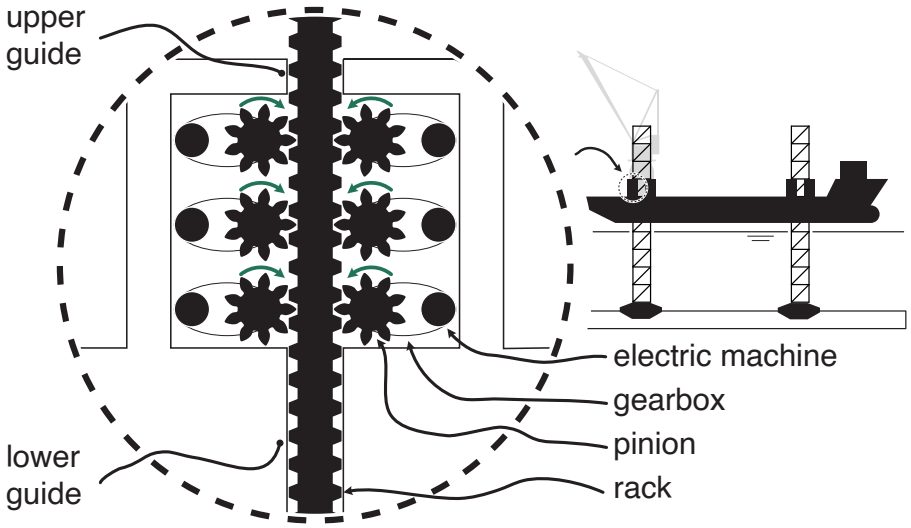

Figure 1.5: Design of a rack-and-pinion jacking system.

1.1.5 ‖ The complicated dynamics in jacking systems

Leg lowering is the first operation when the WTIV arrives at a location. The jacking systems are switched on and this causes the legs to be lowered relative to the hull. At a certain point, the spudcans will penetrate the seabed which provides an upwards reaction force. Once this reaction force is large enough, the jacking systems will lift the hull out of the water (*platform lifting*) rather than penetrate the legs further into the seabed. However, as the WTIV is in open sea, waves cause the spudcan to move up and down in the water periodically. Consequently, multiple impacts are expected with the seabed before the spudcans have finally settled. This transient phase between leg lowering and platform lifting is further referred to as the *seabed penetration phase* or *spudcan penetration phase*.

During leg lowering, the legs are under tension and the electric machines are generating, as energy is gained by lowering the legs. However, during platform lifting, the legs are under compression and the electric machines are motoring, as energy is required to lift the hull out of the water. Thus, the legs, pinions, gearboxes, machines, drives and control systems are subject to load direction changes during the seabed penetration phase.

At the same time, the jacking systems are also responsible for transferring bending moments from the legs to the hull. These bending moments in the legs arise due to wave-exciting forces or when the spudcan is penetrating the seabed under an angle. Part of this bending moment is transferred by the jacking systems by means of a vertical force couple and the other part by the upper and lower guides by means of a horizontal force couple. As a consequence of the vertical forces, the extension between the chords is unequal, which is called rack phase difference (RPD). This is schematised in Figure 1.6. Significant RPD may cause the braces between the chords to fail by buckling.

The distribution of the leg bending moment over the jacking systems and guides depends on their relative stiffness. Naturally, a higher stiffness attracts more loads. The dimensionless ratio β denotes the relative contribution of the jacking systems to transferring the leg bending moment. Normally, WTIVs are designed with this value in the range of 0.4 to 0.8 (DNV, 2022).

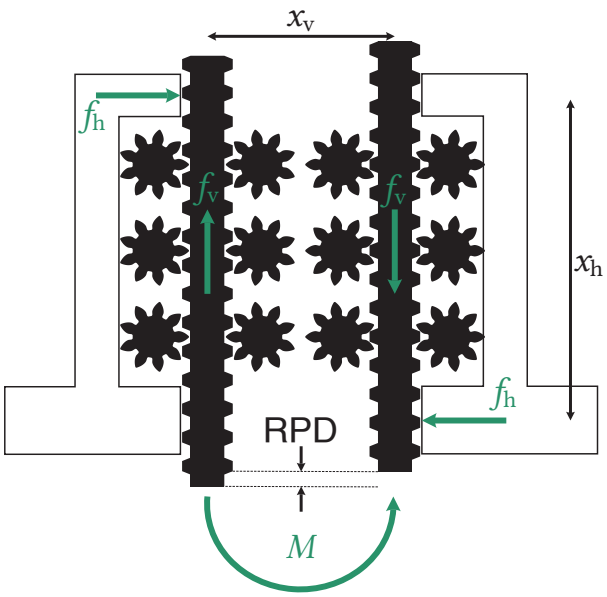

Figure 1.6: Transfer of leg bending moment M to the hull via force couples and the resulting RPD.

1.2 | Problem statement

The control system of the jacking systems ensures a certain leg-handling velocity is achieved by regulating the electric machines. Naturally, nominal operation is desired, meaning that all machines are perfectly synchronised in velocity and torque, such that RPD is absent and the jacking systems efficiently share loads. This is unfortunately

impossible due to the presence of waves and reaction forces from the seabed. Consequently, the jacking systems also transfer bending moments to the hull, load direction constantly changes and RPD is present in the legs. It is currently poorly understood what happens to the structure and jacking systems in detail during this seabed penetration phase—and how control strategies can affect the performance. The following aspects would be required in a model at minimum to accurately simulate and investigate this:

- fully modelled legs (three-dimensional truss with chords and braces);
- fully modelled jacking systems, including:
  - pinions;
  - gearboxes;
  - electric machines;
  - control systems regulating power to the machines;
- seabed model that allows seabed penetration;
- environmental loads such as gravity, wind, waves and currents.

To the best of the author's knowledge, there is no model that includes all of these aspects. The model developed by Kreuzer et al. (2014) comes closest, where the dynamics of a four-legged WTIV are modelled during seabed penetration. A realistic seabed model is considered, but the legs are simplified to equivalent cylinders and a fully modelled jacking systems is absent, as the motions of the legs are imposed, simulating the output of jacking systems. Numerous of other studies of three-legged oil-and-gas jack-ups (Bienen & Cassidy, 2006; Cassidy & Houlsby, 1999; Koole, 2015; Williams et al., 1998; Wu & Chang, 1988) and WTIVs (Heo et al., 2016; Ortega, 2016; Sonnema, 2019) exist, but these only consider global dynamic response which excludes a fully modelled jacking system and seabed penetration. Therefore, GustoMSC is interested in the development of such a model to gain insight in the interaction between the jacking system control systems and the dynamics of the structure. This leads to the problem statement:

There is no model to describe, simulate and investigate the interaction between jacking system dynamics, its control systems and WTIVs dynamics during seabed penetration, in order to gain insight in the effect of control strategies.

1.3 | Research objective

The objective of this thesis is to gain insight into the interaction between the dynamics of a WTIV and its control system. For this, the main research objective is:

Develop a model to investigate the interaction between the jacking system control systems and the dynamics of WTIVs during seabed penetration and investigate the efficacy of control strategies

In order to reach this research objective in a structured manner, the following sub-objectives are defined:

1. identify methods to model the dynamics of structures;
2. identify methods to model the dynamics of WTIVs;
   a. identify methods to model environmental loads on WTIVs;
   b. identify methods to model the load transfer between leg and hull;
   c. identify methods to model the load transfer between spudcan and seabed.
3. identify methods to regulate the dynamics of structures;
   a. identify the working principle of control systems;
   b. identify control methods for electric machines;
4. formulate equations to simulate the structural dynamics of WTIVs during seabed penetration;
   a. develop and derive a novel, detailed model of jacking system dynamics;
   b. implement conventional control methods and strategies;
5. explore the effects of different control methods or strategies on the dynamics of WTIVs

1.4 | Scope of this thesis

This section defines the scope of this thesis. Without a properly defined scope, research possibilities are endless. Therefore the following limitations are considered.

As this study does not consider the design of a WTIV, a simplified representation of WTIVs is adopted based on international guidelines and engineering estimates. The adopted design features similar characteristics such as the type of machines, the general design of the truss leg or the type of cross-sections in the leg. The simulation model has been almost fully parametrised in the sense that certain constraints are still present: e.g. the shape of the hull, the type of machines driving the jacking system or the general design of the legs cannot changed, but their characteristic values can, e.g. the mass of the hull, the power of the machines or the dimensions of the legs.

As the hull of WTIVs is significantly less flexible than the legs, it is assumed that the effects of seabed penetration are confined to their respective legs. For this reason, the adopted WTIV design is reduced to only one leg instead of four, also saving significant computational time. Furthermore, the hull is assumed rigid.

WTIVs are loaded by environmental actions such as wind, currents and waves. Whereas wave-exciting forces are zero time-averaged due to their periodicity, wind and current actions are non-zero time-averaged and will cause WTIVs to drift from their intended positions. In reality, stationkeeping of WTIVs is realised by dynamic positioning systems. These are a series of thrusters overseen by a control system. It is outside the scope of this thesis to also model such a dynamic positioning system. Therefore, wind and current actions are instead not considered and additional stationkeeping is realised by means of mooring.

The simulation model is primarily focused on the seabed penetration phase. The simulation starts during the leg lowering phase, with a predefined clearance between seabed and spudcan, and continues until a predefined duration is reached. The simulation model inherently transitions from leg lowering phase to platform lifting phase via the seabed penetration phase. With the simulation model it is possible to completely simulate the leg lowering and platform lifting load cases, as shown in Figure 1.3, though this would not produce results relevant to this research.

The jacking system control systems implemented in this thesis follow from conventional control methods and strategies for electric machines. The development of a novel control implementation is not considered.

1.5 | Structure of the thesis

The succeeding chapters of this thesis are structured in three parts: Part II contains the literature research, Part III contains the simulation model and Part IV contains the conclusion.

Literature research is performed in Part II and contains Chapters 2–4. This literature research serves as a foundation for the thesis. All sub-objectives starting with "identify" are addressed. Chapter 2 looks into a general procedure to model the dynamics of structures in order to obtain a set of governing equations and procedures. The application of this procedure to WTIVs is found in Chapter 3, by looking at international guidelines and literature. Lastly, Chapter 4 looks into control systems: what is their working principle and how is it implemented to regulate the dynamics of structures?

The simulation model developed in this thesis is called *Salacia* and is addressed in Part III. This part contains Chapters 5 and 6 and addresses the last two sub-objectives. Firstly, Chapter 5 presents the governing equations and their derivations of *Salacia* in detail, which is the simulation model developed with this thesis. Then, the results of the simulations executed with *Salacia* are presented in Chapter 6: the global dynamics and the local, control system-dependent dynamics are addressed.

Finally, Part IV gives concluding remarks on the research and the results by relating the results to the research objectives and provides a discussion and recommendations for further research.

part II

Literature research

chapter 2

A general procedure to model the dynamics of structures

This chapter presents an literature review on structural dynamical modelling of structures in general. Methods and equations identified in this chapter serve as a basis for the formulation of the model in Part III. To put it concisely, structural dynamical modelling involves taking a structure, reducing it to a simplified representative model and then evaluating the results, as schematised in Figure 2.1.

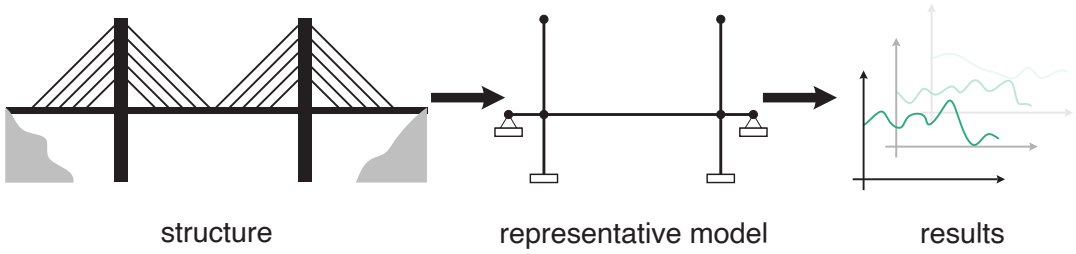

Figure 2.1: Overview of the procedure to model the dynamics of structures.

2.1 | Discretisation of structures into finite elements

Structures like buildings, bridges, wind turbines or jack-ups are complex systems of beams, columns, trusses and other structural elements. The structural dynamics of these are hard to evaluate at hand with analytical calculations. Therefore an equivalent, simplified model is created that represents all structural members, a so-called finite element (FE) model. This means that the structure is discretised: a selection of points, so-called nodes, is chosen along its geometry where displacements and internal loads can be evaluated, and external loads can be applied. Increasing the number of nodes makes the model realistic and delivers more information, at the cost of computational time: simple structures with fewer than hundred nodes can be solved and manually set up by matrix-vector equations and those with more than hundred (up to millions) require special FE software packages. This allows complex structures to be analysed in a relatively simple manner, like shown in Figure 2.1.

Nodes are linked to each other by elements so that internal loads are transferred, representing structural members. These elements can be one-, two- or three-dimensional. One-dimensional elements are sufficiently accurate for structures where the length of the element is significantly larger than its cross-section, such as trusses, but also find applications in buildings to represent beams and columns (Chopra, 2014). Nodes can have up to six degrees of freedom (DOF) in three-dimensional space: three translational directions and three rotational directions. One-dimensional elements that can only axially displace are known as bar elements (Przemieniecki, 1968). Elements formed by two nodes that can only translate are known as truss elements. The most general form are beam elements, which have two nodes with each six DOF. These three flavours of one-dimensional elements are schematised in Figure 2.2.

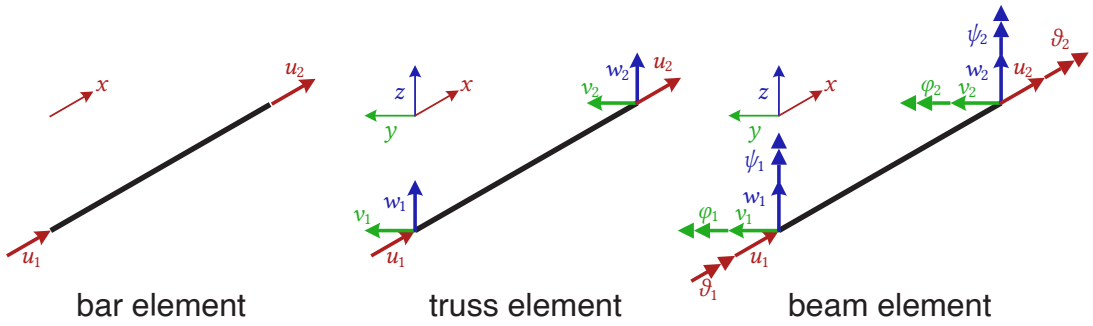

Figure 2.2: Three types of one-dimensional elements and their nodal displacements.

2.2 | The equation of motion

After discretising the structure, the equation of motion (EOM) is formulated which is the governing equation describing the dynamics of the structure. This EOM is derived from Newton's Second Law of Motion,

$$m\ddot{x} = f \tag{2.1}$$

As structures consist of more than one DOF, this equation is vectorised. In structures, the resultant force $\mathbf{M}_s\ddot{\mathbf{x}}$ on all nodes is a sum of elastic forces $\mathbf{f}_{\text{elastic}}$, damping forces $\mathbf{f}_{\text{damping}}$ and external forces $\mathbf{f}$ (Chopra, 2014), yielding

$$\mathbf{M}_s\ddot{\mathbf{x}} = \mathbf{f} - \mathbf{f}_{\text{elastic}} - \mathbf{f}_{\text{damping}} \tag{2.2}$$

The accelerations of the nodes are represented by the acceleration vector $\ddot{\mathbf{x}}$. The elastic and damping forces are proportional to the displacement $\mathbf{x}$ and velocity $\dot{\mathbf{x}}$ respectively, and this proportionality is expressed in matrices, such that the EOM becomes

$$\mathbf{M}_s\ddot{\mathbf{x}} + \mathbf{C}_s\dot{\mathbf{x}} + \mathbf{K}_s\mathbf{x} = \mathbf{f} \tag{2.3}$$

The matrices $\mathbf{M}_s$, $\mathbf{C}_s$ and $\mathbf{K}_s$ are the global structural mass, damping and stiffness matrices. The next sections describe how the EOM, Equation 2.3, and these matrices are formulated for a single beam element, yielding the element structural mass, damping and stiffness matrices $\mathbf{M}_e$, $\mathbf{C}_e$ and $\mathbf{K}_e$. It is later shown how these element matrices are combined to form global matrices to represent a complete structure. As this chapter considers a general procedure, a three-dimensional beam element is used including shear and rotary inertia effects. The complexity of the resulting general equations can then be reduced to less DOF, such as bar or truss elements shown in Figure 2.2, or by neglecting shear and rotary inertia effects.

2.3 | Structural elastic forces

As the considered element is a beam element, the element structural stiffness matrix $\mathbf{K}_e$ is derived with beam theory (Przemieniecki, 1968). Many methods are found in literature, such as Castigliano's theorem or the use of differential equations (Chopra, 2014; Przemieniecki, 1968). The method used here is that of unit displacements, as this allows the mass matrix to be derived as well in an elegant manner. This method works by imposing unit displacements

$$\boldsymbol{\xi} \equiv \begin{pmatrix} u_1 & v_1 & w_1 & \vartheta_1 & \varphi_1 & \psi_1 & u_2 & v_2 & w_2 & \vartheta_2 & \varphi_2 & \psi_2 \end{pmatrix}^{\mathrm{T}} \tag{2.4}$$

of the twelve DOF onto the beam element. This application of unit displacements causes the beam to deform. This deformation is described analytically with beam theory: $u(x)$ describes the axial deformation caused by u_1 and u_2, $\vartheta(x)$ describes the torsional deformation caused by ϑ_1 and ϑ_2, $v(x)$ describes transverse bending caused by v_1, v_2. ψ_1 and ψ_2, and $w(x)$ describes vertical bending caused by w_1, w_2. φ_1 and φ_2. As a general procedure is considered, the Timoshenko beam theory is adopted which includes shear effects (Timoshenko & Gere, 1961). The deformation of the beam element induces strains $\boldsymbol{\varepsilon}$ and stresses $\boldsymbol{\sigma}$ in the beam, which can be derived from the four beam equations. The strains and stresses are function of the unit displacements $\boldsymbol{\xi}$ by the relation (Przemieniecki, 1968)

$$\boldsymbol{\varepsilon} \equiv \mathbf{S}\boldsymbol{\xi} \tag{2.5a}$$

$$\boldsymbol{\sigma} \equiv \mathbf{E}\boldsymbol{\varepsilon} = \mathbf{E}\mathbf{S}\boldsymbol{\xi} \tag{2.5b}$$

Where $\mathbf{S}$ is a matrix relating the unit displacements $\boldsymbol{\xi}$ to the strains $\boldsymbol{\varepsilon}$ and $\mathbf{E}$ is a diagonal elasticity matrix relating stresses to the strains. It then follows that the element structural stiffness matrix $\mathbf{K}_e$ is found by integrating the strain energy over the volume of the beam, and is given by Przemieniecki (1968) as

$$\mathbf{K}_e \equiv \int_V \mathbf{S}^T \mathbf{E}\mathbf{S}\, \mathrm{d}V \tag{2.6}$$

The complete derivation is continued in Section A.1 and the result is given in Equation 2.7. By virtue of Newton's Third Law the matrix is symmetric.

$$\mathbf{K}_e = \begin{bmatrix}
\frac{EA}{l} & 0 & 0 & 0 & 0 & 0 & -\frac{EA}{l} & 0 & 0 & 0 & 0 & 0 \\
 & \frac{12EI_z}{l^3(1+\Theta_z)} & 0 & 0 & 0 & \frac{6EI_z}{l^2(1+\Theta_z)} & 0 & -\frac{12EI_z}{l^3(1+\Theta_z)} & 0 & 0 & 0 & \frac{6EI_z}{l^2(1+\Theta_z)} \\
 & & \frac{12EI_y}{l^3(1+\Theta_y)} & 0 & -\frac{6EI_y}{l^2(1+\Theta_y)} & 0 & 0 & 0 & -\frac{12EI_y}{l^3(1+\Theta_y)} & 0 & -\frac{6EI_y}{l^2(1+\Theta_y)} & 0 \\
 & & & \frac{GJ}{l} & 0 & 0 & 0 & 0 & 0 & -\frac{GJ}{l} & 0 & 0 \\
 & & & & \frac{EI_y(4+\Theta_y)}{l(1+\Theta_y)} & 0 & 0 & 0 & \frac{6EI_y}{l^2(1+\Theta_y)} & 0 & \frac{EI_y(2-\Theta_y)}{l(1+\Theta_y)} & 0 \\
 & & & & & \frac{EI_z(4+\Theta_z)}{l(1+\Theta_z)} & 0 & -\frac{6EI_z}{l^2(1+\Theta_z)} & 0 & 0 & 0 & \frac{EI_z(2-\Theta_z)}{l(1+\Theta_z)} \\
 & & & & & & \frac{EA}{l} & 0 & 0 & 0 & 0 & 0 \\
 & & & & & & & \frac{12EI_z}{l^3(1+\Theta_z)} & 0 & 0 & 0 & -\frac{6EI_z}{l^2(1+\Theta_z)} \\
 & & & & & & & & \frac{12EI_y}{l^3(1+\Theta_y)} & 0 & \frac{6EI_y}{l^2(1+\Theta_y)} & 0 \\
 & & & & & & & & & \frac{GJ}{l} & 0 & 0 \\
 & \text{sym} & & & & & & & & & \frac{EI_y(4+\Theta_y)}{l(1+\Theta_y)} & 0 \\
 & & & & & & & & & & & \frac{EI_z(4+\Theta_z)}{l(1+\Theta_z)}
\end{bmatrix} \tag{2.7}$$

2.4 | Structural inertia forces

In literature, two conventional approaches are found to model the inertia forces of a beam element: the consistent method and the lumped mass method. The consistent mass approach delivers greater accuracy than the lumped mass approach (Chopra, 2014; Przemieniecki, 1968). Nevertheless, the lumped mass approach has a computational advantage: because it is a diagonal mass matrix, the resulting computational time is significantly lower as matrix inversion is straightforward. In the simulation model, Chapter 5, both methods are used: the hull is modelled with the lumped mass method and the leg with the consistent mass method.

2.4.1 ‖ Consistent element mass matrix

The consistent element mass matrix is a matrix that is derived using the same method as the element stiffness matrix: by using the four equations that describe the deformation of the beam due to the unit displacements. Let

$$\bar{\boldsymbol{\xi}} \equiv \left(\bar{u}(x,y,z)\ \bar{v}(x,y,z)\ \bar{w}(x,y,z)\right)^T \tag{2.8}$$

be a vector that describes the three-dimensional displacement of the element at (x, y, z): the axial displacement $\bar{u}(x, y, z)$, transverse displacement $\bar{v}(x, y, z)$ and vertical displacement $\bar{w}(x, y, z)$, which are related to the six beam equations by

$$\bar{u}(x,y,z) = u(x) - y \cdot \psi(x) + z \cdot \varphi(x) \tag{2.9a}$$

$$\bar{v}(x,y,z) = v(x) - z \cdot \vartheta(x) \tag{2.9b}$$

$$\bar{w}(x,y,z) = w(x) + y \cdot \vartheta(x) \tag{2.9c}$$

As this considers a general procedure, the rotation of the cross-section is also included which adds the transverse angle of the neutral axis $\psi(x)$ and vertical angle of the neutral axis $\varphi(x)$, so-called rotary inertia effects. Similarly to

how the stresses and strains are related to the unit displacements $\boldsymbol{\xi}$ by the matrices $\mathbf{S}$ and $\mathbf{E}$, the total displacement of any point $\bar{\boldsymbol{\xi}}$ can be related to the unit displacements $\boldsymbol{\xi}$ by $\bar{\boldsymbol{\xi}} = \mathbf{D}\boldsymbol{\xi}$. It then follows that the element mass matrix is found by Przemieniecki (1968) as

$$\mathbf{M}_\mathrm{e} \equiv \rho \int_V \mathbf{D}^\mathrm{T}\mathbf{D}\,\mathrm{d}V \tag{2.10}$$

Where ρ is the density of the material. Further derivation and the element mass matrix $\mathbf{M}_\mathrm{e}$ itself are found in Section A.2 due to its size.

2.4.2 ‖ Lumped element mass matrix

In the lumped mass approach the mass of one half of the element is concentrated on the first node, and the mass of the second half is concentrated on the second node. This yields a diagonal matrix; the lumped mass matrix (Chopra, 2014)

$$\mathbf{M}_\mathrm{e} = \frac{\rho A l}{2}\left\langle 1\ 1\ 1\ 0\ 0\ 0\ 1\ 1\ 1\ 0\ 0\ 0\right\rangle_\mathrm{diag} \tag{2.11}$$

2.5 | Structural damping forces

Although damping may not be explicitly present in structures in the form of viscous dampers, it should be considered carefully. When structures vibrate energy is lost to internal friction and to the air, as the air is excited and energy is then radiated outwards (Chopra, 2014). Not implementing structural damping in dynamical models can cause numerical errors or excessive unrealistic vibrations, as convergence will not be attained. The most conventional method to model this structural damping is by means of Rayleigh damping, which is a linear combination of the structural mass and stiffness matrices and is given as (Chopra, 2014)

$$\mathbf{C}_\mathrm{s} = a_0\mathbf{M}_\mathrm{s} + a_1\mathbf{K}_\mathrm{s} \tag{2.12}$$

In order to find the unknown coefficients a_0 and a_1, the desired damping ratio ζ at two frequencies ω_i and ω_j needs to be established (Chopra, 2014). Normally, the two first natural frequencies of the structure are chosen, $\omega_{\mathrm{n}1}$ and $\omega_{\mathrm{n}2}$, as these are the most dominant motions. These natural frequencies are found by solving the eigenvalue problem

$$(\mathbf{K}_\mathrm{s} - {\omega_\mathrm{n}}^2\mathbf{M}_\mathrm{s})\mathbf{q} = 0 \tag{2.13}$$

for the unknown eigenfrequency ω_n and eigenvector $\mathbf{q}$ (Wu & Chang, 1988). This yields multiple eigenfrequencies $\boldsymbol{\omega}_\mathrm{n}$ and multiple eigenvectors $\mathbf{Q}$. Using the first two modes of the structure, the coefficients are then found by (Chopra, 2014)

$$a_0 = \zeta\frac{2\omega_{\mathrm{n}1}\omega_{\mathrm{n}2}}{\omega_{\mathrm{n}1} + \omega_{\mathrm{n}2}} \tag{2.14a}$$

$$a_1 = \zeta\frac{2}{\omega_{\mathrm{n}1} + \omega_{\mathrm{n}2}} \tag{2.14b}$$

2.6 | External forces

The last component of the EOM are the external forces $\mathbf{f}$. These external forces can be translational forces or rotational forces (moments) and are applied to the nodes. Let the external forces directly applied to the nodes be denoted as $\mathbf{f}_\mathrm{n}$. When external loads are defined as continuous loads along the beam element, it needs to be determined how these forces are distributed among the two adjacent nodes. Consider therefore the following external translational forces $\mathbf{f}_\mathrm{e}(X)$ along an element

$$\mathbf{f}_\mathrm{e}(X) = \begin{pmatrix} f_X(X) & f_X(Y) & f_Z(X)\end{pmatrix}^\mathrm{T} \tag{2.15}$$

A transformation matrix is then required to map these forces to the respective nodal forces. There are multiple approaches for this found in literature. Consider first the consistent method where this mapping is based on the beam deformation functions, just like for the consistent mass matrix (Chopra, 2014; Przemieniecki, 1968)

$$\mathbf{f} = \mathbf{f}_\mathrm{n} + \int_l \mathbf{D}^\mathrm{T}\Big|_{Y=Z=0} \mathbf{f}_\mathrm{e}(X)\,\mathrm{d}X \tag{2.16}$$

Where the matrix $\mathbf{D}$ follows from Equation 2.9, and $Y = Z = 0$ as forces are assumed to be applied to the centroid of the beam. A second, less computationally expensive, method is suggested by Chopra (2014) to use linear interpolation functions and a third method is to use the lumped method, where all external forces on one half of the element are concentrated on one node, and all external forces on the other half of the element to the other node. The consistent method is most accurate, as loads along the element induce moments on the nodes as well. The three methods are schematised in Figure 2.3 with decreasing accuracy. In the simulation model, Chapter 5, the linear interpolation method is used.

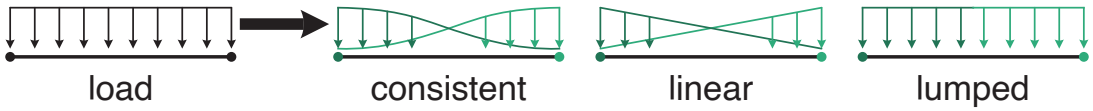

Figure 2.3: Three methods to map the external forces onto the nodes with decreasing accuracy.

2.7 | Procedures to represent a structure with multiple beam elements

Thus far, this chapter has described a general procedure to formulate the EOM for a single beam element. Even the simplest structure comprises of multiple beam elements, and therefore this section addresses how to combine multiple beam elements to form a structure.

2.7.1 || Composition of the global vectors and matrices

Given a structure with n nodes. Elements can be formed between any two nodes i and j where $i \neq j$, for a total of $m = n(n-1)/2$ elements. For each of these elements, the force vector $\mathbf{f}_{i,j}$ and mass $\mathbf{M}_{\mathrm{e}i,j}$, stiffness $\mathbf{K}_{\mathrm{e}i,j}$ and damping $\mathbf{C}_{\mathrm{e}i,j}$ matrices can be readily formulated. The procedure to form the global matrices and vector is shown in Figure 2.4 for the case of $n = 4$: the global matrices are a superposition of the element matrices at their corresponding nodes. These vectors and matrices need to be expressed in the same coordinate system. In case an element does not exist between nodes i and j, it is not included in the superposition procedure.

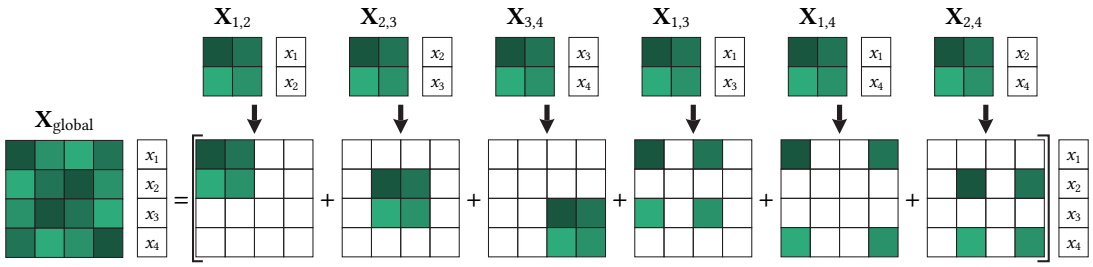

Figure 2.4: Principle of superposition to obtain the global matrices.

2.7.2 || Transformation for elements with an arbitrary orientation

In case the local coordinate system of an element deviates from the global coordinate system, a transformation needs to take place of the mass, damping and stiffness matrices and force vector, before forming the global matrices and vector. The transformation of some vector $\boldsymbol{v}$ and some matrix $\mathbf{Y}$ is formulated by Katsikadelis (2020) as

$$\boldsymbol{v}_{\text{global}} = \mathbf{R}^{\mathrm{T}}\boldsymbol{v}_{\text{local}} \tag{2.17a}$$

$$\mathbf{Y}_{\text{global}} = \mathbf{R}^{\mathrm{T}}\mathbf{Y}_{\text{local}}\mathbf{R} \tag{2.17b}$$

$$\text{where } \mathbf{R} \equiv \begin{bmatrix} \mathbf{\Lambda} & 0 & 0 & 0 \\ 0 & \mathbf{\Lambda} & 0 & 0 \\ 0 & 0 & \mathbf{\Lambda} & 0 \\ 0 & 0 & 0 & \mathbf{\Lambda} \end{bmatrix} \tag{2.17c}$$

The transformation is performed by the coordinate transformation matrix $\mathbf{\Lambda}$. This matrix transforms the global coordinate system xyz to local coordinate system XYZ. This requires the local coordinate system to be expressed in global coordinates, by means of the unit vectors $\hat{\mathbf{e}}_{\mathrm{X}}$, $\hat{\mathbf{e}}_{\mathrm{Y}}$ and $\hat{\mathbf{e}}_{\mathrm{Z}}$

$$\hat{\mathbf{e}}_{\mathrm{X}} = e_{Xx}\hat{\mathbf{i}} + e_{Xy}\hat{\mathbf{j}} + e_{Xz}\hat{\mathbf{k}} \tag{2.18a}$$

$$\hat{\mathbf{e}}_{\mathrm{Y}} = e_{Yx}\hat{\mathbf{i}} + e_{Yy}\hat{\mathbf{j}} + e_{Yz}\hat{\mathbf{k}} \tag{2.18b}$$

$$\hat{\mathbf{e}}_{\mathrm{Z}} = e_{Zx}\hat{\mathbf{i}} + e_{Zy}\hat{\mathbf{j}} + e_{Zz}\hat{\mathbf{k}} \tag{2.18c}$$

where $\hat{\mathbf{i}}$, $\hat{\mathbf{j}}$ and $\hat{\mathbf{k}}$ are unit vectors in the three directions x, y and z of the global coordinate system. It then follows that the transformation matrix $\mathbf{\Lambda}$ is given as (Katsikadelis, 2020)

$$\mathbf{\Lambda} \equiv \begin{bmatrix} e_{Xx} & e_{Xy} & e_{Xz} \\ e_{Yx} & e_{Yy} & e_{Yz} \\ e_{Zx} & e_{Zy} & e_{Zz} \end{bmatrix} \tag{2.19}$$

By definition, a beam element follows its local X-axis such that an element formed by the two nodes (x_1, y_1, z_1) and (x_2, y_2, z_2), yields $\hat{\mathbf{e}}_{\mathrm{X}}$ as

$$\hat{\mathbf{e}}_{\mathrm{X}} = \frac{x_2 - x_1}{l}\hat{\mathbf{i}} + \frac{y_2 - y_1}{l}\hat{\mathbf{j}} + \frac{z_2 - z_1}{l}\hat{\mathbf{k}} = e_{Xx}\hat{\mathbf{i}} + e_{Xy}\hat{\mathbf{j}} + +e_{Xz}\hat{\mathbf{k}} \tag{2.20}$$

where

$$l \equiv \sqrt{(x_2 - x_1)^2 + (y_2 - y_1)^2 + (z_2 - z_1)^2} \tag{2.21}$$

This definition is schematised in Figure 2.5. It is evident that the coordinates of the two nodes only provide the orientation of the X-axis, $\hat{\mathbf{e}}_{\mathrm{X}}$, whereas more information is necessary in order to establish the orientation of the Y and Z axes, $\hat{\mathbf{e}}_{\mathrm{Y}}$ and $\hat{\mathbf{e}}_{\mathrm{Z}}$—there are an infinite number of equally valid orientations of Y and Z around the X-axis without further information, as shown in Figure 2.6 for two arbitrary orientations. Unless the cross-section is axisymmetric, which results in angle-independent sectional parameters such as second moment of area, it is required to define this orientation. In Katsikadelis (2020) and in general for beam elements in FE models, this is solved by defining an additional third point on either the XY or XZ plane, which gives the orientation of the cross-section. In the simulation model, Chapter 5, axisymmetric cross-sections are exclusively used, so that any angle is sufficient.

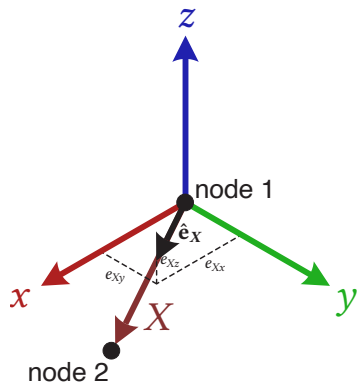

Figure 2.5: Definition of the local X-axis.

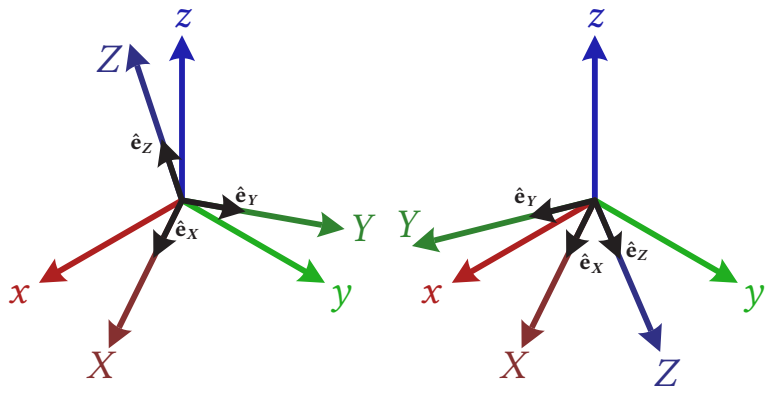

Figure 2.6: Two equally valid orientations of the local cross-section.

2.8 | Procedures to solve the equation of motion

Generally, the structures considered are rather complicated and yield a large EOM. In some cases, the equations are coupled and non-linear. In these cases, numerical integration is required in oder to evaluate the EOM, Equation 2.3, as analytical solutions are not possible. Integration is generally performed in the time-domain by means of time-stepping methods (Chopra, 2014). This means that the state of the system, $\mathbf{x}$, $\dot{\mathbf{x}}$ and $\ddot{\mathbf{x}}$, is evaluated at a certain time t_i. Then using this state the solution for time t_{i+1} is obtained. This requires the EOM is rewritten in the form of

$$\ddot{\mathbf{x}} = -\mathbf{M_s}^{-1}\mathbf{C_s}\dot{\mathbf{x}} - \mathbf{M_s}^{-1}\mathbf{K_s}\mathbf{x} + \mathbf{M_s}^{-1}\mathbf{f} \tag{2.22}$$

Then by introducing new variables $\mathbf{y} \equiv \dot{\mathbf{x}}$ and $\dot{\mathbf{y}} \equiv \ddot{\mathbf{x}}$, the EOM can be rewritten as a system of equations

$$\begin{pmatrix}\mathbf{y}\\ \dot{\mathbf{y}}\end{pmatrix} = \begin{bmatrix}0 & \mathbf{I}\\ -\mathbf{M_s}^{-1}\mathbf{K_s} & -\mathbf{M_s}^{-1}\mathbf{C_s}\end{bmatrix}\begin{pmatrix}\mathbf{x}\\ \dot{\mathbf{x}}\end{pmatrix} + \begin{pmatrix}0\\ \mathbf{M_s}^{-1}\mathbf{f}\end{pmatrix} \tag{2.23}$$

This methods requires initial conditions: at $t = 0$ the displacement $\mathbf{x}$ and velocities $\dot{\mathbf{x}}$ of all DOF need to be provided. It is often sufficient to provide trivial initial conditions and allow the system find its equilibrium. Furthermore, a suitable time step needs to be provided. If the time step is too large, the global numerical error will rapidly grow and convergence will not be achieved. On the other hand, when the time step is too small, the solution requires significant computational time and memory. The required time step is physically related to the relative stiffness of the system: if the ratio $\mathbf{K}$ to $\mathbf{M}$ is high, the system is considered stiff and requires small time steps.

Using a suitable integration scheme, Equation 2.23 can be evaluated for every moment $t > 0$. Many integration schemes exist to solve Equation 2.23, such as Euler forward, Runge-Kutta or Radau. These can be categorised as either implicit or explicit methods. Explicit methods use the state of the system at the previous time step to compute the state of the next time step, whereas the implicit method involves the next time step in the calculation (Chopra, 2014).

These integration schemes, such as Runge-Kutta, are readily available in the Python package SciPy. This implementation also has capabilities of finding the most optimal time step for convergence automatically (SciPy Developers, n.d.). Only the differential equation from Equation 2.23 needs to be provided.

| Concluding remarks

This chapter has presented a procedure to model the dynamics of any structure that can be represented by beam elements, such as buildings, bridges or WTIVs. It is presented how the governing equation—the EOM—is formulated by force balance between external and internal forces, which are the elastic, damping and inertia forces. Furthermore, it has been addressed how the EOM can be solved by means of numerical time integration.

The next chapter is an extension to this chapter, by applying the procedure to model the dynamics of structures to WTIVs specifically. This is performed by looking into relevant research and international guidelines on this subject.

chapter 3

Modelling the dynamics of wind turbine installation vessels

Extending the literature research of the previous chapter, this chapter looks into how the structural dynamics are modelled of WTIVs specifically, by looking into research and guidelines. There have been numerous studies into the global dynamics of jack-ups, especially focused on three-legged drilling rigs (Bienen & Cassidy, 2006; Cassidy & Houlsby, 1999; Koole, 2015; Sonnema, 2019; Williams et al., 1998). Moreover, international guidelines (DNV, 2022; ISO, 2015) exist which recommend methods to study the dynamics of jack-ups. All these studies and guidelines conform to FE models, as described in the previous chapter. Therefore, the structure of this chapter follows the same order as in Chapter 2. The first step is to discretise the WTIV into a representative model, described in Section 3.1. Then in Section 3.2 the transfer of elastic forces in the WTIV are presented, followed by inertia and damping forces in Section 3.3 and Section 3.4. Then external, environmental forces subjected to WTIV are addressed in Section 3.5 followed by a conclusion in Equation 3.5.3.3.

3.1 | Discretisation of wind turbine installation vessels

The overarching discretisation found in literature (Bienen & Cassidy, 2006; Cassidy & Houlsby, 1999; Williams et al., 1998) and guidelines (DNV, 2022; ISO, 2015) is to consider the legs and the hull as separate structural members, as their interface features finite stiffness, and because they have different structural properties. The next two sections look into how the legs and hulls themselves are discretised into a FE model.

3.1.1 ‖ Discretisation of the legs

For global dynamic analysis, it is recommend to represent the legs as an equivalent one-dimensional beam (DNV, 2022; ISO, 2015). The one-dimensional beam is equivalent in the sense that the axial area A, the shear area A_s and the second moment of area I are such, that application of any unit load (axial, shear or moment) results in the same deformation as the full structure. The advantage of this method is that computational time is significantly reduced for virtually the same result. The downside is that, whereas the global dynamics are accurately represented, information about motions and forces of individual chords and braces is lost. This method has been applied in models created by Bienen & Cassidy (2006); Cassidy & Houlsby (1999); Williams et al. (1998); Wu & Chang (1988), where the legs were modelled with just two elements each.

As mentioned, for global dynamical analysis the equivalent leg models are satisfactory, but when local results are required, a detailed FE model containing all structural members is suitable. A hybrid model, where an equivalent leg is combined with this detailed model at the area of interest, is a more computationally effective alternative (DNV, 2022; ISO, 2015). In this case the area of interest could be around the jacking system or near the spudcans.

Summarising, three methods with increasing accuracy and complexity are found in literature to discretise the legs. These methods are schematised in Figure 3.1 and listed in order of increasing accuracy and complexity:

1. Equivalent leg model;
2. Hybrid equivalent-detailed FE leg model;
3. Detailed FE leg model.

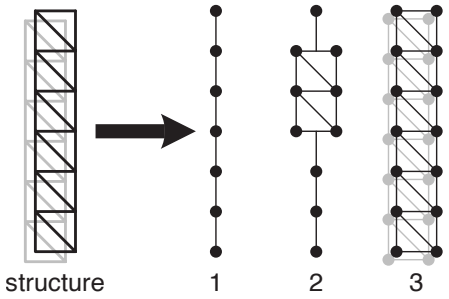

Figure 3.1: Levels of complexity of leg discretisation.

3.1.2 ‖ Discretisation of the hull

The lowest level of complexity is to assume the hull as a rigid body. The motivation behind this is that the stiffness of the hull is significantly larger than that of the legs (Koole, 2015; Williams et al., 1998; Wu & Chang, 1988). This allows the hull to be modelled by a single node.

A second level of complexity is found in international guidelines (ISO, 2015) and literature (Bienen & Cassidy, 2006; Cassidy & Houlsby, 1999; Sonnema, 2019), where the hull is represented by beam elements rather than rigid elements, meaning that stiffness is finite. In literature of three-legged jack-ups (Bienen & Cassidy, 2006) four nodes are used to represent the hull and in literature of four-legged jack-ups (Koole, 2015) five nodes are used to represent the hull.

A third and final level of complexity is recognised by international guidelines (ISO, 2015) and is a detailed FE model, just like the leg model.

Summarising, three methods with increasing accuracy and complexity to model the hull have been identified in literature. These methods are schematised in Figure 3.2 and listed below.

1. Rigid hull;
2. Equivalent hull model;
3. Detailed FE hull model.

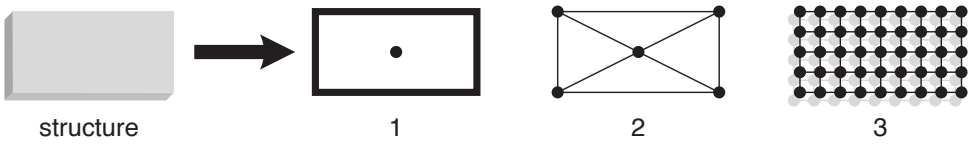

Figure 3.2: Levels of complexity of hull discretisation.

3.2 | Structural elastic forces

Structural elastic forces are present internally in the two overarching structural members, the leg and the hull. These are considered first in Section 3.2.1 and Section 3.2.2. The force transfer between these two models, the so-called leg-and-hull interface, is addressed in Section 3.2.3 followed by the force transfer between the spudcan and the seabed in Section 3.2.4.

3.2.1 ‖ Structural elastic forces of the legs

In literature the equivalent leg model is almost exclusively used and for this method numerous derivations are found for the characteristic stiffness values (EA, GA_s and I). The first two methods are recommended by ISO (2015): the first method is to use tabulated equations based on the type of bracing of the legs and the second method is to create a detailed FE model, subject these to one of the unit loads and find the characteristic stiffness

values based on the resulting deformation. Thirdly, Wu & Chang (1988) uses the principle of virtual work to obtain equivalent stiffness matrices. Lastly, Williams et al. (1998) looked into non-linear dynamic analysis for jack-ups and suggested an addition to the equivalent leg model. This addition takes into account that flexural stiffness is reduced when compressive axial loads are present, the so-called $P-\delta$ effect. As this study is concentrated on the spudcan penetration phase, where large axial loads are expected on a relatively slender structure—the triangular truss—this effect should be considered.

Non-linear consideration: P-δ effect

The EOM, Equation 2.3, is a linear system of equations. Linearity allows the principle of superposition which implies that the sum of the effects of every unit displacement applied separately, should be the same as the effect of applying all unit displacements simultaneously. Notwithstanding, there is a non-linear effect that arises when axial loads and bending are considered simultaneously. Suppose a compressive load P is applied to a simply supported beam with an initial bending deformation $\delta_0(x)$. An additional moment $M_1 = P\delta_0(x)$ is then introduced and consequently, the bending deformation increases to $\delta_1(x)$. A feedback loop arises until equilibrium is reached, which theoretically may be beyond the strength of the material. This is a non-linear effect known as $P-\delta$ effect when considered at node-element level, and $P-\Delta$ effect when looking at the effects on the complete structure. This is schematised in Figure 3.3. Effectively, this effect can be summarised that compressive loads make a structure weaker to bending, and tensile loads make it stronger.

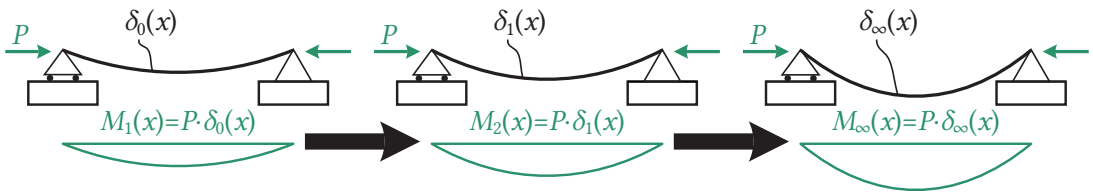

Figure 3.3: The P-δ effect: increasing deformations due to axial loads.

In mathematical context of the beam element, the axial compressive load P follows from axial displacements u_1 and u_2, such that $P \equiv (u_1 - u_2)EA/l$. The equation for a bending beam including an axial load P is given by Timoshenko & Gere (1961) as

$$\frac{\mathrm{d}^4 v}{\mathrm{d}x^4} + \frac{P}{EI_z}\frac{\mathrm{d}^2 v}{\mathrm{d}x^2} = 0 \longrightarrow \frac{\mathrm{d}^4 v}{\mathrm{d}x^4} + \frac{A}{lI_z}(u_1 - u_2)\frac{\mathrm{d}^2 v}{\mathrm{d}x^2} = 0 \tag{3.1}$$

It can be observed that the resulting solution is non-linear as axial displacements u_1 and u_2 are multiplied with the transverse bending deformation $v(x)$. This cannot be expressed in the linear form $\mathbf{K}_s\mathbf{x}$ for the EOM. It is therefore interesting to investigate whether it is even required to include $P-\delta$ effects. The effect is related to the Euler buckling load $P_{cr} = EI\pi^2(2l)^{-2}$: introducing dimensionless load ratio $q^2 \equiv P/P_{cr}$ (Williams et al., 1998) the solution to Equation 3.1 becomes

$$v(x) = c_0 + c_1 x + c_2 \cos\left(q\pi\frac{x}{l}\right) + c_3 \sin\left(q\pi\frac{x}{l}\right) \tag{3.2}$$

Where the four unknown coefficients are found by applying boundary conditions v_1, v_2, ψ_1 and ψ_2. 1 000 000 arbitrary realisations of beam unit displacements, v_1, v_2, ψ_1 and ψ_2, from a uniform distribution between -1 and 1, and 1 000 000 arbitrary realisations of dimensionless load ratio q^2 from a uniform distribution between 0 and 1 are generated. The resulting maximum beam deformation including axial effects $\hat{v}_{\text{axial}}$ and excluding axial effects $\hat{v}$ are calculated from Equation 3.2 and Equation A.11. The envelope of their resulting ratio is plotted against the dimensionless ratio q^2 in Figure 3.4.

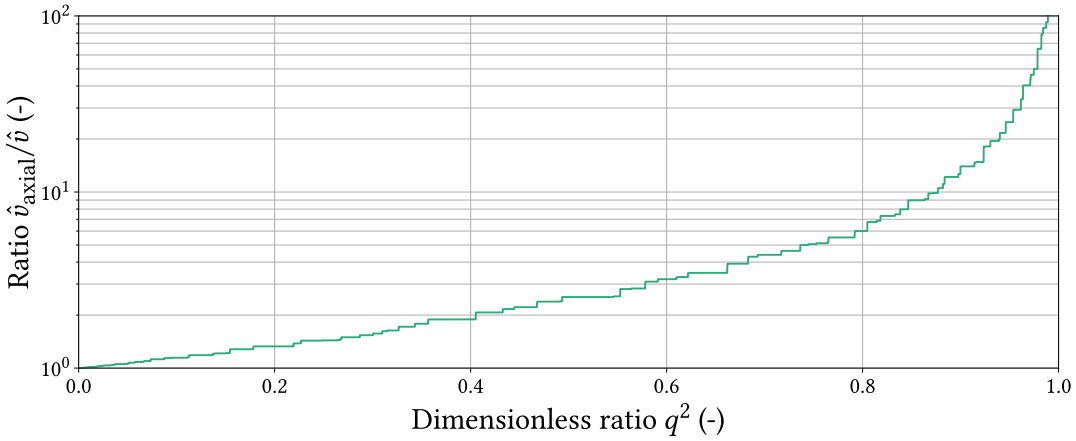

Figure 3.4: Relative importance of $P-\delta$ effects as function of load ratio q^2.

It can be observed that $P-\delta$ effects are only relevant when P approaches the Euler buckling load, regardless of the initial deformation of the beam. For relative small axial loads P, the second term in Equation 3.1 approaches zero, yielding the conventional beam equation again, Equation A.10a. Therefore, as long as the axial elastic loads are lower than roughly 40 % of the Euler buckling load, the $P-\delta$ effects can be ignored and the linear equations hold. In the simulation model, Chapter 5, a maximum dimensionless ratio q^2 of 0.18 is found, implying that $P-\delta$ effects can be neglected.

3.2.2 || Structural elastic forces of the hull

For the equivalent hull model, the characteristic stiffness values are found by applying unit loads to a detailed FE model. Due to its size, torsional stiffness is included for the hull and in-plane bending stiffness can be assumed infinite (ISO, 2015). A rigid hull is only represented by a single node, such that stiffness is not defined.

3.2.3 || Force transfer between the leg and hull

The two structural members that have been presented, the leg and the hull, require to be coupled in order to transfer loads and form one structure. This force transfer occurs through the following three connections (ISO, 2015):

1. fixation system: both vertical and horizontal forces
2. jacking system: vertical forces via contact between rack and pinion
3. guide: horizontal forces via contact between rack and guides

Additionally, contact between the rack and guides may also produce vertical forces by means of friction, but no literature considers this. Together, these three interfaces form the leg-and-hull interface. In increasing complexity of modelling and accuracy, four levels of coupling are identified from literature and guidelines: rigid coupling, linear stiffness coupling, non-linear stiffness coupling and motion coupling.

3.2.3.1 ||| Rigid coupling

The simplest method to model the leg-and-hull interface is to assume rigid coupling, as found in Cassidy & Houlsby (1999); Williams et al. (1998); Wu & Chang (1988). This is method is accurate in the case the fixation system is engaged, which is normally the case for stationary analysis in elevated conditions (DNV, 2022). This method is not applicable as the leg needs to be displaced relative to the hull.

3.2.3.2 ||| Linear stiffness coupling

The conventional and more realistic method is by modelling the connections between the legs and the hull with linear springs: vertical, horizontal and rotational springs. The characteristics of these springs depend on the

stiffness of the chords, the pinions, the guides and the structure holding the jacking system (DNV, 2022; ISO, 2015). A method to obtain these stiffness values is presented by guidelines (ISO, 2015): by creating a detailed FE model of the leg-and-hull interface and applying unit loads (axial, shear and bending moment), the equivalent spring characteristics can be obtained from the resulting displacements. Normally, the horizontal stiffness is assumed infinite (ISO, 2015).

3.2.3.3 || Non-linear stiffness coupling

The linear vertical and rotational springs are conservative as the stiffness of the leg-and-hull interface is not linear. For the connection between rack and pinion, non-linearity is introduced by backlash, due to manufacturing defects or tolerances, which means that the rack and pinion are not always meshing. Additionally, the stiffness between rack and pinion is also dependent on the angle of the pinion as the contact area is variable. For the connection between rack and guide, non-linearity is also introduced by a certain clearance between the rack and guides, as these are not always in contact.

These shortcomings are recognised by Zheng et al. (2015) and ISO (2015) and they provide solutions to model the rack-and-pinion backlash and rack-and-guide clearance, by means of gap elements. This means that they are modelled as springs that only activate in compression.

3.2.3.4 || Motion coupling

The most detailed and realistic level for the leg-and-hull interface is one that includes activation of the jacking systems, so that the legs displace relative to the hull. Serraris et al. (2017) included such a leg-and-hull interface in their model, but its level of detail is limited: the motion of the legs is imposed rather than produced by interaction between rack and pinion, making it a one-way interaction.

To the best of the author's knowledge, research including motion coupling in the leg-and-hull interface for WTIVs or jack-ups with a level of detail that includes the pinions (and gearboxes and motors), does not exist. This is because research is often focused on analyses in elevated (fixed) conditions—which excludes modelling the jacking systems—as this results in the highest loads and displacements (Bienen & Cassidy, 2006; Cassidy & Houlsby, 1999; DNV, 2022; ISO, 2015; Williams et al., 1998; Wu & Chang, 1988). In Chapter 5 this knowledge gap is addressed and such as model is developed.

3.2.4 || Force transfer between the spudcan and seabed

This section identifies methods to model the interface between the spudcan and the seabed. As stated by Kreuzer et al. (2014), there is a clear distinction between two modelling cases in literature. The first case concerns modelling of the interface where the spudcan has penetrated the ground and is fixed to the seabed with certain translational and rotational rigidity. Such models are applicable to platform lifting, pre-loading and platform lowering load cases, as schematised in Figure 1.3. The second case concerns modelling of the spudcan where it is in process of penetrating the ground, which Kreuzer et al. (2014) denoted as "grounding". Such models are applicable to the spudcan penetration phase, which is the transient phase between leg lowering and platform lifting.

3.2.4.1 || Fully penetrated spudcan

The first method considers the case where the spudcan already penetrated into the seabed, physically meaning that there is always a force transfer. Though such models are not directly applicable to this research, relevant insights might be gained from such models. Methods of increasing complexity and accuracy are presented.

The simplest model assumes the spudcans to be either pinned or fixed to the seabed. Both cases assume infinite horizontal and vertical stiffness, whereas the rotational stiffness is zero for the pinned support and infinite for the fixed support. Such models have been used in Koole (2015); Wu & Chang (1988). Essentially, these are linear springs with stiffness values of either extremes. The second level of complexity is therefore found by modelling the spudcan-and-seabed interface with linear springs of finite, non-zero stiffness. Such models are recommended by ISO (2015) are found in research of Koole (2015); Sonnema (2019).

According to Bienen & Cassidy (2006); Cassidy & Houlsby (1999), the use of pinned, fixed or linear spring supports is an oversimplification and yields conservative results. Therefore, an alternative model has been

developed by Cassidy & Houlsby (1999) called "Model C". This model is applicable to dense sand and uses a yield surface to determine whether the seabed is yielding, which results in plastic deformation, and uses the work hardening to consequently increase the stiffness of the seabed. An equivalent model for clayey seabeds called "Model B" has also been developed (Martin, 1994).

3.2.4.2 || Active spudcan penetration

The second case considers the spudcan actively penetrating the seabed. Physically, this means that the force transfer between the spudcan and the seabed is intermittent as the spudcan has not yet settled in the seabed. Kreuzer et al. (2014); Serraris et al. (2017) modelled the spudcan-and-seabed interface with a vertical non-linear penetration curve that only acts in compression, i.e. when the spudcan has a downward vertical velocity. Their reasoning for this is that the seabed will not rebound after the load is removed. Furthermore, every time the spudcan hits the seabed, the soil is under virgin conditions, so there is no physical permanent displacement of the seabed. The horizontal forces are similarly modelled with non-linear penetration curves, and are both a function of horizontal and vertical position.

These vertical and horizontal penetration curves are derived using detailed FE models of the ground and spudcan. The state-of-the-art method to model this interaction is by means of the coupled Eulerian-Lagrangian (CEL) method, which allows for large deformations. This method has been applied in Kreuzer et al. (2014) for a seabed of dense sand, which was modelled using a hypoplastic model, and in Tho et al. (2012) for a seabed of clay, which was modelled using Tresca plasticity. The CEL method has seen excellent convergence with experimental results (Tho et al., 2012).

3.3 | Structural inertia forces

According to ISO (2015) the mass terms in WTIVs are classified in three categories: structural mass, non-structural mass and added mass. Added mass follows from hydrodynamic loads and is addressed in Section 3.5. Non-structural mass includes equipment, marine growth and variable loads and is not considered in this thesis. Structural mass includes the mass of the legs, hull and spudcans. No method is recommended in these guidelines how to model the mass. Nevertheless, as described in Section 2.4 there are two conventional methods to create the mass matrix: a consistent mass matrix and a lumped mass matrix. The lumped mass approach is used in research by Koole (2015) and Wu & Chang (1988). The consistent mass approach is used in Bienen & Cassidy (2006); Cassidy & Houlsby (1999); Williams et al. (1998).

3.4 | Structural damping forces

ISO (2015) considers structural damping, hydrodynamic damping and foundation damping. All of these are recommended to be modelled with a damping ratio of 2 %. The method described in Section 2.5, Rayleigh damping, is widely used in literature as well. For structural damping Bienen & Cassidy (2006); Cassidy & Houlsby (1999); Williams et al. (1998) used a damping ratio ζ of 5 % and the natural frequencies of the first two modes, which are global surge and sway of the jack-up. Hydrodynamic damping is alternatively, and more conventionally, modelled from fluid-structure relative velocity effects which is addressed in Section 3.5.2 (ISO, 2015).

3.5 | Environmental actions

WTIVs are subjected to a variety of environmental actions. These actions include wind, wave and current actions. As stated in scope, Section 1.4, wind and current actions are not considered due to their time-averaged non-zero magnitude, which are cancelled out by dynamic positioning systems. Guidelines further recognise earthquake and operational actions (e.g. operation of the crane or moving on-board mass). These are not considered in this thesis as the former is a highly unlikely event and the latter does not (at least intentionally) occur during the operation of the jacking system.

3.5.1 ‖ Metocean data

The intensity of the environmental actions depend on metocean conditions. These are location- and season-specific characteristic values that describe the weather and sea state. Based on a few characteristic metocean values, environmental actions for a location can be calculated. ISO (2015) lists the following metocean data:

1. water depth;
2. wave characteristics: significant wave height, spectral peak period and direction;
3. current characteristics: velocity, profile and direction;
4. wind characteristics: velocity, profile and direction.

3.5.2 ‖ Wave actions on legs

Hydrodynamic actions from waves on slender structural members, like the legs, are generally calculated with the Morison equation (Bienen & Cassidy, 2006; ISO, 2015). A general procedure is presented here for a randomly oriented beam in wave conditions, including relative velocity effects. The Morison equation normally also features current effects, but as stated earlier, these are not considered in this thesis. The hydrodynamic action $\mathrm{d}\mathbf{f}_\mathrm{h}$ on an infinitesimally small segment $\mathrm{d}X$ of a beam element is given as (Chakrabarti, 1994)

$$\mathrm{d}\mathbf{f}_\mathrm{h} = \mathrm{d}\begin{pmatrix} f_{\mathrm{h},X} \\ f_{\mathrm{h},Y} \\ f_{\mathrm{h},Z} \end{pmatrix} = \left(\frac{1}{2}\rho_\mathrm{w} D_\mathrm{eq} C_\mathrm{D} \mathbf{u}_\mathrm{N} |\mathbf{u}_\mathrm{N}| + \rho_\mathrm{w} A_\mathrm{eq} C_\mathrm{M} \dot{\mathbf{u}}_\mathbf{N} \right) \mathrm{d}X \tag{3.3}$$

where ρ_w is the density of water, D_eq is the equivalent diameter of the leg, C_D is the drag coefficient, A_eq is the equivalent area of the leg, C_M is the inertia coefficient and $\mathbf{u}_\mathrm{N}$ is the absolute or relative fluid particle velocity normal to the element's axis in local coordinates. In deterministic analysis, the absolute velocity of the water particles is used, whereas in stochastic analysis the relative velocity is used. The following condition determines whether relative velocity effects should be included (ISO, 2015)

$$\pi \frac{H_\mathrm{s}}{T_\mathrm{p}} \frac{T_\mathrm{n}}{D} \geq 20 \tag{3.4}$$

where H_s is the significant wave height, T_p is the peak period, T_n is the first natural period of surge or sway motion and D is the diameter of the chord. In order to resolve the velocity normal to the element $\mathbf{u}_\mathrm{N}$ in local coordinates, it is first required to formulate the fluid particle velocity in the global coordinate system $\mathbf{u}_\mathrm{n}$, by means of a velocity field $\mathbf{u}$, which can be either absolute ($\mathbf{u}_\mathrm{abs}$) or relative ($\mathbf{u}_\mathrm{rel}$). Let the absolute fluid particle velocity $\mathbf{u}_\mathrm{abs}$ be defined by the wave-induced fluid particle velocity $\mathbf{u}_\mathrm{h}$

$$\mathbf{u}_\mathrm{abs} \equiv \mathbf{u}_\mathrm{h} \tag{3.5}$$

It then follows that the relative fluid particle velocity is found by subtracting the motion of the element

$$\mathbf{u}_\mathrm{rel} \equiv \mathbf{u}_\mathrm{h} - \dot{\mathbf{x}} \tag{3.6}$$

Secondly, it is required to know the orientation of the element. This is defined in Section 2.7.2 and is characterised by the unit vector $\hat{\mathbf{e}}_\mathbf{X}$ which runs along the axis of the element. The velocity normal to the element's axis $\mathbf{u}_\mathrm{n}$ is then found as (Chakrabarti, 1994; Wu & Chang, 1988)

$$\mathbf{u}_\mathrm{n} \equiv \hat{\mathbf{e}}_\mathbf{X} \times \mathbf{u} \times \hat{\mathbf{e}}_\mathbf{X} \tag{3.7}$$

where $\mathbf{u}$ is either $\mathbf{u}_\mathrm{abs}$ or $\mathbf{u}_\mathrm{rel}$. This velocity normal to the element's axis, $\mathbf{u}_\mathrm{n}$, is expressed in global coordinates. The velocity normal to the element's axis in the local coordinates of the element $\mathbf{u}_\mathrm{N}$ is found by using Equation 2.17a, yielding

$$\mathbf{u}_\mathrm{N} = \mathbf{\Lambda} \mathbf{u}_\mathrm{n} \tag{3.8}$$

Per definition of the Morison force, evaluating Equation 3.8 results in a zero X-component of $\mathbf{u}_\mathrm{N}$. Then, with Equation 3.3, the Y- and Z-components of the hydrodynamic action per unit length $\mathrm{d}f_{\mathrm{h},Y}$ and $\mathrm{d}f_{\mathrm{h},Z}$ can be evaluated on the legs in local coordinates. By using the integration from Equation 2.16, the resulting nodal forces are found.

Next, two models need to be established in order to evaluate the Morison equation: 1) a hydromechanic model to establish the equivalent diameter D_{eq}, equivalent area A_{eq}, drag coefficient C_{D} and inertia coefficient C_{M} and 2) a wave model to establish the absolute wave fluid particle velocity $\mathbf{u}_{\text{h}}$.

3.5.2.1 || Hydromechanic model

The hydromechanic model establishes the coefficients and characteristic dimensions required by the Morison equation: the equivalent diameter D_{eq}, equivalent area A_{eq}, drag coefficient C_{D} and inertia coefficient C_{M}. Depending on the discretisation of the legs, there are two approaches. The first approach is applicable to a detailed leg model, as the hydrodynamic action is calculated on every structural member separately. The characteristic values and coefficients then follow from the dimensions of the structural member considered. The second approach is applicable to an equivalent leg model and results in significantly decreased computational time: all structural members of one leg bay are replaced by a single vertical tubular member with the four aforementioned characteristic values such, that they result in the same load as a detailed model. In the guidelines of ISO (2015) methods are presented to calculate these values.

3.5.2.2 || Wave model

The wave model establishes the absolute wave fluid particle velocity field $\mathbf{u}_{\text{h}}$. Two methods of varying complexity are identified in literature (DNV, 2022; ISO, 2015; Williams et al., 1998): deterministic and stochastic wave models.

In a deterministic wave model, a single wave is used to calculate the resulting forces—generally the maximum wave height and its corresponding period. The wave model depends on the wave height, period and water depth. In a stochastic wave model, the sea is modelled as a superposition of many randomly generated waves with wave heights H and frequencies ω_{h} from a wave spectrum such as the JONSWAP or Pierson-Moskowitz spectrum. The phase angles α_{h} and directions of the waves ψ_{h} are also randomly distributed (ISO, 2015).

Using linear Airy wave theory, the potential function φ_{h} of a single wave realisation is given by Holthuijsen (2007) as

$$\varphi_{\text{h}} = \frac{\omega_{\text{h}} H}{2K} \frac{\cosh\left(K\left(d+z\right)\right)}{\sinh\left(Kd\right)} \cos\left(\omega_{\text{h}} t - Kx\cos\left(\psi_{\text{h}}\right) - Ky\sin\left(\psi_{\text{h}}\right) + \alpha_{\text{h}}\right) \tag{3.9}$$

where K is the wave number and d is the water depth. The wave number K follows from the dispersion relation, by solving

$$\omega_{\text{h}}{}^2 = gK\tanh(Kd) \tag{3.10}$$

for the wave number K. The wave fluid particle velocities $\mathbf{u}_{\text{h}} = \begin{pmatrix} u_{\text{hx}} & u_{\text{hy}} & u_{\text{hz}} \end{pmatrix}^{\text{T}}$ then follow by differentiating the potential function

$$u_{\text{hx}} = \frac{\partial \varphi_{\text{h}}}{\partial x} \tag{3.11a}$$

$$u_{\text{hy}} = \frac{\partial \varphi_{\text{h}}}{\partial y} \tag{3.11b}$$

$$u_{\text{hz}} = \frac{\partial \varphi_{\text{h}}}{\partial z} \tag{3.11c}$$

3.5.3 || Wave actions on hull

This section presents methods on how to model hydrodynamic actions on the hull. The method presented here is for a rigid body in water, meaning it does not deform. Furthermore, due to dynamic positioning systems on board, it is assumed the average location of the hull does not change and therefore the effect of the current and higher-order wave effects are not considered. The method to obtain the hydrodynamic actions follows the principle of superposition: an oscillating body in waves is modelled as a superposition of an oscillating body in still water and a restrained body in waves, as shown in Figure 3.5. Note that for purposes of visualisation only one DOF is shown, namely heave, whereas actually all six DOF are considered.

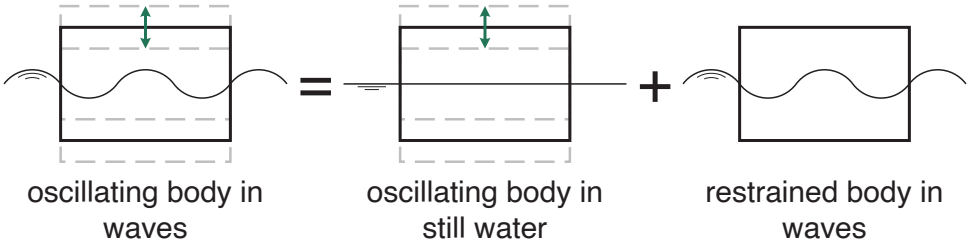

Figure 3.5: Principle of superposition applied to evaluate wave actions on hull.

3.5.3.1 || Hydromechanic reaction forces

Consider first the case of an oscillating body in still water. The motions of the body can be described by displacements, velocities and accelerations which oscillate in time and each of these motions is linearly proportional to a reactive force from the water, collectively called hydromechanic actions (Vugts, 1970). The hydromechanic actions caused by displacements of the body are called hydrostatic forces, and follow from Archimedes' Law. Its proportionality is expressed as the restoring stiffness matrix $\mathbf{K}_h$. Hydromechanic actions caused by velocities and accelerations are classified as hydrodynamic forces: damping forces are proportional to velocity and arise because the body's motion generate waves which radiate outwards, meaning energy is lost; added mass forces are proportional to acceleration and arise because the body needs to accelerate surrounding water particles. Their proportionality is expressed in matrices $\mathbf{C}_h$ and $\mathbf{M}_h$ respectively.

3.5.3.2 || Wave-exciting forces

Secondly, the case of a restrained body in waves yields the wave-exciting forces $\mathbf{f}_h$. These are a sum of Froude-Krilov and diffraction forces: the former are forces exerted by fluid pressure onto the hull and the latter is a correction in order to guarantee watertightness of the hull (Vugts, 1970).

3.5.3.3 || Procedures to obtain the hydromechanic coefficients and wave-exciting actions

The procedure to evaluate the hydromechanic coefficients $\mathbf{M}_h$, $\mathbf{C}_h$ and $\mathbf{K}_h$, and wave-exciting forces $\mathbf{f}_h$, involves complicated complex-valued equations which, even for a simple rectangular barge, require to be solved numerically. According to Vugts (1970), only ellipsoidally shaped hulls can be evaluated analytically. The numerical method to solve these equations is called boundary element method (BEM). This method discretises the hull in a finite number of panels. Special software programs have been developed for this, such as WAMIT or NEMOH. The resulting EOM for a hull with mass $\mathbf{M}_s$ is finally found to be

$$[\mathbf{M}_s + \mathbf{M}_h]\ddot{\mathbf{x}} + \mathbf{C}_h\dot{\mathbf{x}} + \mathbf{K}_h\mathbf{x} = \mathbf{f}_h \tag{3.12}$$

| Concluding remarks

This chapter has presented an expansion of the literature research on a general procedure to model the dynamics of structures from Chapter 2 by focusing on its application to WTIVs and jack-ups. Different methods, of varying complexity and accuracy, have been presented in order to establish the EOM of WTIVs and jack-ups. Based on the literature research of the preceding two chapters, this EOM of WTIVs contains both structural and hydromechanic components and is given as

$$[\mathbf{M}_s + \mathbf{M}_h]\,\ddot{\mathbf{x}} + [\mathbf{C}_s + \mathbf{C}_h]\,\dot{\mathbf{x}} + [\mathbf{K}_s + \mathbf{K}_h]\,\mathbf{x} = \mathbf{f}_h + \mathbf{f} \tag{3.13}$$

where $\mathbf{f}$ encompasses all other external loads. This literature research serves as a basis for the simulation model and is further worked out in Part III.

It can further be concluded that literature and international guidelines are mainly interested in models that assess the global dynamical response of WTIVs and jack-ups under wind and wave loading in fixed, elevated conditions. There is limited research that looks into the dynamics of WTIVs during the spudcan penetration phase of WTIVs: only the model created by Kreuzer et al. (2014) looks into this. However, this model has significant

shortcomings: the penetration of the legs are imposed (thus one-way) and lack significant details: motors, gearboxes, pinions and control systems are omitted. These details are required in order to accurately investigate the interaction between the control system and the dynamics of the WTIVs during spudcan penetration.

The next chapter, Chapter 4, is the last chapter of the literature research and addresses the need for and working principle of control systems in structures. The application of control systems to induction machines, which are the machines used in jacking systems, is also addressed.

chapter 4

Modelling and regulating the dynamics of three-phase induction machines

Control systems are used to regulate the behaviour of the jacking systems in order to perform leg-handling operations. This chapter addresses these control systems and their components; a general description as well as its implementation for jacking systems is given. The first section, Section 4.1, addresses one of the key components of the jacking systems, the electric machines, and explains why induction machines are preferred. The modelling of these induction machines are presented in Section 4.2. Thirdly, Section 4.3 addresses the need, design and function of control systems followed by their application to induction machines in Section 4.4.

4.1 | Electric machines and three-phase induction machines

For the operation of the rack-and-pinion jacking systems, a machine is required that produces rotary motion. Naturally, electric machines are more suitable compared to other machines such as internal combustion engines or pneumatic machines. This section describes such machines and explains the preference for induction machines.

4.1.1 ‖ Difference between electric machines, motors and generators

In this thesis, thus far the terms *electric machine* and *induction machine* have been used, rather than common names of *electric motor* or *induction motor*. This is because an electric machine can operate both as a motor as well as a generator. The scope of this thesis is the seabed penetration phase which is operationally characterised by the transition from leg lowering the platform lifting and for the induction machines this is characterised as the transition from generating to motoring mode. Therefore, as both operating modes are expected, the general term of an electric or induction machine is preferred.

4.1.2 ‖ The design of electric machines

The general design of electric machines is shown in Figure 4.1 and consist of a stationary part, the stator, and a rotary part, the rotor, described by angular displacement ϑ_{mr} and its time-derivatives, and subjected some external load τ_{l}. The rotor and stator contain either windings that can generate a magnetic field when currents flow through them, or they contain permanent magnets. Regardless, the interaction of these two magnetic fields generates an electromagnetic torque τ_{e} that is subjected to the rotor. In motor mode the net torque $\tau_{\mathrm{e}} - \tau_{\mathrm{l}}$ and ω_{mr} have the same sign and electrical energy is converted into mechanical energy. In generator mode the signs are opposite and mechanical energy is converted into electrical energy. Generally, two types of electric machines exist: alternating current (AC) machines and direct current (DC) machines. Only AC machines are considered.

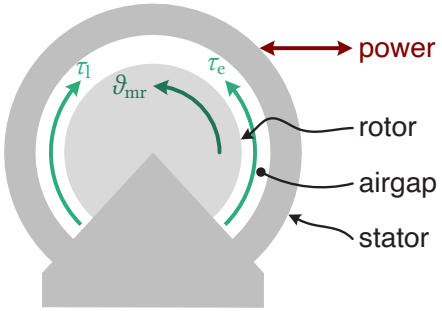

Figure 4.1: General design of an electric machine.

4.1.3 || Alternating-current electric machines

AC machines are powered by a sinusoidal current and voltage. More than one phase can be supplied to a machine, where single-phase and three-phase machines are most common. Three-phase machines have multiple advantages over its single-phase counterpart: they provide better efficiency, are simpler to design and are cheaper (Wildi, 2014). Moreover, the sum of all phases is zero at all times. Single-phase and three-phase power is schematised in Figures 4.2 and 4.3.

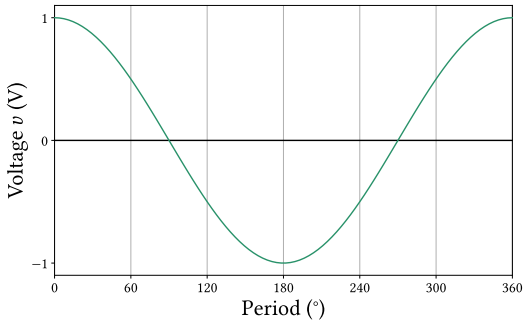

Figure 4.2: Single-phase AC electricity.

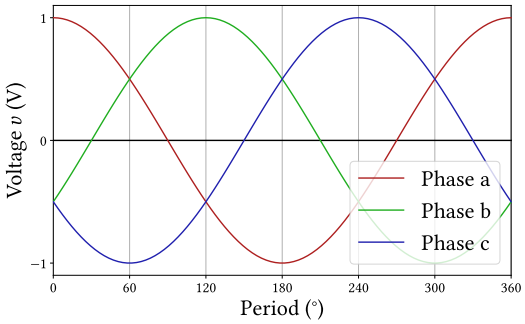

Figure 4.3: Three-phase AC electricity.

One of the key characteristics of an AC machine are its number of poles p: two magnetic north and south poles are thus four poles or two pole pairs. Consequently, this means that when the rotor completes one period (360° rotation), the generated electricity has completed two periods. Similarly, this means that two periods of supplied AC power are required for the rotor to physically rotate one period. For this reason, the electrical rotor frequency ω_{rr} is often used instead of the mechanical rotor frequency ω_{mr}, and is found by $\omega_{rr} \equiv p/2 \cdot \omega_{mr}$.

This relation between electrical frequency ω_e and electrical rotor frequency ω_{rr} is not always one-to-one. AC machines where this relation does not hold are called asynchronous or induction machines and those where this relation holds are called synchronous machines.

4.1.3.1 ||| Asynchronous or induction machines

In asynchronous or induction machines, the frequency of the rotor and the electricity do not match. This relation is quantified as the slip s, which is the difference between the synchronous frequency an the rotor frequency (Wildi, 2014)

$$s = \frac{\omega_e - \omega_{rr}}{\omega_e} \tag{4.1}$$

The reason why an induction machine cannot operate at synchronous frequency, is because it cannot develop an electromagnetic torque at that frequency: torque is only generated when the magnetic fields of the stator and rotor are asynchronous. This behaviour is characterised by the torque-velocity or torque-slip curve (Krause et al., 2013). Such a typical curve is visualised in Figure 4.4.

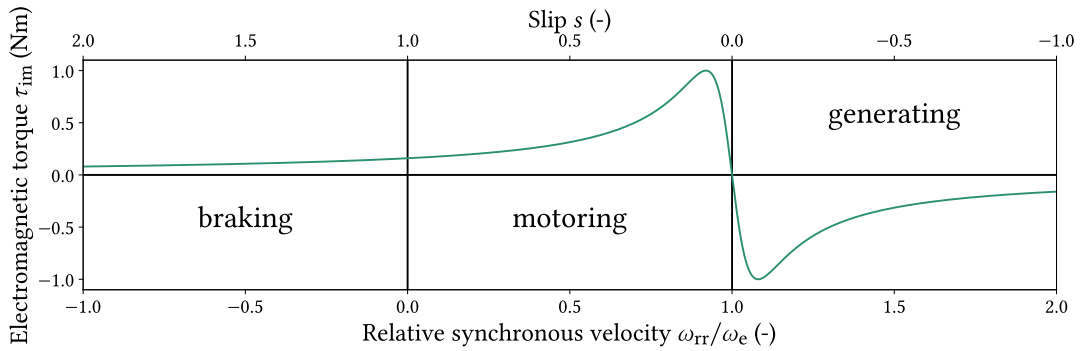

Figure 4.4: Torque-velocity or torque-slip characteristics of induction machines.

It can indeed be seen that at zero slip s or synchronous frequency ω_s no torque is developed. Such conditions only arise in case no external loads are applied. In reality, this is not possible as there is always friction from bearings. Consequently, induction machines cannot run at synchronous velocity. Besides motoring and generating mode, induction machines also have the possibility to operate as a brake (Wildi, 2014).

In induction machines, the stator contains windings connected to a power source or load. The layout of the stator windings is determined by the number of phases and poles p. The rotor naturally contains windings as well, for which the so-called *squirrel-cage* design is most commonly used (Wildi, 2014). Such a design requires no connection to an external power source or load. This makes squirrel-cage machines singly fed as only the stator is supplied. Moreover, three-phase variants of such designs are self-starting which is a significant advantage.

4.1.3.2 || Synchronous machines

In synchronous machines, the frequency of the rotor and electricity match. This means that regardless of the external load applied, the frequency remains constant. Another characteristic is that they are not self-starting, and thus require an external starter. Furthermore, whereas induction machines are single-fed, synchronous machines are doubly fed as the rotor requires a connection to a power source as well (Wildi, 2014).

4.1.3.3 || Considerations for the type of alternating-current machine

Synchronous machines are capable of operating at low frequency and can develop large torques, whereas induction machines are capable of operating at high frequency and low torques (Wildi, 2014). As the operation of jacking systems requires low frequency and a large torque, two options are possible: synchronous machines or induction machines with a gearbox. Synchronous machines with such characteristics are relatively large in dimensions and rather expensive, whereas induction machines are relatively small and cost-effective. Out of these two options, induction machines with gearboxes are significantly more cost-effective and require significantly less space.

4.1.4 || Three-phase power electronics

Three-phase induction machines seem to be the preferred choice for the actuation of jacking systems. Naturally, these machines require a source of three-phase electricity. The behaviour of induction machines is dependent on the external load and the three-phase electricity. The former cannot be controlled, naturally, whereas the latter can. AC power is characterised by its voltage and its frequency, so naturally, in order to control the behaviour of induction machines, voltage and frequency should be manipulated.

The discipline of power electronics is concerned with the conversion of electricity: DC-to-DC converters change the voltage, AC-to-AC converters change both the voltage and frequency. Note that transformers are a special type of AC-to-AC converters, that only change the voltage. Additionally, the conversion from AC-to-DC is also possible by means of rectifiers and conversion from DC-to-AC is done with inverters (Wildi, 2014).

Just like power stations onshore, the electricity generated aboard is three-phase power. The voltage and frequency of this onboard power is fixed, thus, in order to create three-phase AC power with a different frequency, a system of rectifiers and inverters is required.

4.1.4.1 || Three-phase rectifiers: conversion from ac to dc

Rectifiers convert AC power into DC power. The key to the operation of rectifiers are electrical components known as diodes, which allow only one-directional current flow: they only open for a positive voltage (Wildi, 2014). A rectifier is a cleverly designed circuit which employs these characteristics by adding a diode to each of the three phases, as shown in Figure 4.5. With three-phase power, there is always one phase larger than the other two for a duration of 120°, as can be seen from Figure 4.6. During this period, the diode of that phase opens and the other two are closed, as the voltage over these is negative. Consequently, an approximate DC voltage v_{DC} is produced that can be used by some load R. The ripples can be filtered out by the addition of an inductance in series with the load, or a capacitor parallel to the load (Wildi, 2014).

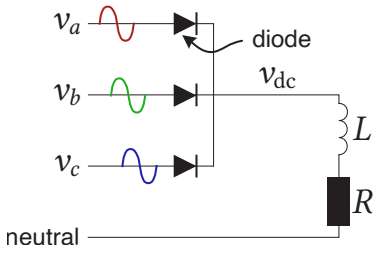

Figure 4.5: Three-phase rectifier circuit with inductive filter.

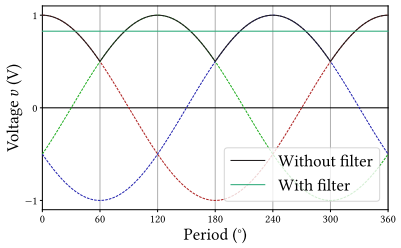

Figure 4.6: DC voltage output from three-phase rectifier.

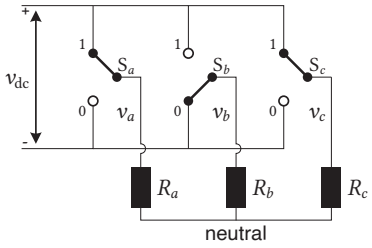

Figure 4.7: Three-phase inverter circuit with switch state 101.

4.1.4.2 Three-phase inverters: conversion from dc to ac

Inverters perform the operations of rectifiers in inverse by creating AC from DC, hence their name. The conversion of AC from a DC voltage source v_{DC} is done by so-called voltage source inverter (VSI). Additionally, conversion from a current source also exist and are known as current source inverter (CSI), but these are not considered. There are multiple methods to create three-phase voltage from a DC voltage source. The method considered here is so-called pulse-width modulation (PWM). With PWM a reference waveform is created of the desired voltage. A carrier frequency, which should be at least ten times the frequency of the reference frequency (Wildi, 2014), is compared to this reference waveform: if the reference is larger than the carrier, the state is 1, and if the reference is smaller than the carrier, the state is 0. This is schematised in Figures 4.8 and 4.9.

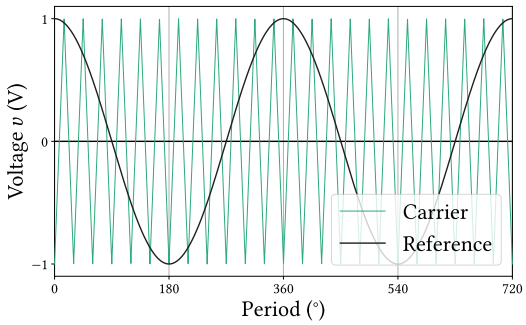

Figure 4.8: Comparison between reference and carrier signal.

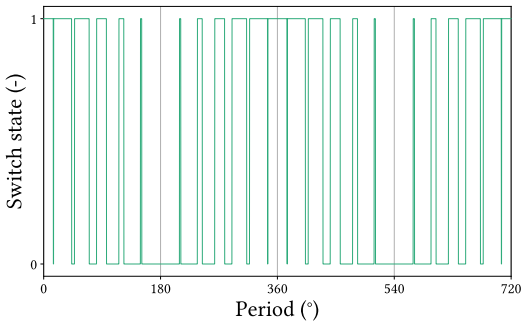

Figure 4.9: Resulting state of the switch in the inverter.

Reference waveforms are created for all three phases leading to three states. These states are given as input to the inverter circuit. This is a circuit with both diodes and switches, which are switched on by those switch commands. Such a circuit is shown in Figure 4.7 for three-phase power. A DC voltage is applied to the circuit, originating from a DC voltage source such as a battery or a rectifier. With three phases and two states per switch, the system has eight possible states. In Figure 4.7 the state 101 is shown as the first and third gate are set to 1 and the second to 0.

An example of the output of a three-phase inverter for the duration of two periods is shown in Figures 4.10–4.12, showing the switch states, phase-to-phase voltages and phase-to-neutral voltages. The resulting phase-to-neutral voltages show clear similarities with their perfect, sinusoidal references as visualised in Figure 4.3. Similar to rectifiers, filters can be used to smoothen the output. Induction machines inherently filter the voltage input, such that this is not required.

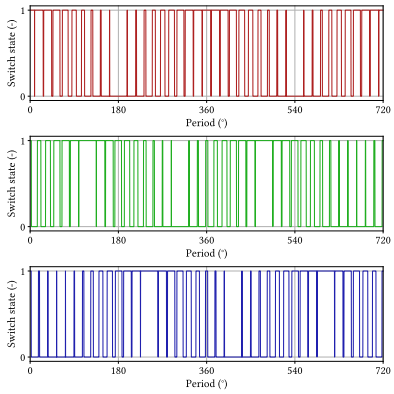

Figure 4.10: Three-phase switch states.

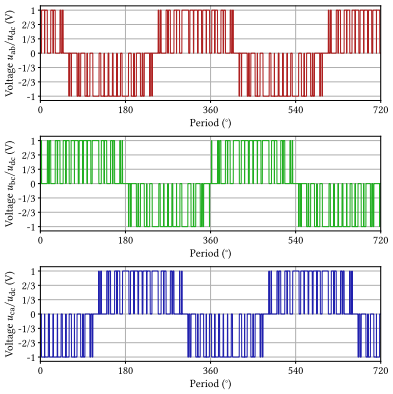

Figure 4.11: Three-phase phase-to-phase voltage.

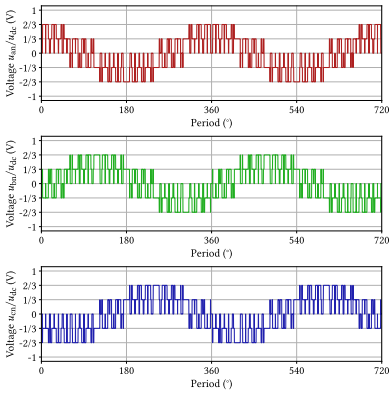

Figure 4.12: Three-phase phase-to-neutral voltage.

4.2 | Dynamics of three-phase squirrel-cage induction machines

The previous section has addressed why three-phase induction machines are the preferred type of machine in industry worldwide, due to their operation at high frequency, and has addressed methods to create any three-phase voltage that is given as input. This section looks into how the dynamics of the induction machines are modelled, i.e., what is the resulting torque and velocity of the induction machines given some externally applied load and supplied voltage.

As schematised in Figure 4.14, an induction machine has a stator and a rotor: the stator is is the stationary component and the rotor is the rotary component described by angular displacement ϑ_{mr} and angular velocity ω_{mr}. The stator is supplied with three-phase voltage $\mathbf{v}_{\mathbf{abcs}}$. Because of the property that the sum of all three phases is zero at all times, a reduction from three-phase *abc* to a two-phase equivalent $\alpha\beta$ is possible, by Clarke's transformation (Hoeijmakers, 2004)

$$\mathbf{v}_{\boldsymbol{\alpha\beta}\mathrm{s}} = \begin{pmatrix} v_{\alpha\mathrm{s}} \\ v_{\beta\mathrm{s}} \end{pmatrix} = \frac{2}{3} \begin{bmatrix} 1 & -\frac{1}{2} & -\frac{1}{2} \\ 0 & \frac{\sqrt{3}}{2} & -\frac{\sqrt{3}}{2} \end{bmatrix} \begin{pmatrix} v_{a\mathrm{s}} \\ v_{b\mathrm{s}} \\ v_{c\mathrm{s}} \end{pmatrix} \tag{4.2}$$

which is visualised Figure 4.13. This stator voltage $\mathbf{v}_{\boldsymbol{\alpha\beta}\mathrm{s}}$ causes currents in the stator $\mathbf{i}_{\boldsymbol{\alpha\beta}\mathrm{s}}$ to flow. These stator currents $\mathbf{i}_{\boldsymbol{\alpha\beta}\mathrm{s}}$ are periodical and produce a magnetic field. As changing magnetic fields induce currents, these stator currents thus induce currents in the rotor $\mathbf{i}_{\boldsymbol{\alpha\beta}\mathrm{r}}$ through magnetic induction (hence the name), which is expressed by magnetic flux linkage $\boldsymbol{\lambda}_{\boldsymbol{\alpha\beta}\mathrm{s}}$. Similarly, as the induced rotor currents $\mathbf{i}_{\boldsymbol{\alpha\beta}\mathrm{r}}$ are periodical as well, they also affect the currents in the stator though magnetic flux linkage $\boldsymbol{\lambda}_{\boldsymbol{\alpha\beta}\mathrm{r}}$. These flux linkages are described by the equations

$$\frac{\mathrm{d}}{\mathrm{d}t}\boldsymbol{\lambda}_{\boldsymbol{\alpha\beta}\mathrm{s}} = \mathbf{v}_{\boldsymbol{\alpha\beta}\mathrm{s}} - R_{\mathrm{s}}\mathbf{i}_{\boldsymbol{\alpha\beta}\mathrm{s}} \tag{4.3a}$$

$$\frac{\mathrm{d}}{\mathrm{d}t}\boldsymbol{\lambda}_{\boldsymbol{\alpha\beta}\mathrm{r}} = -R_{\mathrm{r}}\mathbf{i}_{\boldsymbol{\alpha\beta}\mathrm{r}} + \frac{p}{2}\omega_{\mathrm{mr}} \begin{bmatrix} 0 & -1 \\ 1 & 0 \end{bmatrix} \boldsymbol{\lambda}_{\boldsymbol{\alpha\beta}\mathrm{r}} \tag{4.3b}$$

where

$$\mathbf{i}_{\boldsymbol{\alpha\beta}\mathrm{s}} = \frac{1}{L_{\mathrm{r}}L_{\mathrm{s}} - {L_{\mathrm{m}}}^2} \left(L_{\mathrm{r}}\boldsymbol{\lambda}_{\boldsymbol{\alpha\beta}\mathrm{s}} - L_{\mathrm{m}}\boldsymbol{\lambda}_{\boldsymbol{\alpha\beta}\mathrm{r}} \right) \tag{4.4a}$$

$$\mathbf{i}_{\boldsymbol{\alpha\beta}\mathrm{r}} = \frac{1}{L_{\mathrm{r}}L_{\mathrm{s}} - {L_{\mathrm{m}}}^2} \left(L_{\mathrm{s}}\boldsymbol{\lambda}_{\boldsymbol{\alpha\beta}\mathrm{r}} - L_{\mathrm{m}}\boldsymbol{\lambda}_{\boldsymbol{\alpha\beta}\mathrm{s}} \right) \tag{4.4b}$$

and where R_{r} and R_{s} are the resistances of the rotor and stator respectively, L_{r} and L_{s} are the inductances of the rotor and stator respectively, L_{m} is the mutual inductance between the rotor and stator and p is the number of poles (Hoeijmakers, 2004). It can be seen in Equation 4.3 that squirrel-cage induction machines are indeed singly

fed, as only the stator is supplied by a voltage. The magnetic interaction between the stator and rotor develops a torque τ_{im} which is subjected to the rotor (Hoeijmakers, 2004)

$$\tau_{\text{im}} \equiv \frac{3}{2}\frac{p}{2} L_{\text{m}}(i_{\alpha\text{s}} i_{\beta\text{r}} - i_{\beta\text{s}} i_{\alpha\text{r}}) \tag{4.5}$$

as visualised in Figure 4.14. With a certain supplied stator voltage $\mathbf{v}_{\mathbf{abcs}}$, solving Equations 4.2–4.5 yields the electromagnetic torque τ_{im} which is used as input to the EOM of the rotor

$$j_{\text{r}} \frac{\mathrm{d}^2 \vartheta_{\text{mr}}}{\mathrm{d}t^2} = \tau_{\text{im}} - \tau_{\text{l}} \tag{4.6}$$

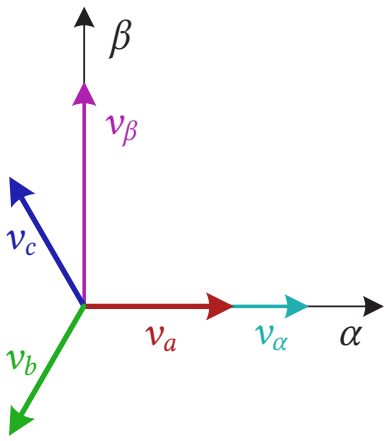

Figure 4.13: Clarke's transformation from *abc* to $\alpha\beta$.

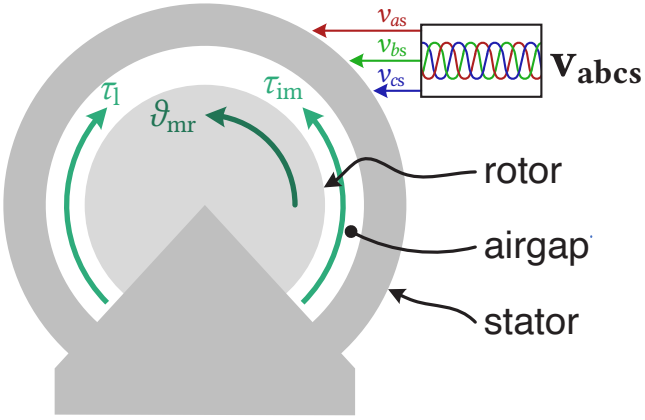

Figure 4.14: General design of an induction machine.

4.3 | The need, design and function of control systems

Control systems are implemented in a variety of systems in order to regulate their behaviour. Examples of such systems are the human body, every-day household appliances or large structures. This section addresses why they are necessary and how they are designed.

4.3.1 ‖ The need for control systems

Control systems found within organisms such as the human body have been around for eternity, whereas control systems intentionally developed by humans have been around since only antiquity. In the Roman Empire, urban water distribution to public fountains was prioritised over bathhouses and private homes, to ensure water access for all citizens. Such distribution requires a control system, which in the ancient Roman city of Pompeii was realised by a system of weirs of different heights to regulate the flow (Adam & Varène, 2008). Two millennia later, during the industrial revolution, the velocity of steam engines was kept constant by so-called ball governors: when the velocity exceeds a certain threshold, valves are opened to relieve the pressure, resulting in a decrease in velocity (Friedland, 1986).

Ostensibly, control systems are necessary to reach a certain objective automatically, which, without control systems, would require constant manual interference. In these particular cases, the objectives are prioritised water distribution and constant velocity respectively. In structures in particular, such as moveable bridges or towers, the objective is often in the nature of regulating their dynamics. Control systems in moveable bridges ensure functionality by raising and lowering the deck. In towers in earthquake-prone areas, control systems ensure structural integrity by dampening structural vibrations (Scruggs & Gavin, 2011). Regarding WTIVs, control systems ensure the leg-handling operations as outlined in Figure 1.3 can be performed under a variety of environmental circumstances.

4.3.2 ‖ The design of control systems

The general design philosophy of a control system is straightforward and is shown in Figure 4.15: an input $\mathbf{c}_{\text{in}}$ is given to a control system $\boldsymbol{\mathcal{C}}$, which produces an actuating signal $\mathbf{c}_{\text{sig}}$ which is sent to the process that is controlled $\boldsymbol{\mathcal{P}}$, yielding the process output $\mathbf{c}_{\text{out}}$ (Golnaraghi & Kuo, 2010). The actuating signals are sent to actuators within the controlled process, as these can provide physical manipulation. In the case of jacking systems with a VSI, the actuating signal $\mathbf{c}_{\text{sig}}$ are the switch states, the controlled process are the induction machines and the output are its dynamics and currents. Note that vector-matrix notation is adopted, as control systems can be multi-variable.

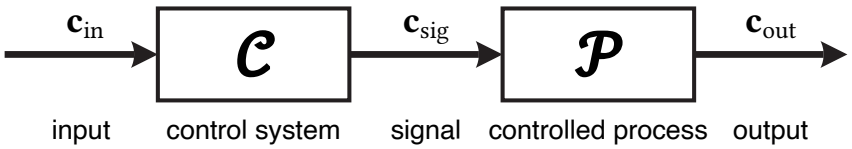

Figure 4.15: General design of control systems.

In order to develop a control system $\boldsymbol{\mathcal{C}}$, it needs to determined how the system that is to be controlled reacts to an input $\mathbf{c}_{\text{sig}}$. Kalman developed a mathematical formulation describing the influence of such as signal on the state variables $\mathbf{c}_{\text{st}}$ of a system, the so-called *state-space representation*,

$$\frac{\mathrm{d}}{\mathrm{d}t}\mathbf{c}_{\text{st}}(t) = \mathbf{A}\mathbf{c}_{\text{st}}(t) + \mathbf{B}\mathbf{c}_{\text{sig}}(t) \tag{4.7a}$$

$$\mathbf{c}_{\text{out}}(t) = \mathbf{C}\mathbf{c}_{\text{st}}(t) \tag{4.7b}$$

where $\mathbf{A}$ is the system matrix, $\mathbf{B}$ is the input matrix and $\mathbf{C}$ is the output matrix (Friedland, 1986). The set of equations allows a transfer function $\boldsymbol{\mathcal{P}}(s)$ to be formulated,

$$\boldsymbol{\mathcal{P}}(s) = \frac{\mathbf{c}_{\text{out}}(s)}{\mathbf{c}_{\text{sig}}(s)} = \mathbf{C}\left(s\mathbf{I} - \mathbf{A}\right)^{-1}\mathbf{B} \tag{4.8}$$

where s is the Laplace variable and $\mathbf{I}$ is an identity matrix (Friedland, 1986). This transfer function mathematically describes the response of a system $\mathbf{c}_{\text{out}}(s)$ to an input from a control system $\mathbf{c}_{\text{sig}}(s)$ and is used to tune the controller.

4.3.2.1 ||| Main characteristics of control systems

There are endless methods to design a control system, as each control system is designed according to their implementation. A few general design characteristics are shared between them, which are addressed in the succeeding paragraphs.

Feedback of control systems

The most notable design consideration of control systems is the implementation of feedback. Control systems without feedback are called open-loop control and those with feedback closed-loop control (Golnaraghi & Kuo, 2010). Figure 4.15 schematises an open-loop control system and Figure 4.16 schematises an closed-loop control system: in closed-loop control the loop from output to input is literally closed, hence its name. Additional sensing hardware $\boldsymbol{\mathcal{S}}$ is required in order to measure quantities $\mathbf{c}_{\text{mea}}$ of the controlled process. In the case of jacking systems the measurements can for example be currents, voltages, torque or velocity.

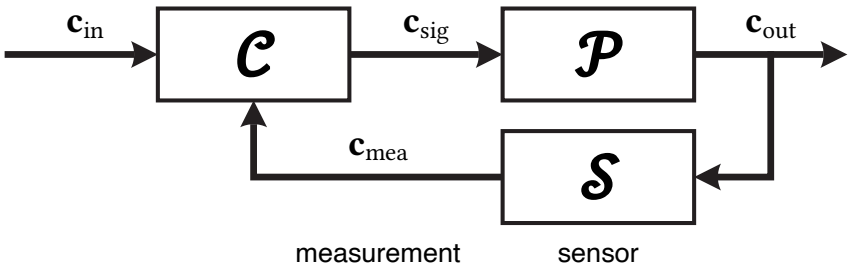

Figure 4.16: General design of closed-loop control systems.

Closed-loop control receives information about the state of the system and adjusts its output accordingly, whereas open-loop control does not take this into account. Given a jacking system subjected to an external load, with an open-loop control system it will run faster or slower depending on the load, whereas a closed-loop control system will adjust the supplied electricity accordingly and run at its intended velocity. It can be understood that, whereas closed-loop control systems are harder to design and implement, they can improve performance.

System interfacing

As previously mentioned, the control system takes an input and converts that to an output. These are not necessarily singular, as both the input as well as the output can be plural. The interfaces can be characterised as single-input single-output (SISO), single-input multiple-output (SIMO), multiple-input single output (MISO) and multiple-input multiple-output (MIMO) (Friedland, 1986).

Linear and non-linear control

A third characteristic is the linearity of the controlled process. Non-linear systems cannot be solved analytically and therefore it is challenging to created a control system for such processes. On the other hand, linear systems are easier to control as the input and output are proportional to one another. Non-linear systems may be linearised if their intended operating point allows this (Friedland, 1986). Mathematically, the state-space representation from Equation 4.7 and the transfer function from Equation 4.8 are only applicable to linear systems.

Time invariance

A last characteristic is the time invariance of the controlled process. A system is understood to be time-variant if it matters when it is controlled (Golnaraghi & Kuo, 2010). Naturally, the design of control systems for such systems is more complicated than time-invariant systems as history of the system should taken into account. In case a system is time-variant, the state-space representation from Equation 4.7 is rewritten as

$$\frac{\mathrm{d}}{\mathrm{d}t}\mathbf{c}_{\text{st}}(t) = \mathbf{A}(t)\mathbf{c}_{\text{st}}(t) + \mathbf{B}(t)\mathbf{c}_{\text{sig}}(t) \tag{4.9a}$$

$$\mathbf{c}_{\text{out}}(t) = \mathbf{C}(t)\mathbf{c}_{\text{st}}(t) \tag{4.9b}$$

where the three matrices are now time-dependent. Similarly, for time-variant systems the transfer function Equation 4.8 is not applicable. In other words, only so-called linear time-invariant (LTI) systems have transfer functions.

4.3.2.2 || Stability

Stability is an important topic when designing control systems. It is self-evident that a control system should not destabilise the controlled process $\mathcal{P}$. Systems that are inherently unstable require closed-loop control systems to become stabilised. If properly implemented, closed-loop control systems stabilise an inherently unstable system, whereas for improperly implemented control systems or none at all, it remains unstable, as visualised in Figure 4.17.

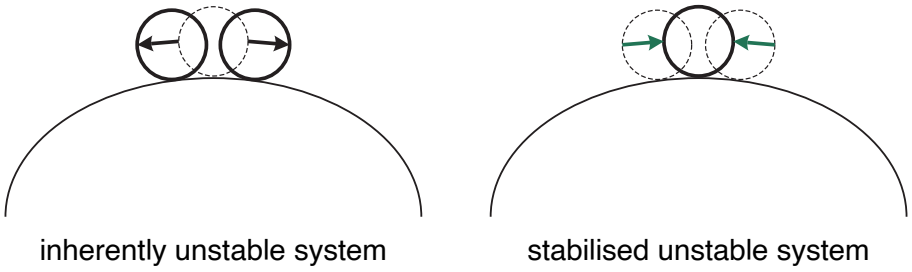

Figure 4.17: Influence of control systems on inherently unstable systems.

Contrarily, inherently stable systems do not necessarily require closed-loop control systems. Though, if implemented properly, closed-loop control systems can actually improve stability by accelerating stabilisation and with less zero-crossings (Golnaraghi & Kuo, 2010). Improper implementation, however, can destabilise an inherently stable system, as visualised in Figure 4.18.

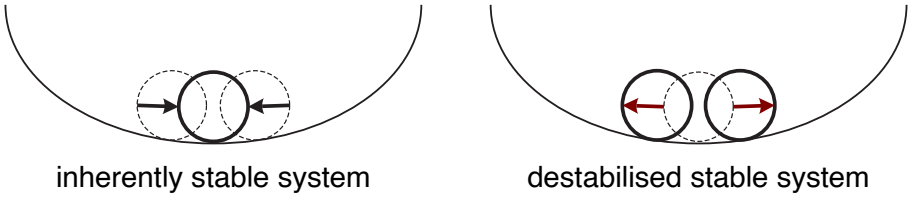

Figure 4.18: Influence of control systems on inherently stable systems.

4.3.2.3 || Controllability and observability

Another important concept of control systems are its controllability and observability. These concepts essentially determine whether a solution to a control problem exists: if a system is observable, it means that it is possible to estimate its state variables $\mathbf{c}_{\text{st}}$ based on measurements and if a system is controllable, it means that it is possible to bring the system from any initial state to another (Friedland, 1986). In the case of an induction machine, state variables are the magnetic fluxes and these are not directly measurable. However, based on a history of measurements, these state variables can be estimated using the induction machine equations. Mathematically, a system is said to be controllable if and only if

$$\operatorname{rank}\begin{bmatrix}\mathbf{B} & \mathbf{AB} & \mathbf{A}^2\mathbf{B} & \cdots & \mathbf{A}^{n-1}\mathbf{B}\end{bmatrix} = n \tag{4.10}$$

where n is the number of state variables (Friedland, 1986). Similarly, a system is said to be observable if and only if

$$\operatorname{rank}\begin{bmatrix}\mathbf{C} \\ \mathbf{AC} \\ \mathbf{A}^2\mathbf{C} \\ \vdots \\ \mathbf{A}^{n-1}\mathbf{C}\end{bmatrix} = n \tag{4.11}$$

4.3.3 || The function of control systems or control laws

Where the laws of physics govern how the controlled process $\boldsymbol{\mathcal{P}}$ transforms some actuation signal $\mathbf{c}_{\text{sig}}$ into some output $\mathbf{c}_{\text{out}}$, the control laws of the control system $\boldsymbol{C}$ dictate how this signal $\mathbf{c}_{\text{sig}}$ is calculated from some input $\mathbf{c}_{\text{in}}$. Naturally, numerous of control laws exist with each their own advantages and suitable applications. Firstly, open-loop control is addressed in Section 4.3.3.1. The most commonly used closed-loop control law is are proportional integral derivative (PID) controllers and these are addressed in Section 4.3.3.2.

4.3.3.1 || Open-loop control

The control law $\boldsymbol{C}$ for open-loop control systems is relatively straightforward. A certain input $\mathbf{c}_{\text{in}}$ is given to the controller. It is assumed that the output of the system $\mathbf{c}_{\text{out}}$ corresponds to the same quantity and is observable. Naturally, it is desired to have a control law $\boldsymbol{\mathcal{G}}_{\text{OL}}$ such, that the input and output match. The equivalent transfer function $\boldsymbol{\mathcal{G}}_{\text{OL}}$ of the open-loop system is schematised in Figure 4.19.

Figure 4.19: Equivalent open-loop control system.

The question remains, what actuating signal $\mathbf{c}_{\text{sig}}$ does the open-loop controller $\boldsymbol{C}$ need to apply to the system $\boldsymbol{\mathcal{P}}$? Based on knowledge of the system, it is known what output $\mathbf{c}_{\text{out}}$ the system gives in response to a signal $\mathbf{c}_{\text{sig}}$. Assuming this signal $\mathbf{c}_{\text{sig}}$ is correctly applied and no external disturbances are present, it inherently follows that input and output are similar: $\mathbf{c}_{\text{in}} = \mathbf{c}_{\text{out}}$, such that

$$\boldsymbol{\mathcal{G}}_{\text{OL}} = \boldsymbol{C} \cdot \boldsymbol{\mathcal{P}} = \frac{\mathbf{c}_{\text{out}}}{\mathbf{c}_{\text{in}}} = 1 \tag{4.12a}$$

$$\longrightarrow \boldsymbol{C} = \boldsymbol{\mathcal{P}}^{-1} \tag{4.12b}$$

For purposes of illustration for Equation 4.12, imagine a common open-loop system: a bread toaster. The input to this appliance c_{in} is the duration of toasting, say 60 s, which is set by a rotating dial. If every dial increment corresponds to a second, it follows that the system characteristic is given as $\mathcal{P} = 1\,\text{s}$ as every increment c_{sig} adds 1 s to the output c_{out}. It then follows that $C = 1\,\text{s}^{-1}$, $c_{\text{in}} = c_{\text{out}} = 60\,\text{s}$ and $c_{\text{sig}} = 60$. If another toaster allows the time to be set per increments of 5 s, it follows that $C = 0.2\,\text{s}^{-1}$, $\mathcal{P} = 5\,\text{s}$, $c_{\text{in}} = c_{\text{out}} = 60\,\text{s}$ and $c_{\text{sig}} = 12$.

4.3.3.2 || Closed-loop control with PID

PID control is the most conventional law for control. It is well-established and versatile and its working principle is relatively straightforward. A PID controller compares a certain setpoint $\mathbf{c}^*(t)$ to a measurement $\mathbf{c}_{\text{mea}}(t)$ and calculates the error between them as $\Delta\mathbf{c}(t) = \mathbf{c}^*(t) - \mathbf{c}_{\text{mea}}(t)$. This error, its time-integral and its time-derivative are multiplied with constants known as gains to form the actuating signal $\mathbf{c}_{\text{sig}}(t)$, by

$$\mathbf{c}_{\text{sig}}(t) = K_{\text{p}}\Delta\mathbf{c}(t) + K_{\text{i}}\int_0^t \Delta\mathbf{c}(\xi)\,\mathrm{d}\xi + K_{\text{d}}\frac{\mathrm{d}\Delta\mathbf{c}(t)}{\mathrm{d}t} \tag{4.13}$$

where ξ is an integration variable for the running integral (Golnaraghi & Kuo, 2010). These gains K_{p}, K_{i} and K_{d} are non-negative and constant. Another notation is given in the form of

$$\mathbf{c}_{\text{sig}}(t) = K_{\text{p}}\left(\Delta\mathbf{c}(t) + \frac{1}{T_{\text{i}}}\int_0^t \Delta\mathbf{c}(\xi)\,\mathrm{d}\xi + T_{\text{d}}\frac{\mathrm{d}\Delta\mathbf{c}(t)}{\mathrm{d}t}\right) \tag{4.14}$$

where T_{i} and T_{d} are the integral time and the time constant respectively. PID control systems work because they always strive to achieve the setpoint $\mathbf{c}^*(t)$: in case the error $\Delta\mathbf{c}(t)$ grows, the signal $\mathbf{c}_{\text{sig}}(t)$ is increased.

Types of PID control systems

As stated before, the gains K_{p}, K_{i} and K_{d} are non-negative, thus may be zero. In such cases, the controller can for example be PI- or PD-controller. Seven types of controllers are possible with PID. The influence of the type of PID-controller on a step response is shown in Figure 4.20 for a simple unit mass-spring-damper system with mass 1 kg, damping $1\,\text{N s m}^{-1}$, stiffness $1\,\text{N m}^{-1}$ and displacement setpoint 1 m. Furthermore, the gains themselves are either 1 or 0.

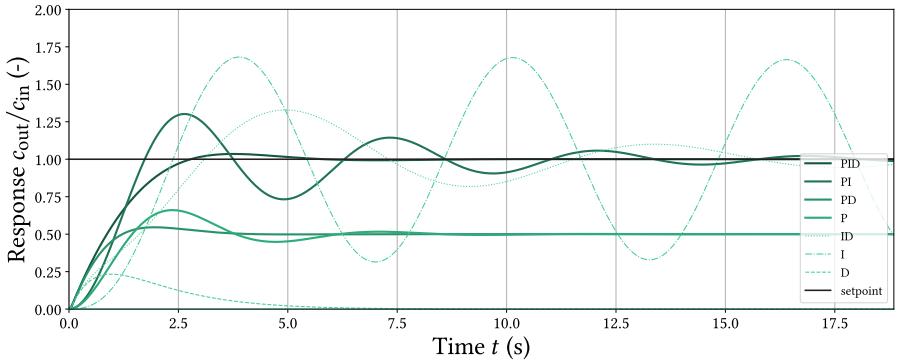

Figure 4.20: Influence of the type of PID-controller on a step response for a mass-spring-damper system.

It can be observed that convergence is not always achieved. In some cases, a P-controller is not enough and requires the integral term in order to achieve convergence. Such a PI-controller takes into account the history of the system and will therefore achieve convergence. This convergence can often take a while and therefore the addition of the derivative term is added, which decreases the so-called *settling time* (Golnaraghi & Kuo, 2010).

Tuning of PID control systems

It is important to properly tune a PID-controller, i.e. quantify the gains K_p, K_i and K_d. The response of the system strongly depends on these values and is described by a few characteristics which are schematised in Figure 4.21 (Golnaraghi & Kuo, 2010). The overshoot is the maximum output of the system in response to an input and is a measure of stability of the control system. Decreasing K_p and K_i or increasing K_d minimises overshoot. The *dead time* t_l is the time for the system to respond, the *delay time* t_d is the time it takes the system to reach 50 % of the setpoint and the *rise time* t_r is the time it takes to increase from 10 % to 90 %, which can be decreased by increasing K_p and K_i. Lastly, the settling time t_s is the time it takes for the system to reduce the error to 5 %.

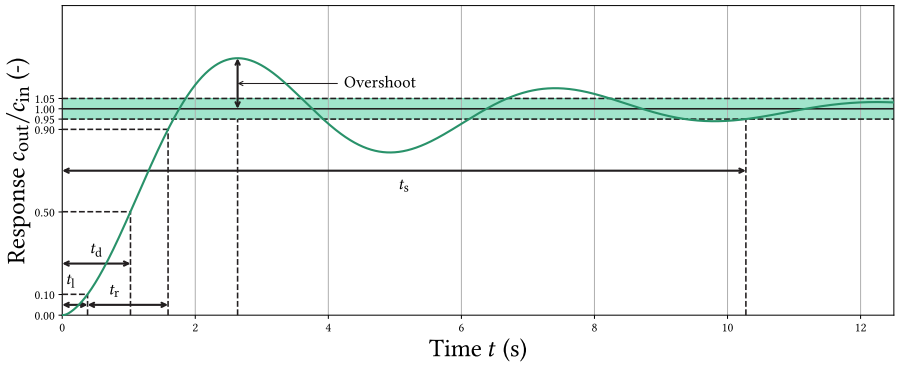

Figure 4.21: Characteristics of the response of a control system.

There are numerous methods to determine the optimum gains for a system. The methods considered here are as follows:

1. manual tuning;
2. open-loop Ziegler-Nichols;
3. closed-loop Ziegler-Nichols;
4. loop shaping.

Manual tuning

Manual tuning of a PID-controllers is mainly done through expert knowledge of the system. Knowing how certain response characteristics like settling time or overshoot can be decreased by changing the gains, an optimum can be found through manual iteration.

Open-loop tuning with Ziegler-Nichols

With open-loop Ziegler-Nichols tuning, a step input $\mathbf{c}_{\text{in}}$ is provided to a system without controller (thus open-loop). From the resulting output of the system $\mathbf{c}_{\text{out}}$, the gains are determined. These are function of the delay time t_{l} and rise time t_{r} (Ziegler & Nichols, 1942).

Closed-loop tuning with Ziegler-Nichols

With closed-loop Ziegler-Nichols tuning, the closed-loop controller is used. Gains K_{i} and K_{d} are set to 0 and K_{p} is increased until stable oscillations are found in the output $\mathbf{c}_{\text{out}}$. This is known as the ultimate gain K_{u} and the period of its resulting oscillations as T_{u}. Based on these two values and the type of PID-controller (P, PI or PID), the gains are calculated (Ziegler & Nichols, 1942).

Loop-shaping

Whereas the previous three tuning methods were heuristic, this method is mathematically founded. For a LTI system, the transfer function $\boldsymbol{\mathcal{P}}(s)$ is given by Equation 4.8. The transfer function of a PID-controller $\boldsymbol{C}(s)$ is given by the Laplace transform of Equation 4.13 as

$$\boldsymbol{C}(s) = \frac{K_{\text{d}}s^2 + K_{\text{p}}s + K_{\text{i}}}{s} \tag{4.15}$$

where the feedback is represented by the denominator. Then, the transfer function of the entire system $\boldsymbol{\mathcal{G}}_{\text{CL}}$ (thus from input $\mathbf{c}_{\text{in}}$ to output $\mathbf{c}_{\text{out}}$) is given as

$$\boldsymbol{\mathcal{G}}_{\text{CL}}(s) = \frac{\boldsymbol{C}(s)\boldsymbol{\mathcal{P}}(s)}{\mathbf{I} + \boldsymbol{C}(s)\boldsymbol{\mathcal{P}}(s)} \tag{4.16}$$

Assuming some external disturbance to the output $\mathbf{d}$ and some noise in the measurement $\mathbf{n}$, the output of the system becomes (Brunton & Kutz, 2019)

$$\mathbf{c}_{\text{out}} = \boldsymbol{\mathcal{G}}_{\text{CL}}(s)\mathbf{c}_{\text{in}} - \boldsymbol{\mathcal{T}}(s)\mathbf{n} + \boldsymbol{\mathcal{S}}(s)\mathbf{d} \tag{4.17}$$

where $\boldsymbol{\mathcal{T}}(s)$ is the complementary sensitivity function and $\boldsymbol{\mathcal{S}}(s)$ is the sensitivity function given as

$$\boldsymbol{\mathcal{S}}(s) = \frac{\mathbf{I}}{\mathbf{I} + \boldsymbol{C}(s)\boldsymbol{\mathcal{P}}(s)} \tag{4.18a}$$

$$\boldsymbol{\mathcal{T}}(s) = \frac{\boldsymbol{C}(s)\boldsymbol{\mathcal{P}}(s)}{\mathbf{I} + \boldsymbol{C}(s)\boldsymbol{\mathcal{P}}(s)} = \boldsymbol{\mathcal{G}}_{\text{CL}}(s) \tag{4.18b}$$

$$\tag{4.18c}$$

The sensitivity function $\boldsymbol{\mathcal{S}}(s)$ should be small for low frequencies, so that disturbances are rejected, and the complementary sensitivity function $\boldsymbol{\mathcal{T}}(s)$ should be small for high frequencies, so that noise is rejected (Brunton & Kutz, 2019). It is then a question of tuning the gains of the control law $\boldsymbol{C}(s)$ such, that these objectives are achieved. This can be schematised in a Bode plot.

4.4 | Control systems of induction machines

This section has been removed as it contains confidential information provided by the research partner GustoMSC

| Concluding remarks

This section has presented extensive theoretical background into modelling and controlling of three-phase squirrel-cage induction machines, as well as their application to multi-machine systems such as the jacking systems on WTIVs. It is explained why such types of induction machines are the preferred choice of actuator in jacking systems.

part III

Simulation model

chapter 5

A detailed description and derivation of the simulation model

The governing equations of the simulation model are presented in this chapter in great detail: the derivations of the equations, their coefficients and their parameters. It is deserving of a name, and thus the simulation model is named *Salacia* after the Roman Goddess of oceans, a fitting tribute. The first section, Section 5.1 presents a top level overview of Salacia: what are the components of the model and what are its simulation capabilities? Then, in Section 5.2 the sub-models are described in detail which includes their derivations. The implementation of control systems into the simulation model is described in Section 5.3. Additional background into the methodology of the model—development process, code structure, Python packages—is found in Appendix B and validation of the model is found Appendix C.

5.1 | Top level description of the simulation model

The simulation model looks into the dynamics of WTIVs during seabed penetration. This phenomenon occurs locally in the legs and therefore the model is limited to include only a single leg, limiting computational time and memory. This leg is modelled with the highest level of detail as found in the literature research: it is modelled as a three-dimensional truss with beam elements, which is the level of detail required in order to properly assess the influence of individual jacking systems on the structure. A three-dimensional overview of the model is shown in Figure 5.1 and the sub-models are shown in Figure 5.2. The global coordinate system is vertically positioned on the top of the seabed and is horizontally coincident with the centroid of the hull and truss.

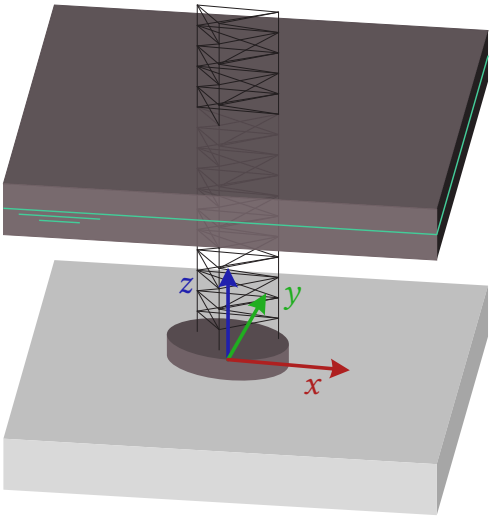

Figure 5.1: Three-dimensional overview of the model including its global coordinate system.

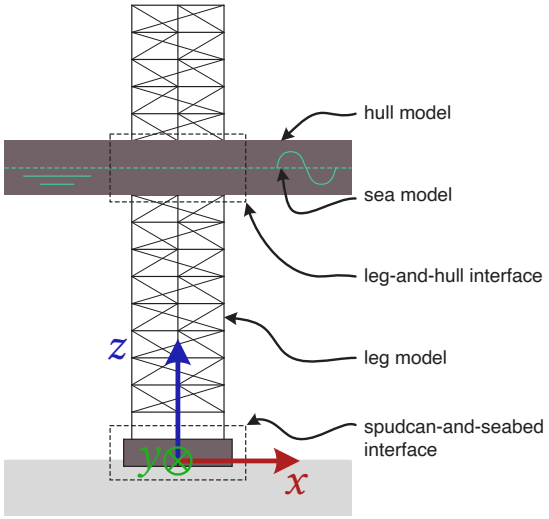

Figure 5.2: Two-dimensional overview of the model showing the sub-models.

5.2 | Detailed description and derivation of the simulation model

This section provides a detailed description and derivation of the the sub-models. Five sub-models can be understood: the sea, the hull, the leg, their leg-and-hull interface and the spudcan-and-seabed interface. All parameters used are clarified and their values used in simulations are given.

5.2.1 ‖ Sea model

The sea model is relatively straightforward: it has a water depth d, density ρ_w and waves are modelled with a single oblique incident wave by means of Airy's wave theory. The parameters defining this wave η are wave height H, wave period T, wave phase α_h and wave direction ψ_h. Figure 5.3 schematises the sea model and definition of these parameters, which have also been listed in Table 5.1. A non-zero wave direction has been adopted so that the three chords are loaded asynchronously.

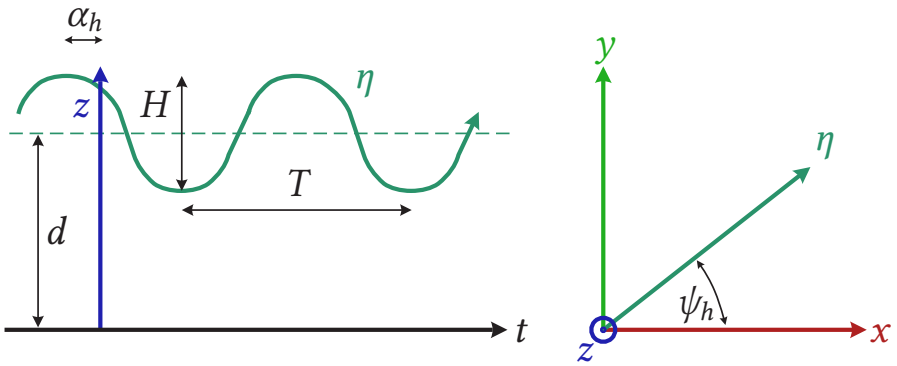

Figure 5.3: Overview of the sea model and its parameters.

Table 5.1: Parameters of the sea model.

Quantity	Symbol	Value
Water density	ρ_w	1025 kg m^{-3}
Water depth	d	40 m
Wave height	H	2.5 m
Wave period	T	8 s
Wave phase	α_h	0°
Wave direction	ψ_h	30°

5.2.2 ‖ Hull model

In the model, the hull of the WTIV is modelled as a rectangular solid barge with length l_{hull}, width b_{hull} and height h_{hull}. It has an uniformly distributed mass m_{hull}. The barge is further assumed to be rigid, meaning that it will not deform under loading. This allows the hull to be modelled by a single node at its centroid with all six DOF. This results in a diagonal structural (lumped) mass matrix $\mathbf{M}_{s,hull}$ defined as

$$\mathbf{M}_{s,hull} \equiv m_{hull} \cdot \left\langle 1 \quad 1 \quad 1 \quad \tfrac{1}{12}\left(b_{hull}^2 + h_{hull}^2\right) \quad \tfrac{1}{12}\left(h_{hull}^2 + l_{hull}^2\right) \quad \tfrac{1}{12}\left(l_{hull}^2 + b_{hull}^2\right) \right\rangle_{diag} \tag{5.1}$$

In the global coordinate system, the node of the hull is positioned at $(x_{hull}, y_{hull}, z_{hull})$, where $x_{hull} = y_{hull} = 0$ and z_{hull} follows from hydrostatic equilibrium,

$$z_{hull} = d + \frac{h_{hull}}{2} - \frac{m_{hull} + m_{leg}}{\rho_w l_{hull} b_{hull}} \tag{5.2}$$

where the third term represents the draught. The forces the hull is subjected to are gravity forces $\mathbf{f}_{w,hull}$, wave forces $\mathbf{f}_{h,hull}$, mooring forces and forces from the rack-and-guide and rack-and-pinion interfaces $\mathbf{f}_{rg,hull}$ and $\mathbf{f}_{rp,hull}$. The latter is addressed in Section 5.2.4. Table 5.2 lists the governing parameters of the hull.

Table 5.2: Parameters of the hull.

Quantity	Symbol	Value
Hull mass	m_{hull}	5.0×10^6 kg
Hull length	l_{hull}	60 m
Hull width	b_{hull}	20 m
Hull height	h_{hull}	8 m
Hull mooring period	T_{moor}	25 s

5.2.2.1 || Hydromechanic reaction forces and wave-exciting forces on the hull

The hull is subjected to hydromechanic reaction forces as well as wave-exciting forces, as described in Section 3.5.3. These are evaluated within the Python code by means of the `Capytaine` package. This Python package is an open source rewrite of the commercial BEM solver NEMOH (Ancellin, 2023). First the rectangular barge is modelled and divided into panels, and the mean sea level is defined. Then, as function of the sea and hull parameters as listed in Tables 5.1 and 5.2, the package evaluates the hydromechanics and wave-exciting forces, yielding the the added mass, damping and restoring stiffness matrix $\mathbf{M}_{\text{h,hull}}$, $\mathbf{C}_{\text{h,hull}}$ and $\mathbf{K}_{\text{h,hull}}$, and wave-exciting forces $\mathbf{f}_{\text{h,hull}}$. A screenshot of the model from Python is shown in Figure 5.4.

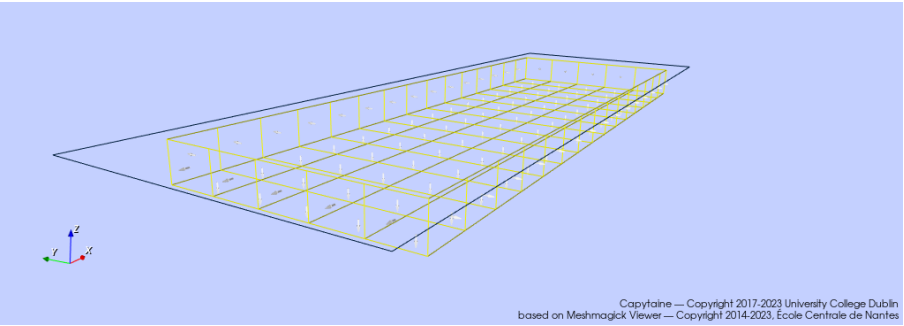

Figure 5.4: Model of the barge with the Capytaine package.

The hydromechanics and wave-exciting forces are dependent on the submerged volume of the hull. For a rectangular barge, the calculation of the submerged volume is straightforward: the product of its waterline area and its draught. Whereas the waterline area is constant, the draught is variable as the hull is lifted by the jacking systems. In the simulation model, the hydromechanics and wave-exciting are evaluated for the initial draught, rather than function of draught, to significantly decrease computational time required. More importantly, the focus of this research is on spudcan penetration phase, and not on platform lifting. With an initial draught of about 4 m as calculated from the given parameters, the model is valid up to a decreased draught of about 3 m. Beyond this value the resulting change in the hydromechanics and wave-exciting forces is significant.

5.2.2.2 || Mooring forces on the hull

Lastly, the hull is subjected to mooring forces. Even though no forces are considered that cause the ship to drift away from mean position, such as second-order wave effects, current forces or wind forces, the addition of mooring has strictly a numerical motivation. Mooring is provided in the horizontal plane, as hydrostatic restoring is absent in this plane. The mooring stiffness $\mathbf{K}_{\text{moor,hull}}$ is calculated from the mooring period T_{moor} and is given as

$$\mathbf{K}_{\text{moor,hull}} \equiv m_{\text{hull}} \left(\frac{2\pi}{T_{\text{moor}}} \right)^2 \cdot \left\langle 1 \quad 1 \quad 0 \quad 0 \quad 0 \quad \tfrac{1}{12} \left(l_{\text{hull}}^2 + b_{\text{hull}}^2 \right) \right\rangle_{\text{diag}} \tag{5.3}$$

5.2.3 || Leg model

The leg is modelled with highest level of detail: as a three-dimensional truss. This means that the physical nodes of the truss are FE nodes and the chords and braces are elements. The cross-section of the leg is an equilateral

triangle so that there are three chords. These chords are denoted by A, B and C as shown in Figure 5.5. The bracing is of type "sideways K bracing" (ISO, 2015), which are alternating diagonal braces.

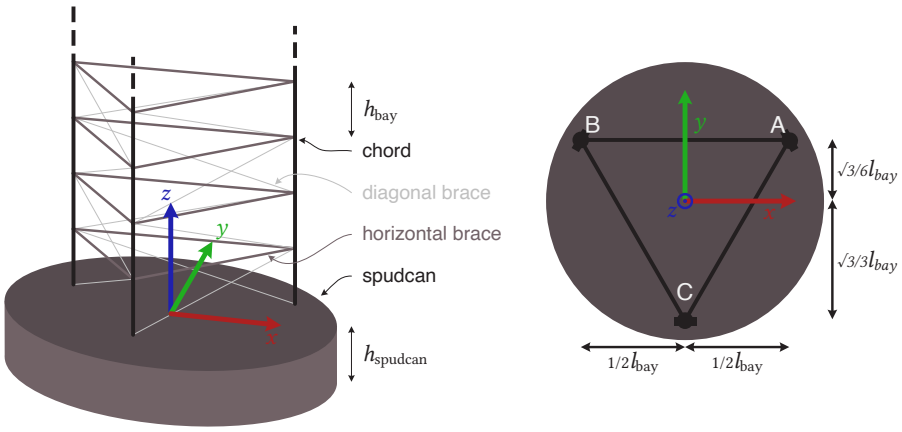

Figure 5.5: General design and parameter definition of the leg for $n_{bay} = 4$.

The general dimensions of the leg are controlled by three parameters: the number of leg bays n_{bay}, the height h_{bay} and width b_{bay} of the leg bays. On the bottom of the leg there is a spudcan that is assumed rigid and is modelled with a single node. This node is implemented with lumped mass characteristics of an equivalent cylinder with radius $r_{spudcan}$, height $h_{spudcan}$ and mass $m_{spudcan}$. The general leg design and definition of the parameters are schematised in Figure 5.5 and the parameters are given in Table 5.3.

In the global coordinate system, the node of the spudcan is positioned at $(x_{spudcan}, y_{spudcan}, z_{spudcan})$, where $x_{spudcan} = y_{spudcan} = 0$ and $z_{spudcan}$ which follows from

$$z_{spudcan} = \frac{1}{2} h_{spudcan} + \Delta z_{spudcan} \tag{5.4}$$

where $\Delta z_{spudcan}$ is the initial clearance between the seabed and the bottom of the spudcan at $t = 0$, to allow the internal dynamics to approach a state of equilibrium before the spudcan penetrates the seabed. The global coordinates of the leg nodes $(\mathbf{x}_l, \mathbf{y}_l, \mathbf{z}_l)$ follows from the rest of the geometry of the leg.

Table 5.3: Parameters of the general leg design.

Quantity	Symbol	Value
Number of leg bays	n_{bay}	15
Height of leg bays	h_{bay}	5 m
Width of leg bays	b_{bay}	9 m
Spudcan radius	$r_{spudcan}$	8 m
Spudcan height	$h_{spudcan}$	2.5 m
Spudcan mass	$m_{spudcan}$	300 000 kg
Initial spudcan clearance	$\Delta z_{spudcan}$	1.4 m

5.2.3.1 || Chord and brace design

The leg is made out of structural steel with the following three material properties: Young's modulus E_{steel}, Poisson's ratio ν_{steel} and density ρ_{steel}. The parameter values used are given in Table 5.4. Additionally, the shear modulus G_{steel} follows from

$$G_{steel} \equiv \frac{E_{steel}}{2(1 + \nu_{steel})} \tag{5.5}$$

Table 5.4: Parameters of structural steel used for the leg.

Quantity	Symbol	Value
Young's modulus	E_{steel}	210×10^9 Pa
Poisson's ratio	ν_{steel}	0.3
Density	ρ_{steel}	7900 kg m^{-3}

As schematised in Figure 5.5, the truss comprises of three types of structural members: chords, diagonal bracing and horizontal bracing. All of these members are modelled as thin-walled circular cross-sections parametrised by outer radius r_1 and inner radius r_2. The values of these parameters are listed in Table 5.5. The structural contribution of the racks that are placed on the chords is neglected.

Table 5.5: Parameters of the chord design.

Quantity	Symbol	Value
Chord outer radius	$r_{1,\text{chord}}$	300 mm
Chord inner radius	$r_{2,\text{chord}}$	225 mm
Brace outer radius	$r_{1,\text{chord}}$	150 mm
Brace inner radius	$r_{2,\text{chord}}$	115 mm

The element stiffness matrix and element mass matrix require a number of sectional parameters: cross-sectional area A, shear area A_s, second moments of area I_y and I_z, and torsion constant J. With the shear correction from Cowper (1966), these sectional parameters for hollow circular cross-sections are calculated as

$$A \equiv \pi \left(r_1^2 - r_2^2\right) \tag{5.6a}$$

$$A_s \equiv \frac{2(1+\nu_{\text{steel}})}{4+3\nu_{\text{steel}}} \cdot A \tag{5.6b}$$

$$I_y = I_z \equiv \frac{\pi}{4}\left(r_1^4 - r_2^4\right) \tag{5.6c}$$

$$J \equiv \frac{\pi}{2}\left(r_1^4 - r_2^4\right) \tag{5.6d}$$

5.2.3.2 || Internal structural forces of the leg

The global structural mass matrix $\mathbf{M}_{s,\text{leg}}$ and global structural stiffness matrix $\mathbf{K}_{s,\text{leg}}$ of the leg are created with the procedure as outlined in Section 2.7. The consistent mass method is adopted in favour of the lumped mass method. The non-linear P-δ effects as described in paragraph 3.2.1 are neglected. This is because of the following. The largest static compression loads that can occur in the leg is in elevated conditions, when it is fully carrying the mass of the hull. With the hull mass m_{hull} distributed over the three chords, the axial load per chord is about 16.4×10^6 N. The Euler buckling load for the chord is about 90.1×10^6 N, giving a dimensionless load ratio q^2 of 0.18. As this study only concentrates on the seabed penetration phase, during which hydrostatic loads carry a significant portion of the hull mass, this dimensionless load ratio q^2 is even lower during simulations. As addressed in paragraph 3.2.1, this means P-δ effects can be neglected.

The global structural damping matrix $\mathbf{C}_{s,\text{leg}}$ is formulated by means of Rayleigh damping, described in Sections 2.5 and 3.4. A structural damping ratio ζ of 2 % is used. The two frequencies used are the first two natural frequencies of the leg: ω_{n1} and ω_{n2}. These natural frequencies are found by solving the eigenvalue problem from Equation 2.13 yielding eigenfrequencies $\boldsymbol{\omega}_n$ and eigenvectors $\mathbf{Q}$. The resulting first six modes for the parameter values given in this section, are shown in Figure 5.6. The first mode is global twist around the z-axis. The second and third mode are global surge and sway and have the same natural frequency, as expected for symmetrical structures.

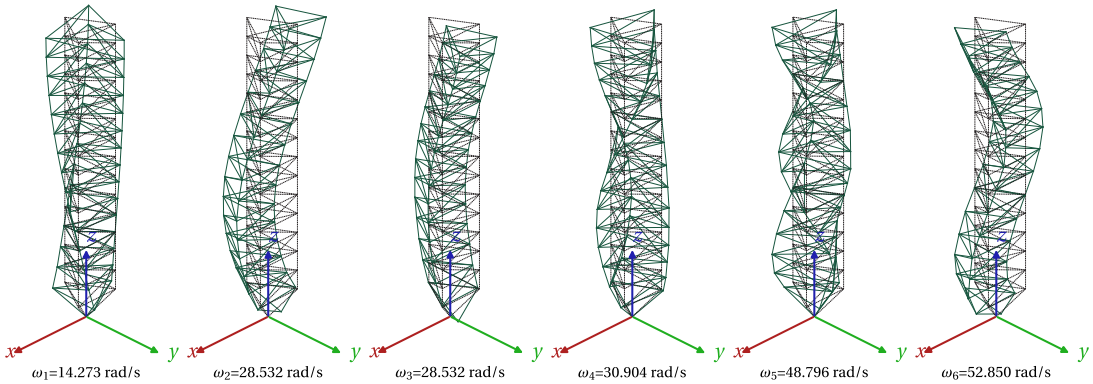

Figure 5.6: First six modes of the leg and their natural frequencies.

5.2.3.3 External forces on the leg

The external forces the leg is subjected to are gravity forces $\mathbf{f}_{\mathrm{w,leg}}$, forces from the rack-and-guide and rack-and-pinion interfaces $\mathbf{f}_{\mathrm{rg,leg}}$ and $\mathbf{f}_{\mathrm{rp,leg}}$, which are addressed in Section 5.2.4, and forces from the spudcan-and-seabed interface $\mathbf{f}_{\mathrm{ss,leg}}$, which are addressed in Section 5.2.5. Hydrodynamic forces on the leg by means of the Morison equation, Equation 3.3, are not included. Notwithstanding that the procedure to implement the Morison equation for three-dimensional structures (Equations 3.3–3.11) is rather challenging and computationally expensive, it was found that their influence on the results was negligible as the truss is relatively slender.

5.2.4 Leg-and-hull interface

This section has been removed as it contains confidential information provided by the research partner GustoMSC

5.2.5 Spudcan-and-seabed interface

This section has been removed as it contains confidential information provided by the research partner GustoMSC

5.3 Implementation of control systems into the simulation model

This section has been removed as it contains confidential information provided by the research partner GustoMSC

Concluding remarks

This section has presented an extensive description and derivation of the simulation model *Salacia*. This model is able to simulate the dynamics of a one-legged WTIV subjected to gravity and wave-exciting forces. The level of detail of this model is never seen before in literature, as the dynamics of the pinions and machine rotors, the currents in the induction machines and the electromagnetic torque can be evaluated. Furthermore, three types of conventional induction machine control systems are implemented that regulate these induction machines with varying multi-machine strategies, in order to evaluate their efficacy. The next chapter, Chapter 6, presents the results.

chapter 6

Results of the simulation model

Numerous simulations have been performed with the simulation model, with varying control laws and strategies. This section presents their results: the global dynamics of the WTIV in Section 6.1, the (local) dynamics of the jacking systems and the performance of the control strategies in Section 6.2. Furthermore, Section 6.3 conducts a study into the sensitivity of the model to changes in the parameters.

6.1 | Global dynamics of the simulation model

Global dynamics are an important measure of the behaviour and stability of a system. Irrespective of the control laws or strategies, certain dynamics are virtually always the same. These dynamics are referred to as *global dynamics* and are presented in this section. Since the leg and the hull are the only two large, global bodies in this model, this chapter is structured by looking into the global dynamics of these two first, in Section 6.1.1 and Section 6.1.2. The interaction of the leg with the seabed is addressed in Section 6.1.3. Furthermore, the global interaction between the leg and hull is characterised by the leg bending moment and is addressed in Section 6.1.4.

6.1.1 || Global dynamics of the the hull

The global dynamics of the hull are characterised by the displacement of its center of mass. The surge, heave, pitch and yaw of the hull center of mass are plotted in Figures 6.1–6.4. Hull sway and roll are not plotted as these have the same qualitative characteristics as hull surge and pitch respectively.

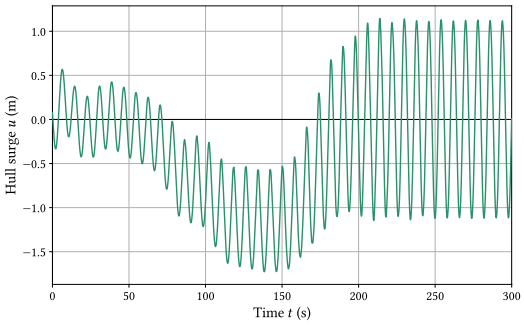

Figure 6.1: Surge of the hull.

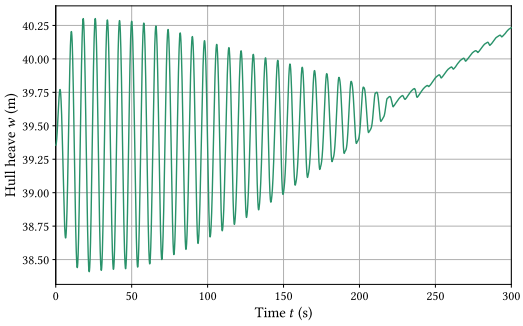

Figure 6.2: Heave of the hull.

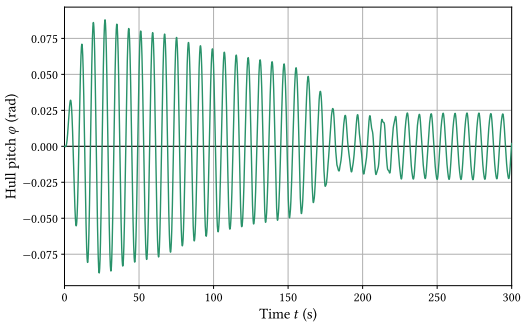

Figure 6.3: Pitch of the hull.

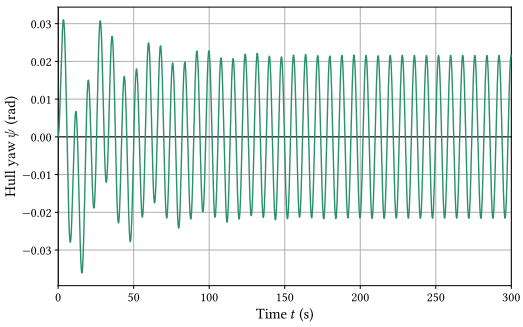

Figure 6.4: Yaw of the hull.

The influence of the sea waves on the global dynamics of the hull is indisputable: all hull motions have the same period as the waves. The following observations can be made:

Hull surge (and sway) The hull moves slightly in negative surge direction once the spudcan hits the seabed for the first time, at $t \approx 45$ s. Because of the phase angle between the spudcan surge and heave, the spudcan will always impact the seabed when its surge is off-centre (non-zero), causing the leg to act as a walking stick for the hull. This is a numerical consequence of the assumption in the spudcan-and-seabed model: the penetration curves are operated from the global origin (0,0,0) rather than a dynamically determined position. However, this does not have any implications for the results—moreover, the phenomenon is self-equilibrating. Once the spudcan has settled, at around $t \approx 220$ s, the surge and sway motions of the hull suddenly increase. This is because rather than freely floating in water, the WTIV is now pinned to the seabed such that the hull cannot freely pitch any more. The forces causing the hull to pitch cannot just vanish, thus are converted into surge.

Hull heave The hull starts from its draught position and has equilibrated with the wave-exciting forces after roughly two periods. Once the spudcan hits the seabed at $t \approx 45$ s, the amplitude of heave starts decreasing immediately. The reason for this reduction is that the instantaneous gap between the spudcan and seabed decreases, as the leg is lowered. Once the amplitude has converged to virtually 0 m, at $t \approx 220$ s, it starts steadily elevating out of the water with minimal interference of the waves. It can therefore be understood that *leg lowering* occurs in the period $t \in [0\,\text{s}, 45\,\text{s}]$ and *platform lifting* in the period $t \in [220\,\text{s}, \rightarrow)$. The period between that, $t \in [45\,\text{s}, 220\,\text{s}]$, can be understood as the transient *spudcan penetration* phase. These results of hull heave are in excellent qualitative agreement with Vazquez et al. (2017).

Hull pitch (and roll) The hull pitch motions have equilibrated with the wave-exciting forces after roughly two periods as well. Its amplitude also decreases because of leg lowering but does not decrease to zero, as its motions are sustained due to the pinned support of the spudcan.

Hull yaw The hull yaw takes longer to equilibrate. Its amplitude does not decrease because its plane is perpendicular to the leg lowering actions.

6.1.2 ‖ Global dynamics of the leg

The global dynamics of the leg are characterised by the surge, sway and heave displacements of the nodes. In Figure 6.5 the vertical position of the nodes are plotted. Similar to the reduction in heave amplitude of the hull, the legs also decrease in amplitude. Furthermore, it can be observed that their average global heave position decreases. In Figure 6.6 the resulting leg extension is plotted. The leg extension does not contain any wave-induced dynamics. This is because it is calculated from the rotor rotation, such that the control system acts as a filter.

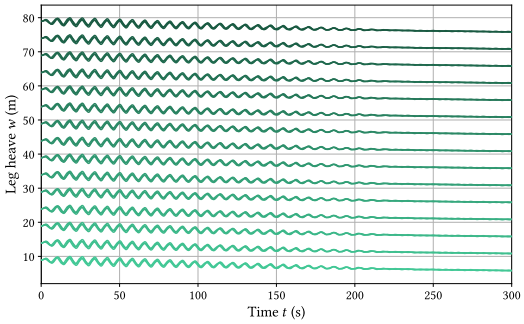

Figure 6.5: Heave of the leg nodes.

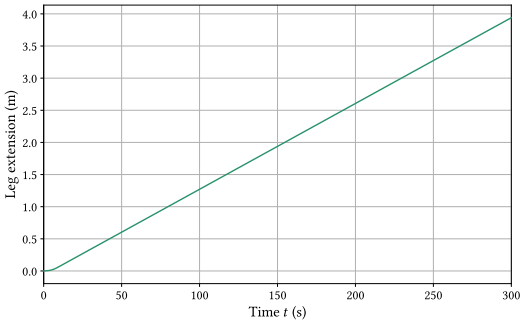

Figure 6.6: Downwards vertical leg extension.

The global three-dimensional positions are plotted in a three-dimensional graph in Figure 6.7. The colour indicates the time and goes from light green to dark green chronologically. It can be observed that initially, the dynamics of the leg take on a hourglass shape. This is because at the center of the hourglass, the leg-and-hull interface is positioned which acts as an equivalent rotational spring. After the spudcan has pinned to the seabed, the dark green lines, it can clearly be observed that the legs oscillate around the pinned support rather than the leg-and-hull interface: the leg-and-hull interface itself is displaced. This decreases the roll and pitch of the hull and increases the hull surge and sway.

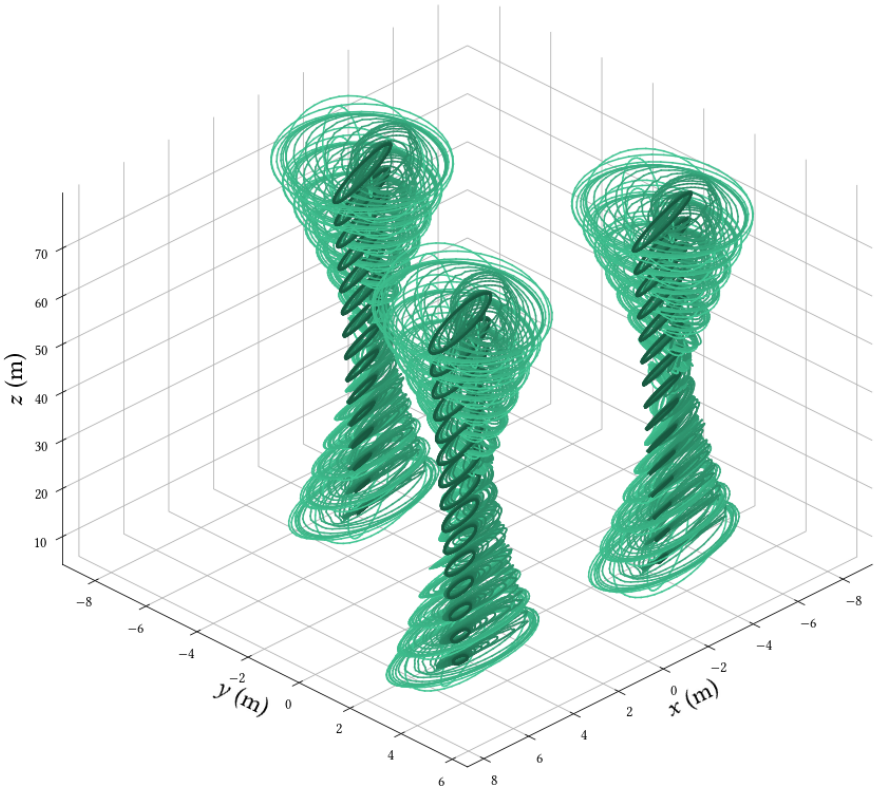

Figure 6.7: Three-dimensional time-trace of the position of the legs.

Lastly, the resulting chord loads are plotted in Figure 6.8. A positive chord load naturally corresponds to tension, which is the load state the chord takes on in the beginning, as it is hanging on the pinions. It can be observed that the amplitude of the loads are temporarily increased during the spudcan penetration phase and also changes signs quite often, as predicted in Section 1.1.5. Once platform lifting commences, a clear trend towards compression chord loads is visible, because the buoyancy of the hull decreases. The inclusion of backlash in the rack-and-pinion interface is clear: when the load direction changes, the rack and pinion are temporarily disconnected. At that moment, no force transfer takes place. Especially during leg lowering, $t \in [0\,\text{s}, 45\,\text{s}]$, when the leg is freely hanging in the pinions, gravity ensures the mechanical contact is kept. This is why no negative loads are found. Only after impact loads have become large enough, at $t \approx 90\,\text{s}$, impact loads cause the leg to be displaced upwards more than the backlash distance, so that negative forces arise.

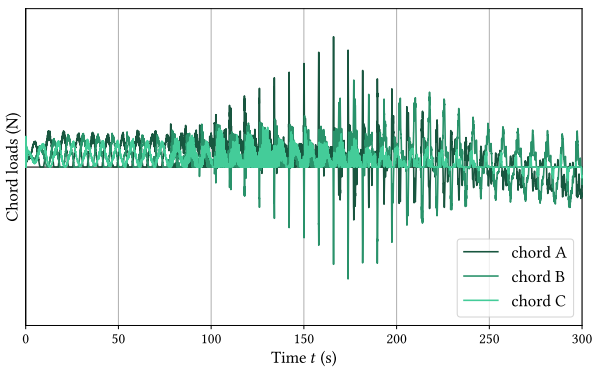

Figure 6.8: Axial loads of the chords.

6.1.3 || Seabed reaction forces

The interaction of the leg with the seabed is characterised by the spudcan-and-seabed interface. In Figures 6.9–6.12, the surge and heave components of the spudcan-and-seabed interface are plotted. By careful inspection of the graphs, it can be seen that the seabed only reacts in compression, such that energy is dissipated to the seabed. The physical reasoning for this is addressed in Section 5.2.5. It can also be observed that heave reaction forces from the seabed increase with every impact, as the spudcan is penetrating further into the seabed.

When the platform lifting phase comments, at $t \approx 220$ s, the spudcan behaves like a jack-hammer. This is because of the condition that forces only arise when it compresses the seabed, i.e., when the spudcan moves downwards: seabed gives a reaction force to the spudcan, the spudcan velocity becomes positive, the seabed reaction force vanishes, the spudcan velocity becomes negative again and a seabed reaction forces is developed, and it is repeated. This jack-hammering has no effect on the results, as it is filtered out by the internal structural damping of the leg, but increases computational time nonetheless. Furthermore, whereas before $t \approx 220$ s the seabed reaction forces contained only low-frequency characteristics with a period of 8 s, after $t \approx 220$ s mainly high-frequency characteristics are observed. To continue simulating the platform lifting phase as well, another spudcan-and-seabed model should be adopted instead.

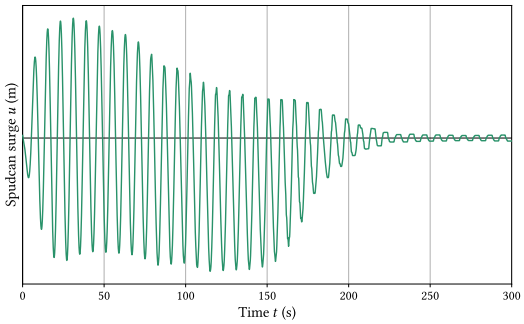

Figure 6.9: Surge of the spudcan.

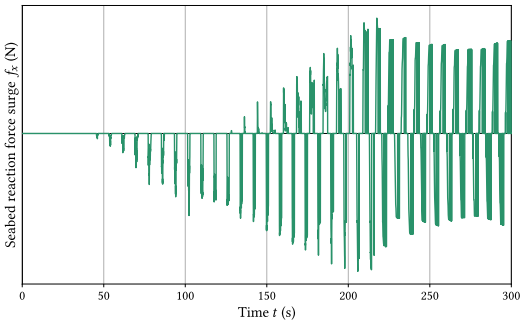

Figure 6.10: Surge reaction force of the seabed .

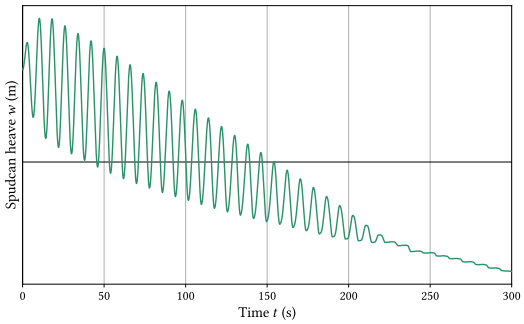

Figure 6.11: Heave of the spudcan.

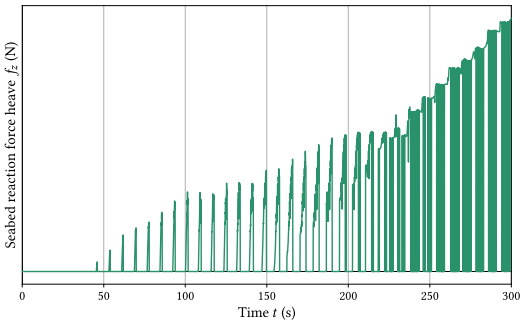

Figure 6.12: Heave reaction force of the seabed .

6.1.4 || Leg bending moment

The last global dynamic phenomenon is the connection between the leg and the hull, which is characterised by the leg bending moment. Naturally, this bending moment is found in both roll and pitch directions. The pitch leg bending moment is the largest of the two, as the wave direction is 30°. It can be observed that the dimensionless ratio β of 0.6 is indeed observed, as the moments transferred by the jacking systems are slightly larger than that of the guides.

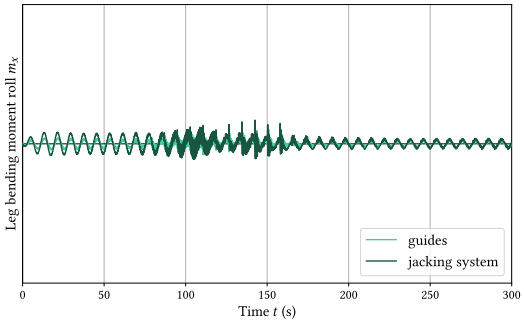

Figure 6.13: Roll leg-bending moment m_x.

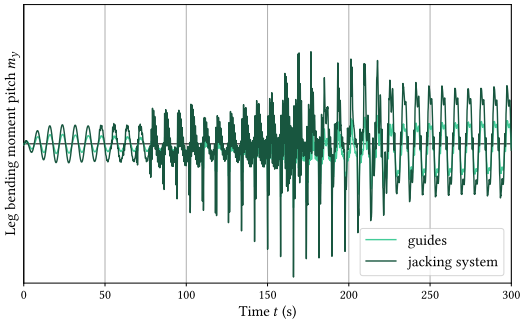

Figure 6.14: Pitch leg-bending moment m_y.

6.2 | Dynamics of the jacking systems

This section has been removed as it contains confidential information provided by the research partner GustoMSC

6.3 | Sensitivity of the model to parameters changes

This section has been removed as it contains confidential information provided by the research partner GustoMSC

| Concluding remarks

This section has been removed as it contains confidential information provided by the research partner GustoMSC

part IV

Discussion and conclusion

chapter 7

Discussion and recommendations

The simulation model is able to simulate the dynamics of a one-legged WTIV subjected to gravity and wave-exciting forces, including the dynamics, currents and torques of the jacking systems as function of the voltage given by the control systems. In the process of creating this model, a few assumptions have been considered in order to simplify equations and increase performance of the integration. The consequences of these assumptions on the results are interpreted and discussed in this chapter. Additionally, recommendations for further research are given.

7.1 | The sea model

First of all, the sea model is relatively simplified. Only one incident oblique wave is considered which is described predominantly by its wave period. Consequently, results show that this wave period is dominant among the dynamics of the WTIV and the jacking systems. In reality however, the sea is described by a spectrum with a certain peak wave period. A single incident oblique wave with this peak period compared to a spectrum, delivers more unconservative results. For further research, it is recommended to include a sea state from a spectrum.

7.2 | Wind turbine installation vessel design: hull and leg

The design of the WTIV used in this simulation model is simplified. Conventionally, WTIVs contain four or six legs, whereas this model contains only one leg. This simplification was added to significantly reduce computational time and memory, and because the effects of spudcan penetration are confined to the legs. Consequently, the simulation model is not one-to-one comparable with actual WTIVs, mainly because the legs are loaded differently. In the simulation model, an externally applied moment to the hull results in opposing chord loads, whereas in reality, this results in non-opposing leg loads with slight variations between the chords, as schematised in Figure 7.1.

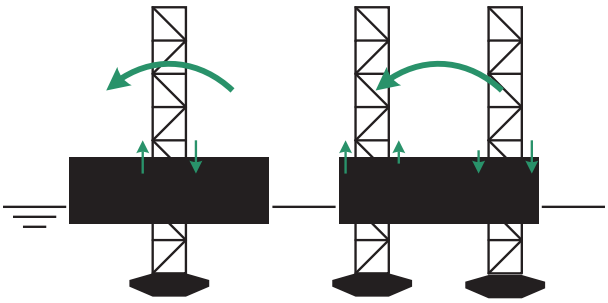

Figure 7.1: Difference in chord and leg loads between this simulation model and reality.

For further research, it is recommend to expand the model to include four or six legs and investigate the efficacy of the control strategies. Based on the results found in this thesis and the difference in loading as visualised in Figure 7.1, a hypothesis can be formulated. In this thesis, the multi-inverter strategy with common setpoint per chord is somewhat equivalent to a multi-inverter strategy with common setpoint per leg in reality. Additionally, in this thesis the multi-inverter strategy with common setpoint per leg, would be somewhat equivalent to a single setpoint for the entire WTIV in reality. Naturally, it is expected that the former of these two provides better performance and stability.

Another difference between the design of the WTIV in this thesis and reality is the geometry of the hull. In this thesis, a simplified rectangular uniform barge is adopted in order to at least provide hydrodynamics and

wave-exciting forces. In reality, the hull is shaped like a conventional seagoing vessel and thus for further research when four or six legs are considered, it is recommended to improve the geometry of the hull. Furthermore, the wave-exciting forces and hydrodynamics on the hull are calculated for the initial draught of the hull, even though these are function of draught. As the hull is lifted out of the water—resulting in decreasing draught—these hydrodynamics and wave-exciting forces are only valid for a small reduction of draught. In order to further simulate platform lifting, it is required, and thus recommend for further research, to make this draught-dependent.

7.3 | The spudcan-and-seabed model

In this thesis, non-linear penetration curves for spudcan penetration are created using the well-established CEL-method as described in literature. These non-linear penetration curves were implemented in such a manner, that they only provide reaction forces when the sign of displacement and velocity of the spudcan are equal, as seen in literature. Consequence of this implementation is that energy is dissipated to the seabed which is realistic and beneficial, but it also causes high-frequency dynamics to be introduced after the spudcan has settled—when platform lifting commences. In order to continue simulating this platform lifting, it is recommend to adopt another spudcan-and-seabed model such as the ones described in Section 3.2.4.1.

Another consequence of this spudcan-and-seabed model is that, contrary to expectations, it is not the impact with the seabed that is crucial—causing the control system to strongly respond, but the sudden disappearance of the seabed reaction force that is, as this gives a sudden large error. In reality the seabed permanently deforms when the spudcan penetrates it such that with every impact the seabed becomes stiffer, such that seabed reaction forces are not gradual. Thus, when such a realistic seabed model with permanent deformations is considered, it is expected that the sudden appearance of the seabed reaction forces also causes a strong response of the control system.

Furthermore, a certain amount of backfill is present in reality, which is material resting on top of the spudcan. This effect and permanent deformation are not included in this thesis. Such models with permanent deformation and backfill for spudcan penetration are not found in literature and it is outside the scope of this thesis to develop these.

Lastly, it is recommend to simulate the efficacy of the control strategies in response to a non-homogeneous seabed, such as a multi-layered seabed. Such seabed is a more accurate representation or reality. In case a softer clay layer is positioned between two sand layers, the response to so-called punch-through can be evaluated. With the CEL-method such a multi-layered seabed and their penetration curves are obtained equally straightforward as a single-layered seabed.

7.4 | The control systems

The Volts-per-Hertz (V/Hz) control strategies allowed the voltage output of the control systems to be idealised by a perfect sine wave. Consequently, the resulting currents, torque and dynamics of the jacking systems do not contain any high-frequency components or ripples. The direct torque control (DTC) control strategy does not permit an idealised output, as its voltage output are arbitrary pulses. Naturally, the inductive components of the induction motor circuit provide filtering such that the resulting currents are continuous, as explained in Section 4.1.4.2. Nevertheless, a relatively high solution frequency is required as otherwise ripples are present in the currents and torque.

Throughout the simulations with DTC-controllers, the integration algorithm was given a lower limit of 5000 Hz and each simulation required about 90 min to complete. The results presented significant ripples, though these did not cause any global numerical errors—as it were, this solution with ripples oscillated around the perfect ripple-free solution. By increasing the solution frequency—i.e. the inverter carrier frequency—the ripples decreased at the cost of significant increased computational time and memory. Unfortunately for the simulation time of 300 s, it was not possible to increase the frequency beyond 5000 Hz due to computational limitations. For this reason, only for a region of interest the frequency was temporarily increased to 25 000 Hz in order to study the dynamics, currents and torques without any disturbances in the data. The difference is for the same time period is shown in Figure 7.2 and its consequence is ostensible.

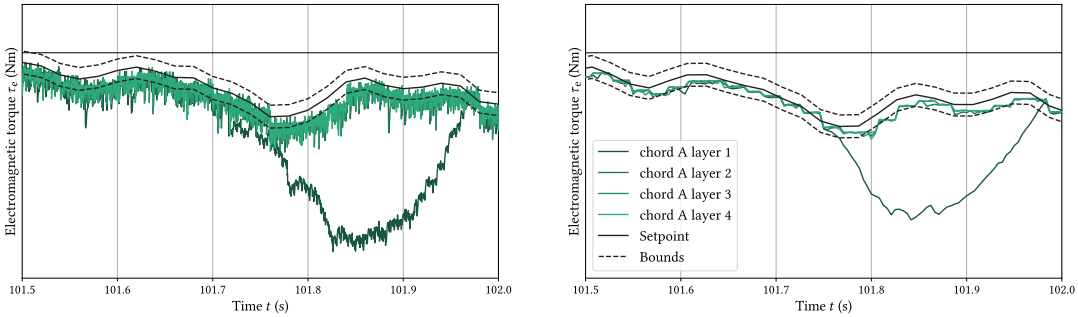

Figure 7.2: Difference between an inverter frequency of 5000 Hz (left) and 25 000 Hz (right).

chapter 8

Conclusion

The research objective of this thesis is to address the knowledge gap on the modelling of the dynamics of WTIVs as there is no model found in literature that is able simulate the dynamics of WTIVs in great detail, including the dynamics of the jacking systems and the interaction with its control system. This thesis has successfully addressed this gap by developing a novel, detailed simulation model *Salacia* that is able to:

- simulate the dynamics of a simplified, one-legged WTIV:
  - dynamics of a simplified rectangular hull;
  - dynamics of a detailed three-dimensional truss leg;
  - dynamics of detailed jacking systems, including pinions, gearboxes and machine rotors;
- simulate the interaction between these bodies via a novel leg-and-hull interface:
  - horizontal force transfer between leg and hull via contact between rack and guide;
  - vertical force transfer between leg, hull and jacking systems via contact between rack and pinion;
- simulate the interaction between the seabed and the spudcan;
- simulate the two-way interaction between dynamics and induction machine control systems:
  - the interaction from control system to dynamics via its torque setpoint;
  - the interaction from dynamics to control system via load torque on the machine rotor;
- simulate the transition from leg lowering to platform lifting, via the transient spudcan penetration phase

Furthermore, methods have been established in order to derive certain parameters and relations:

- hydrodynamics and wave-exciting forces via the Python module Capytaine;
- seabed penetration curves in all DOF except yaw with the CEL models;
- stiffness between the rack and the pinion via FE models.

The efficacy of multiple control laws and strategies has been investigated. It has been shown that to achieve load-sharing between multiple machines, 1) a control law should be used that is able to control torque and velocity independently, such as DTC-controllers, and 2) a suitable multi-machine strategy should be adopted. Multi-machine strategies are characterised by whether an inverter supplies one or multiple induction machines. Multi-inverter strategies, where each jacking system is supplied with its own inverter, are required in order to achieve load-sharing. Best stability and performance is achieved when a common setpoint is given to all jacking systems that are loaded equally by the environmental conditions, i.e. the waves. In this thesis with a simplified WTIV, the chords are loaded asynchronously such that the best performance and stability is achieved when chords are given a common setpoint.

Furthermore, because the wave-exciting forces are periodical, either the velocity or torque of the induction machines, or both, should be periodical as well in order to absorb these loads. This is determined by the choice of control strategy. It is most beneficial if these environmental loads are predominantly taken by the torque, such that the physical consequences are absent. With the common setpoint per chord, this is the case.

Lastly, even with load-sharing capabilities of the multi-machine strategies with DTC-controllers, during spudcan penetration the bottom layer deviated from the setpoint. As it turns out, the relative stiffness between the leg chords and the rack-and-pinion interface is a governing parameter in inherent load-sharing characteristics. By increasing this ratio, the loads are inherently increasingly symmetrically distributed.

References

Adam, J.-P., & Varène, P. (2008). Le castellum aquae de pompéi, étude architecturale. *Revue Archéologique*, *1*(45), 37-72.

Ancellin, M. (2023). *Capytaine: a python-based distribution of nemoh.* `https://ancell.in/capytaine/latest/index.html`. (Accessed: 5 July 2023)

Bienen, B., & Cassidy, M. J. (2006). Three-dimensional dynamic analysis of jack-up structures. *Advances in Structural Engineering*, *9*(1), 19–37. doi: https://doi.org/10.1260/136943306776232873

Boswell, L. F. (2018). The jack-up platform overview. In J. Carlton, P. Jukes, & Y.-S. Choo (Eds.), *Encyclopedia of maritime and offshore engineering* (1st ed., Vol. 4, p. 2695-2702). John Wiley & Sons, Ltd.

Brunton, S. L., & Kutz, J. N. (2019). *Data driven science and engineering.* Cambridge, United Kingdom: Cambridge University Press.

Buitendijk, M. (2022). *Huisman launches floating installation of wind turbines with windfarm installation vessel.* `https://swzmaritime.nl/news/2022/04/22/huisman-launches-floating-installation-of-wind-turbines-with-windfarm-installation-vessel/`. (Accessed: 4 July 2023)

Cassidy, M., & Houlsby, G. T. (1999, 05). *On the Modelling of Foundations for Jack-up Units on Sand* (Vol. All Days). Retrieved from `https://doi.org/10.4043/10995-MS` (OTC-10995-MS) doi: 10.4043/10995-MS

Chakrabarti, S. K. (1994). *Hydrodynamics of offshore structures.* WIT Press.

Chopra, A. K. (2014). *Dynamics of structures.* Harlow, England: Pearson.

Cowper, G. (1966). The Shear Coefficient in Timoshenko's Beam Theory. *Journal of Applied Mechanics*, *33*(2), 335-340.

DNV. (2022, February). *Self-elevating units* (Tech. Rep. No. DNV-RP-C104). Høvik, Norway: Author.

Friedland, B. (1986). *Control System Design: An Introduction to State-Space Methods.* Mineola, United States of America: Dover Publications, Inc.

Golnaraghi, F., & Kuo, B. C. (2010). *Automatic Control Systems.* United States of America: John Wiley & Sons, Inc.

Heo, S., Koo, W., & Park, M.-S. (2016). Dynamic Response and Reliability of Six-Leg Jack-Up Type Wind Turbine Installation Vessel. *International Journal of Structural Stability and Dynamics*, *17*(3), 1750037.

Hoeijmakers, M. J. (2004). *Modelling of ac machines.* Lecture notes.

Holthuijsen, L. H. (2007). *Waves in Oceanic and Coastal Waters.* Cambridge University Press.

Hosker, E., & Justus, D. (2019, November). *Offshore Wind Outlook 2019* (Tech. Rep.). Paris, France: International Energy Agency.

Hutchinson, M., & Zhao, F. (2023). *Global wind report 2023* (Tech. Rep.). Brussels, Belgium: Global Wind Energy Council.

International Marine Contractors Association. (n.d.). *Introduction to dynamic positioning.* `http://marineengineering.co.za/lectures/technical-information/general-docs/dynamic-positioning.pdf`. (Accessed: 10 February 2023)

ISO. (2015, January). *Petroleum and natural gas industries — site-specific assessment of mobile offshore units — part 1: Jack-ups* (Tech. Rep. No. ISO 19905-1). Geneva, Switzerland: Author.

Katsikadelis, J. T. (2020). *Dynamic analysis of structures.* Academic Press.

Kolios, A., & Lozano-Minguez, E. (2018). Offshore wind energy technology. In J. Carlton, P. Jukes, & Y.-S. Choo (Eds.), *Encyclopedia of maritime and offshore engineering* (1st ed., Vol. 6, p. 3551-3564). John Wiley & Sons, Ltd.

Koole, T. (2015). *Modern Jack-Ups and their Dynamic Behaviour* (Unpublished master's thesis). Delft University of Technology, Delft, the Netherlands.

Krause, P., Wasynczuk, O., Sudhoff, S., & Pekarek, S. (2013). *Analysis of Electric Machinery and Drive Systems.* Hoboken, United States of America: John Wiley & Sons, Ltd.

Kreuzer, E., Solowjow, E., Qiu, G., Hamann, T., & Grabe, J. (2014, 06). *Leg-seabed interactions of jack-up vessels due to motions in irregular waves* (Vol. 1B). Retrieved from https://doi.org/10.1115/OMAE2014-24303 (OMAE2014-24303)

Martin, C. M. (1994). *Physical and numerical modelling of offshore foundations under combined loads* (Unpublished doctoral dissertation). University of Oxford, Oxford, United Kingdom.

Ortega, R. E. A. (2016). *Global response analysis of wind turbine installation vessels in semi-submerged condition. a modified quasi-static approach* (Unpublished master's thesis). West Pomeranian University of Technology, Szczecin, Poland.

Przemieniecki, J. (1968). *Theory of matrix structural analsysis.* New York, United States of America: Dover Publications, Inc.

SciPy Developers. (n.d.). *Scipy user guide.* https://docs.scipy.org/doc/scipy/tutorial/index.html#user-guide. (Accessed: 3 July 2023)

Scruggs, J. T., & Gavin, H. P. (2011). Earthquake response control for civil structures. In W. S. Levine (Ed.), *Control system applications* (2nd ed., chap. 30). CRC Press.

Serraris, J., Carinato, A., Huijs, F., Hofstede, H., & Luger, D. (2017, 09). *Jack-up motion response and leg to seabed impact loads during installation at site: comparison of model tests and simulations.*

Sonnema, W. (2019). *3D FE analysis of four legged jack-up vessels during preloading in cohesive soil* (Unpublished master's thesis). Delft University of Technology, Delft, the Netherlands.

Suyderhoud, J., & Vleugels, T. (2016). *Past, present and future: 150 years of heritage.* Schiedam, the Netherlands: GustoMSC.

Tho, K. K., Leung, C. F., Chow, Y. K., & Swaddiwudhipong, S. (2012). Eulerian finite-element technique for analysis of jack-up spudcan penetration. *International journal of geomechanics*, *12*(1), 64–73.

Timoshenko, S. P. (1921). On the correction for shear of the differential equation for transverse vibrations of prismatic bars. *The London, Edinburgh, and Dublin Philosophical Magazine and Journal of Science*, *41*(245), 744-–746.

Timoshenko, S. P., & Gere, J. M. (1961). *Theory of elastic stability.* McGraw-Hill Book Company, Inc.

Trinomics. (2020, October). *Final report cost of energy (lcoe)* (Tech. Rep.). Brussels, Belgium: European Commission.

Vazquez, J., Grasso, B., Gamino, M., & Templeton, J. (2017, 09). *Seabed modeling effects on jack-up response while going on location.*

Vugts, J. (1970). *The hydrodynamic forces and ship motions in waves* (Unpublished doctoral dissertation). Delft University of Technology, Delft, the Netherlands.

Wildi, T. (2014). *Electrical Machines, Drives and Power Systems.* Harlow, United Kingdom: Pearson Education Limited.

Williams, M., Thompson, R., & Houlsby, G. (1998). Non-linear dynamic analysis of offshore jack-up units. *Computers & Structures*, *69*(2), 171-180. Retrieved from https://www.sciencedirect.com/science/article/pii/S0045794998001199 doi: https://doi.org/10.1016/S0045-7949(98)00119-9

Wu, J.-S., & Chang, C.-Y. (1988). Structural simplification of jack-up rig and its dynamic responses in regular waves. *Journal of Ship Research*, *32*(2), 134–153.

Zheng, Y.-K., Zhang, S.-L., & Lai, L. (2015). Load Distribution of the Hull-Leg Connection Components of a Jack-Up. *Journal of Shanghai Jiaotong University (Science)*, *20*(6), 721–728.

Ziegler, J., & Nichols, N. (1942). Optimum Settings for Automatic Controllers. *Transactions of the ASME*, *64*, 759-768.

part V

Appendices

appendix A

Derivation of the element matrices

This appendix chapter presents the calculations performed in order to derive the complete element stiffness and element mass matrices for a three-dimensional beam element. A general procedure is considered in line with Chapter 2, which includes shear and rotary inertia effects.

A.1 | Derivation of the element stiffness matrix

The derivation of the element stiffness matrix for a beam element $\mathbf{K}_e$ is obtained by subjecting it to unit displacements

$$\boldsymbol{\xi} \equiv \begin{pmatrix} u_1 & v_1 & w_1 & \vartheta_1 & \varphi_1 & \psi_1 & u_2 & v_2 & w_2 & \vartheta_2 & \varphi_2 & \psi_2 \end{pmatrix}^{\mathrm{T}} \tag{A.1}$$

of the twelve DOF. The application of these unit displacements causes the beam to deform. Naturally, the magnitude of these deformations is determined by the stiffness of the beam element $\mathbf{K}_e$. This deformation is described analytically with beam theory: $u(x)$ describes the axial deformation caused by u_1 and u_2, $\vartheta(x)$ describes the torsional deformation caused by ϑ_1 and ϑ_2, $v(x)$ describes transverse bending caused by v_1, v_2. ψ_1 and ψ_2, and $w(x)$ describes vertical bending caused by w_1, w_2. φ_1 and φ_2. Naturally, these deformations induce strains $\boldsymbol{\varepsilon}(x, y, z)$ and stresses $\boldsymbol{\sigma}(x, y, z)$ in the beam element. Axial, transverse bending, vertical bending, torsional, transverse shear and vertical shear strains and stresses are understood, such that

$$\boldsymbol{\varepsilon}(x, y, z) = \begin{pmatrix} \varepsilon_u & \varepsilon_v & \varepsilon_w & \gamma_\vartheta & \gamma_v & \gamma_w \end{pmatrix}^{\mathrm{T}} \tag{A.2a}$$

$$\boldsymbol{\sigma}(x, y, z) = \begin{pmatrix} \sigma_u & \sigma_v & \sigma_w & \tau_\vartheta & \tau_v & \tau_w \end{pmatrix}^{\mathrm{T}} \tag{A.2b}$$

These strains and stresses are function of the unit displacements $\boldsymbol{\xi}$ by the relation

$$\boldsymbol{\varepsilon}(x, y, z) \equiv \mathbf{S}(x, y, z) \cdot \boldsymbol{\xi} \tag{A.3a}$$

$$\boldsymbol{\sigma}(x, y, z) \equiv \mathbf{E} \cdot \boldsymbol{\varepsilon}(x, y, z) = \mathbf{E} \cdot \mathbf{S}(x, y, z) \cdot \boldsymbol{\xi} \tag{A.3b}$$

where $\mathbf{S}(x, y, z)$ is a matrix relating the unit displacements $\boldsymbol{\xi}$ to the strains $\boldsymbol{\varepsilon}(x, y, z)$ and $\mathbf{E}$ is a diagonal elasticity matrix relating stresses to the strains (Przemieniecki, 1968). Similarly, these matrices can be divided into the components as

$$\mathbf{S}(x, y, z) = \begin{pmatrix} \mathbf{s}_u & \mathbf{s}_v & \mathbf{s}_w & \mathbf{s}_\vartheta & \mathbf{s}_\varphi & \mathbf{s}_\psi \end{pmatrix}^{\mathrm{T}} \tag{A.4a}$$

$$\mathbf{E} = \left\langle E_u \;\; E_v \;\; E_w \;\; E_\vartheta \;\; E_\varphi \;\; E_\psi \right\rangle_{\mathrm{diag}} \tag{A.4b}$$

It then follows that the element structural stiffness matrix $\mathbf{K}_e$ is found by integrating the strain energy over the volume of the beam, and is given by Przemieniecki (1968) as

$$\mathbf{K}_e \equiv \int_V \mathbf{S}^{\mathrm{T}} \mathbf{E} \mathbf{S} \, \mathrm{d}V \tag{A.5}$$

For each of the four equations describing the beam deformation, these matrices are derived.

Axial deformations: beam subjected to u_1 and u_2

The differential equation describing axial deformations of a beam is given as

$$\frac{\mathrm{d}^2 u}{\mathrm{d}x^2} = 0 \tag{A.6}$$

With unit displacements $u(0) = u_1$ and $u(l) = u_2$ the solution to this differential equation is

$$u(x) = u_1 + (u_2 - u_1)\frac{x}{l} \tag{A.7}$$

Only normal strain and stresses arise due to these unit displacements. The axial normal strains $\varepsilon_u(x)$ and stresses $\sigma_u(x)$ can be readily obtained by differentiating $u(x)$,

$$\varepsilon_u(x) = \frac{\mathrm{d}}{\mathrm{d}x}u(x) = \frac{u_2 - u_1}{l} = \mathbf{s}_u\boldsymbol{\xi} \tag{A.8a}$$

$$\sigma_u(x) = E\frac{\mathrm{d}}{\mathrm{d}x}u(x) = E\left(\frac{u_2 - u_1}{l}\right) = E_u\mathbf{s}_u\boldsymbol{\xi} \tag{A.8b}$$

From this the axial components $\mathbf{s}_u$ and E_u of the matrices $\mathbf{S}$ and $\mathbf{E}$ are found as

$$\mathbf{s}_u = \frac{1}{l}\begin{pmatrix}-1 & 0 & 0 & 0 & 0 & 0 & 1 & 0 & 0 & 0 & 0 & 0\end{pmatrix} \tag{A.9a}$$

$$E_u = E \tag{A.9b}$$

Transverse bending: beam subjected to v_1, v_2. ψ_1 and ψ_2

Conventionally, the resulting deformation of a beam element under transverse displacements is described by the Euler-Bernoulli beam theory (Chopra, 2014). The Euler-Bernoulli beam theory for beams without distributed load, is described by

$$EI_z\frac{\mathrm{d}^4 v}{\mathrm{d}x^4} = 0 \tag{A.10a}$$

$$EI_z\frac{\mathrm{d}^3 v}{\mathrm{d}x^3} = -V(X) \tag{A.10b}$$

$$EI_z\frac{\mathrm{d}^2 v}{\mathrm{d}x^2} = -M(x) \tag{A.10c}$$

$$\frac{\mathrm{d}v}{\mathrm{d}x} = \psi(x) \tag{A.10d}$$

The general solution to Equation A.10a is a cubic polynomial,

$$v(x) = c_0 + c_1 x + c_2 x^2 + c_3 x^3 \tag{A.11}$$

As this section describes a general procedure, the Timoshenko beam theory is applied, which includes shear effects. The Timoshenko beam theory for beams without distributed load adds the following correction to the angle $\psi(x)$ of the neutral axis (Timoshenko, 1921)

$$\psi(x) = \frac{\mathrm{d}v}{\mathrm{d}x} + \frac{EI_z}{GA_s}\frac{\mathrm{d}^3 v}{\mathrm{d}x^3} \tag{A.12}$$

With the unit displacements $v(0) = v_1$, $v(l) = v_2$, $\psi(0) = \psi_1$ and $\psi(l) = \psi_2$ the unknown coefficients are determined to yield

$$\begin{aligned} v(x) = v_1 &- \frac{l\Theta_z\psi_2 - l\Theta_z\psi_1 - 2\mathrm{S}\psi_1 - 2\Theta_z v_2 + 2\Theta_z v_1}{2(\Theta_z + 1)}\frac{x}{l} \\ &+ \frac{l\Theta_z\psi_2 - l\Theta_z\psi_1 - 2l\psi_2 - 4l\psi_1 + 6v_2 - 6v_1}{2(\Theta_z + 1)}\frac{x^2}{l^2} + \frac{l\psi_2 + l\psi_1 - 2v_2 + 2v_1}{(\Theta_z + 1)}\frac{x^3}{l^3} \end{aligned} \tag{A.13}$$

where

$$\Theta_z \equiv \frac{12EI_z}{GA_s l^2} \tag{A.14}$$

Due to the transverse displacements, normal bending strains $\varepsilon_v(x,y)$ and stresses $\sigma_v(x,y)$ are developed as well as shear strains $\gamma_v(x)$ and stresses $\tau_v(x)$. These normal strains $\varepsilon_v(x,y)$ are found by the relation

$$\begin{aligned}\varepsilon_v(x,y) &= -y\frac{\mathrm{d}^2 v}{\mathrm{d}x^2} = \mathbf{s}_v\boldsymbol{\xi} \\ &= y\left(-\frac{(l^2\Theta_z - 2l^2)\psi_2 - (l^2\Theta_z + 4l^2)\psi_1 + 6lv_2 - 6lv_1}{l^3(\Theta_z+1)} - 6x\frac{l\psi_2 + l\psi_1 - 2v_2 + 2v_1}{l^3(\Theta_z+1)}\right)\end{aligned} \tag{A.15}$$

and the normal stresses $\sigma_v(x,y)$ by the relation

$$\sigma_v(x,y) = E\varepsilon_v(x,y) = E_v\mathbf{s}_v\boldsymbol{\xi} \tag{A.16}$$

such that

$$\mathbf{s}_v = \frac{y}{l^3(\Theta_z+1)}\begin{pmatrix}0 & 6l-12x & 0 & 0 & 0 & l^2\Theta_z+4l^2-6lx & 0 & -6l+12x & 0 & 0 & 0 & -l^2\Theta_z+2l^2-6lx\end{pmatrix} \tag{A.17a}$$

$$E_v = E \tag{A.17b}$$

Similarly, the shear strains $\gamma_v(x)$ are found by the relation

$$\gamma_v(x) = \frac{\mathrm{d}v}{\mathrm{d}x} - \psi(x) = \Theta_z\frac{-l\psi_2 - l\psi_1 + 2v_2 - 2v_1}{2l(\Theta_z+1)} = \mathbf{s}_\psi\boldsymbol{\xi} \tag{A.18}$$

and the shear stresses $\tau_v(x)$ by the relation

$$\tau_v(x) = G\gamma_v(x) = E_\psi\mathbf{s}_\psi\boldsymbol{\xi} \tag{A.19}$$

such that

$$\mathbf{s}_\psi = \frac{\Theta_z}{2l(\Theta_z+1)}\begin{pmatrix}0 & -2 & 0 & 0 & 0 & -l & 0 & 2 & 0 & 0 & 0 & -l\end{pmatrix} \tag{A.20a}$$

$$E_\psi = G \tag{A.20b}$$

Vertical bending: beam subjected to w_1, w_2. φ_1 and φ_2

The derivation of the vertical deformations $w(x)$ is similar to that of the transverse deformations $v(x)$, yielding

$$\mathbf{s}_w = \frac{z}{l^3(\Theta_y+1)}\begin{pmatrix}0 & 0 & 6l-12x & 0 & -l^2\Theta_y-4l^2+6lx & 0 & 0 & 0 & -6l+12x & 0 & l^2\Theta_y-2l^2+6lx & 0\end{pmatrix} \tag{A.21a}$$

$$E_w = E \tag{A.21b}$$

$$\mathbf{s}_\varphi = \frac{\Theta_y}{2l(\Theta_y+1)}\begin{pmatrix}0 & 0 & -2 & 0 & l & 0 & 0 & 0 & 2 & 0 & l & 0\end{pmatrix} \tag{A.21c}$$

$$E_\varphi = G \tag{A.21d}$$

Axial torsion: beam subject to ϑ_1 and ϑ_2

The differential equation describing axial rotations of a beam is given as:

$$\frac{\mathrm{d}^2\vartheta}{\mathrm{d}x^2} = 0 \tag{A.22}$$

With boundary conditions $\vartheta(0) = \vartheta_1$ and $\vartheta(l) = \vartheta_2$ the solution to this differential equation is

$$\vartheta(x) = \vartheta_1 + (\vartheta_2 - \vartheta_1)\frac{x}{l} \tag{A.23}$$

Only torsional shear strains and stresses arise due to these unit displacements. The torsional shear strains and stresses can be readily obtained by differentiating $\vartheta(x)$

$$\gamma_\vartheta(x) = r\frac{\mathrm{d}}{\mathrm{d}x}\vartheta(x) = r\frac{\vartheta_2 - \vartheta_1}{l} = \mathbf{s}_\vartheta \boldsymbol{\xi} \tag{A.24a}$$

$$\tau_\vartheta(x) = Gr\frac{\vartheta_2 - \vartheta_1}{l} = E_\vartheta \mathbf{s}_\vartheta \boldsymbol{\xi} \tag{A.24b}$$

where r is the distance from the $x-$axis. From this $\mathbf{s}_\vartheta$ and E_ϑ is found:

$$\mathbf{s}_\vartheta = \frac{r}{l}\begin{pmatrix}0 & 0 & 0 & -1 & 0 & 0 & 0 & 0 & 0 & 1 & 0 & 0\end{pmatrix} \tag{A.25a}$$

$$E_\vartheta = G \tag{A.25b}$$

Element stiffness matrix

The product $\mathbf{S}^\mathrm{T}\mathbf{E}\mathbf{S}$ can be evaluated and integrated over the volume of the beam so that the resulting element stiffness matrix is given below. By virtue of Newton's Third Law the matrix is symmetric.

$$\mathbf{K}_\mathrm{e} = \begin{bmatrix}
\frac{EA}{l} & 0 & 0 & 0 & 0 & 0 & -\frac{EA}{l} & 0 & 0 & 0 & 0 & 0 \\
 & \frac{12EI_z}{l^3(1+\Theta_z)} & 0 & 0 & 0 & \frac{6EI_z}{l^2(1+\Theta_z)} & 0 & -\frac{12EI_z}{l^3(1+\Theta_z)} & 0 & 0 & 0 & \frac{6EI_z}{l^2(1+\Theta_z)} \\
 & & \frac{12EI_y}{l^3(1+\Theta_y)} & 0 & -\frac{6EI_y}{l^2(1+\Theta_y)} & 0 & 0 & 0 & -\frac{12EI_y}{l^3(1+\Theta_y)} & 0 & -\frac{6EI_y}{l^2(1+\Theta_y)} & 0 \\
 & & & \frac{Gj}{l} & 0 & 0 & 0 & 0 & 0 & -\frac{Gj}{l} & 0 & 0 \\
 & & & & \frac{EI_y(4+\Theta_y)}{l(1+\Theta_y)} & 0 & 0 & 0 & \frac{6EI_y}{l^2(1+\Theta_y)} & 0 & \frac{EI_y(2-\Theta_y)}{l(1+\Theta_y)} & 0 \\
 & & & & & \frac{EI_z(4+\Theta_z)}{l(1+\Theta_z)} & 0 & -\frac{6EI_z}{l^2(1+\Theta_z)} & 0 & 0 & 0 & \frac{EI_z(2-\Theta_z)}{l(1+\Theta_z)} \\
 & & & & & & \frac{EA}{l} & 0 & 0 & 0 & 0 & 0 \\
 & & & & & & & \frac{12EI_z}{l^3(1+\Theta_z)} & 0 & 0 & 0 & -\frac{6EI_z}{l^2(1+\Theta_z)} \\
 & & & & & & & & \frac{12EI_y}{l^3(1+\Theta_y)} & 0 & \frac{6EI_y}{l^2(1+\Theta_y)} & 0 \\
 & & & & & & & & & \frac{Gj}{l} & 0 & 0 \\
 & & & & & & & & & & \frac{EI_y(4+\Theta_y)}{l(1+\Theta_y)} & 0 \\
 & \text{sym} & & & & & & & & & & \frac{EI_z(4+\Theta_z)}{l(1+\Theta_z)}
\end{bmatrix} \tag{A.26}$$

A.2 | Derivation of the consistent element mass matrix

The consistent element mass matrix is a matrix that is derived using the same method as the element stiffness matrix: by using the four equations that describe the deformation of the beam due to the unit displacements. Let

$$\bar{\boldsymbol{\xi}} \equiv \begin{pmatrix}\bar{u}(x,y,z) & \bar{v}(x,y,z) & \bar{w}(x,y,z)\end{pmatrix}^\mathrm{T} \tag{A.27}$$

be a vector that describes the three-dimensional displacement of the element at (x, y, z) in response to the unit displacements $\boldsymbol{\xi}$. The resulting displacement is composed of axial displacement $\bar{u}(x, y, z)$, transverse displacement $\bar{v}(x, y, z)$ and vertical displacement $\bar{w}(x, y, z)$, which are related to the six beam equations by

$$\bar{u}(x,y,z) = u(x) - y\cdot\psi(x) + z\cdot\varphi(x) \tag{A.28a}$$

$$\bar{v}(x,y,z) = v(x) - z\cdot\vartheta(x) \tag{A.28b}$$

$$\bar{w}(x,y,z) = w(x) + y\cdot\vartheta(x) \tag{A.28c}$$

As this considers a general procedure, the rotation of the cross-section is also included which adds the transverse angle of the neutral axis $\psi(x)$ and vertical angle of the neutral axis $\varphi(x)$, so-called rotary inertia effects. Similarly to how the stresses and strains are related to the unit displacements $\boldsymbol{\xi}$ by the matrices $\mathbf{S}$ and $\mathbf{E}$, the total displacement of any point $\bar{\boldsymbol{\xi}}$ can be related to the unit displacements $\boldsymbol{\xi}$ by

$$\bar{\boldsymbol{\xi}} = \mathbf{D}(x,y,z)\boldsymbol{\xi} = \begin{pmatrix}\mathbf{d}_{\bar{u}}^\mathrm{T} \\ \mathbf{d}_{\bar{v}}^\mathrm{T} \\ \mathbf{d}_{\bar{w}}^\mathrm{T}\end{pmatrix}\boldsymbol{\xi} \tag{A.29}$$

These components can be written out to obtain

$$\mathbf{d}_{\bar{u}} \equiv \frac{1}{l}\begin{bmatrix} l-x \\ -\frac{6y}{1+\Theta_z}\left(\frac{x^2}{l^2}-\frac{x}{l}\right) \\ \frac{6z}{1+\Theta_y}\left(\frac{x^2}{l^2}-\frac{x}{l}\right) \\ 0 \\ \frac{zl}{1+\Theta_y}\left(-3\frac{x^2}{l^2}+\frac{x}{l}(4+\Theta_y)-1\right) \\ \frac{yl}{1+\Theta_z}\left(-3\frac{x^2}{l^2}+\frac{x}{l}(4+\Theta_y)-1\right) \\ x \\ \frac{6y}{1+\Theta_z}\left(\frac{x^2}{l^2}-\frac{x}{l}\right) \\ -\frac{6z}{1+\Theta_y}\left(\frac{x^2}{l^2}-\frac{x}{l}\right) \\ 0 \\ \frac{zl}{1+\Theta_y}\left(-3\frac{x^2}{l^2}+\frac{x}{l}(2-\Theta_y)\right) \\ \frac{yl}{1+\Theta_z}\left(-3\frac{x^2}{l^2}+\frac{x}{l}(2-\Theta_z)\right) \end{bmatrix} \tag{A.30}$$

$$\mathbf{d}_{\bar{v}} \equiv \frac{1}{1+\Theta_z}\begin{bmatrix} 0 \\ 1+\Theta_z-\Theta_z\frac{x}{l}-3\frac{x^2}{l^2}+2\frac{x^3}{l^3} \\ 0 \\ -z(1+\Theta_z)(1-\frac{x}{l}) \\ 0 \\ \frac{2+\Theta_z}{2}x-\frac{4+\Theta_z}{2l}x^2+\frac{1}{l^2}x^3 \\ 0 \\ \Theta_z\frac{x}{l}+3\frac{x^2}{l^2}-2\frac{x^3}{l^3} \\ 0 \\ -z(1+\Theta_z)\frac{x}{l} \\ 0 \\ -\frac{1}{2}\Theta_z x-\frac{2-\Theta_z}{2l}x^2+\frac{x^3}{l} \end{bmatrix} \tag{A.31}$$

$$\mathbf{d}_{\bar{w}} \equiv \frac{1}{1+\Theta_y}\begin{bmatrix} 0 \\ 0 \\ 1+\Theta_y-\Theta_y\frac{x}{l}-3\frac{x^2}{l^2}+2\frac{x^3}{l^3} \\ y(1+\Theta_y)(1-\frac{x}{l}) \\ -\frac{2+\Theta_y}{2}x+\frac{4+\Theta_y}{2l}x^2-\frac{1}{l^2}x^3 \\ 0 \\ 0 \\ 0 \\ \Theta_y\frac{x}{l}+3\frac{x^2}{l^2}-2\frac{x^3}{l^3} \\ y(1+\Theta_y)\frac{x}{l} \\ \frac{1}{2}\Theta_y x+\frac{2-\Theta_y}{2l}x^2-\frac{x^3}{l} \\ 0 \end{bmatrix} \tag{A.32}$$

It then follows that the element mass matrix is found by Przemieniecki (1968) as

$$\mathbf{M}_{\mathrm{e}} \equiv \rho \int_V \mathbf{D}^{\mathrm{T}}\mathbf{D}\,\mathrm{d}V \tag{A.33}$$

Where ρ is the density of the material. The resulting element mass matrix $\mathbf{M}_{\mathrm{e}}$ is a combination of translation and rotary inertia,

$$\mathbf{M}_{\mathrm{e}} = \mathbf{M}_{\mathrm{e,tra}} + \mathbf{M}_{\mathrm{e,rot}} \tag{A.34}$$

where the translational inertia $\mathbf{M}_{\mathrm{e,tra}}$ is given as

$$
\mathbf{M}_{\mathrm{e,tra}} = \rho A l
\begin{bmatrix}
\frac{1}{3} & 0 & 0 & 0 & 0 & 0 & \frac{1}{6} & 0 & 0 & 0 & 0 & 0 \\
 & \frac{13}{35}+\frac{7}{10}\Theta_z+\frac{1}{3}\Theta_z^2}{(1+\Theta_z)^2} & 0 & 0 & 0 & 0 & \frac{9}{70}+\frac{3}{10}\Theta_z+\frac{1}{6}\Theta_z^2}{(1+\Theta_z)^2} & 0 & 0 & 0 & 0 & -\frac{\left(\frac{13}{420}+\frac{3}{40}\Theta_z+\frac{1}{24}\Theta_z^2\right)L}{(1+\Theta_z)^2} \\
 & & \frac{13}{35}+\frac{7}{10}\Theta_y+\frac{1}{3}\Theta_y^2}{(1+\Theta_y)^2} & 0 & 0 & 0 & 0 & \frac{9}{70}+\frac{3}{10}\Theta_y+\frac{1}{6}\Theta_y^2}{(1+\Theta_y)^2} & 0 & 0 & \frac{\left(\frac{13}{420}+\frac{3}{40}\Theta_y+\frac{1}{24}\Theta_y^2\right)L}{(1+\Theta_y)^2} & 0 \\
 & & & \frac{j}{3A} & 0 & 0 & 0 & 0 & -\frac{j}{6A} & 0 & 0 & 0 \\
 & & & & \frac{\left(\frac{1}{105}+\frac{1}{60}\Theta_y+\frac{1}{120}\Theta_y^2\right)I^2}{(1+\Theta_y)^2} & -\frac{\left(\frac{11}{210}+\frac{11}{120}\Theta_y+\frac{1}{24}\Theta_y^2\right)L}{(1+\Theta_y)^2} & 0 & -\frac{\left(\frac{13}{420}+\frac{3}{40}\Theta_y+\frac{1}{24}\Theta_y^2\right)L}{(1+\Theta_y)^2} & 0 & -\frac{\left(\frac{1}{140}+\frac{1}{60}\Theta_y+\frac{1}{120}\Theta_y^2\right)I^2}{(1+\Theta_y)^2} & 0 & 0 \\
 & & & & & \frac{\left(\frac{1}{105}+\frac{1}{60}\Theta_z+\frac{1}{120}\Theta_z^2\right)I^2}{(1+\Theta_z)^2} & 0 & \frac{\left(\frac{13}{420}+\frac{3}{40}\Theta_z+\frac{1}{24}\Theta_z^2\right)L}{(1+\Theta_z)^2} & 0 & 0 & -\frac{\left(\frac{1}{140}+\frac{1}{60}\Theta_z+\frac{1}{120}\Theta_z^2\right)I^2}{(1+\Theta_z)^2} & 0 \\
 & & & & & & \frac{1}{3} & 0 & 0 & 0 & 0 & 0 \\
 & & & & & & & \frac{13}{35}+\frac{7}{10}\Theta_z+\frac{1}{3}\Theta_z^2}{(1+\Theta_z)^2} & 0 & 0 & 0 & 0 \\
 & & & & & & & & \frac{13}{35}+\frac{7}{10}\Theta_y+\frac{1}{3}\Theta_y^2}{(1+\Theta_y)^2} & 0 & \frac{\left(\frac{11}{210}+\frac{11}{120}\Theta_y+\frac{1}{24}\Theta_y^2\right)L}{(1+\Theta_y)^2} & 0 \\
 & & & & & & & & & \frac{j}{3A} & 0 & 0 \\
 & & & & & & & & & & \frac{\left(\frac{1}{105}+\frac{1}{60}\Theta_y+\frac{1}{120}\Theta_y^2\right)I^2}{(1+\Theta_y)^2} & 0 \\
 & & & & & & & & & & & \frac{\left(\frac{1}{105}+\frac{1}{60}\Theta_z+\frac{1}{120}\Theta_z^2\right)I^2}{(1+\Theta_z)^2}
\end{bmatrix}
\quad \text{(A.35)}
$$

sym

and the rotary inertia $\mathbf{M}_{\mathrm{e,rot}}$ is given as

$$\mathbf{M}_{\mathrm{e,rot}} = \rho A l \begin{bmatrix}
0 & 0 & 0 & 0 & 0 & 0 & 0 & 0 & 0 & 0 & 0 & 0 \\
 & \frac{\frac{6}{5}}{(1+\Theta_z)^2}\frac{I_z}{Al^2} & 0 & 0 & 0 & \frac{\left(\frac{1}{10}-\frac{1}{2}\Theta_z\right)L}{(1+\Theta_z)^2}\frac{I_z}{Al^2} & 0 & \frac{-\frac{6}{5}}{(1+\Theta_z)^2}\frac{I_z}{Al^2} & 0 & 0 & 0 & \frac{\left(\frac{1}{10}-\frac{1}{2}\Theta_z\right)L}{(1+\Theta_z)^2}\frac{I_z}{Al^2} \\
 & & \frac{\frac{6}{5}}{(1+\Theta_y)^2}\frac{I_y}{Al^2} & 0 & \frac{-\left(\frac{1}{10}-\frac{1}{2}\Theta_y\right)L}{(1+\Theta_y)^2}\frac{I_y}{Al^2} & 0 & 0 & 0 & \frac{-\frac{6}{5}}{(1+\Theta_y)^2}\frac{I_y}{Al^2} & 0 & \frac{-\left(\frac{1}{10}-\frac{1}{2}\Theta_y\right)L}{(1+\Theta_y)^2}\frac{I_y}{Al^2} & 0 \\
 & & & 0 & 0 & 0 & 0 & 0 & 0 & 0 & 0 & 0 \\
 & & & & \frac{\left(\frac{2}{15}+\frac{1}{6}\Theta_y+\frac{1}{3}\Theta_y^2\right)l^2}{(1+\Theta_y)^2}\frac{I_y}{Al^2} & 0 & 0 & 0 & \frac{\left(\frac{1}{10}-\frac{1}{2}\Theta_y\right)L}{(1+\Theta_y)^2}\frac{I_y}{Al^2} & 0 & \frac{\left(-\frac{1}{30}-\frac{1}{6}\Theta_y+\frac{1}{6}\Theta_y^2\right)l^2}{(1+\Theta_y)^2}\frac{I_y}{Al^2} & 0 \\
 & & & & & \frac{\left(\frac{2}{15}+\frac{1}{6}\Theta_z+\frac{1}{3}\Theta_z^2\right)l^2}{(1+\Theta_z)^2}\frac{I_z}{Al^2} & 0 & \frac{-\left(\frac{1}{10}-\frac{1}{2}\Theta_y\right)L}{(1+\Theta_z)^2}\frac{I_z}{Al^2} & 0 & 0 & 0 & \frac{\left(-\frac{1}{30}-\frac{1}{6}\Theta_z+\frac{1}{6}\Theta_z^2\right)l^2}{(1+\Theta_z)^2}\frac{I_z}{Al^2} \\
 & & & & & & 0 & 0 & 0 & 0 & 0 & 0 \\
 & & & & & & & \frac{\frac{6}{5}}{(1+\Theta_z)^2}\frac{I_z}{Al^2} & 0 & 0 & 0 & \frac{-\left(\frac{1}{10}-\frac{1}{2}\Theta_z\right)L}{(1+\Theta_z)^2}\frac{I_z}{Al^2} \\
 & & & & & & & & \frac{\frac{6}{5}}{(1+\Theta_y)^2}\frac{I_y}{Al^2} & 0 & \frac{\left(\frac{1}{10}-\frac{1}{2}\Theta_y\right)L}{(1+\Theta_y)^2}\frac{I_y}{Al^2} & 0 \\
 & & & & & & & & & 0 & 0 & 0 \\
 & \text{sym} & & & & & & & & & \frac{\left(\frac{2}{15}+\frac{1}{6}\Theta_y+\frac{1}{3}\Theta_y^2\right)l^2}{(1+\Theta_y)^2}\frac{I_y}{Al^2} & 0 \\
 & & & & & & & & & & & \frac{\left(\frac{2}{15}+\frac{1}{6}\Theta_z+\frac{1}{3}\Theta_z^2\right)l^2}{(1+\Theta_z)^2}\frac{I_z}{Al^2}
\end{bmatrix} \tag{A.36}$$

appendix B

Model methodology

This appendix chapter provides insight into the methodology; how has the simulation model *Salacia* been developed. First Section B.1 addresses the philosophy behind the model: which approach has been adopted to reach the final model, what are the governing equations of the model and how are the parameters defined. Secondly, Section B.2 addresses the programs used in the simulation model. Section B.3 describes the simulation procedure.

B.1 | Modelling philosophy

The modelling philosophy describes the thoughts behind the development of the model: what approach is taken to go from zero lines of code to a fully working model, how are the governing equations programmed in the code, how is it structured and which packages are used?

An iterative modelling approach

This section has been removed as it contains confidential information provided by the research partner GustoMSC

The mathematical formulation of the governing equations

The model is written with coupled ordinary differential equations (ODEs) described in Chapter 5. Both linear and non-linear ODEs are found in the code: for example, linear ODEs describe the displacements, velocities and forces of structural components, such as the legs or pinions, and non-linear ODEs describe the currents in the induction motors. Within the code, all of these ODEs have been fully vectorised to reduce computational time.

The solution algorithm to integrate the equation of motion

These ODEs are solved in the time-domain by numerical time-integration. The integration scheme used is the Runge-Kutta 45 method. This method is an explicit method and ensures stability for stiff systems, by automatically adopting a suitable time step (SciPy Developers, n.d.).

The parametrisation of the model

The model is parametrised such that multiple geometrical designs, induction machines or environmental parameters can be considered and simulated. This means that if the value of one parameter is changed, say the mass of the hull or the period of incident waves, the results will be different. The model has been almost fully parametrised in the sense that certain constraints are still present: e.g. the shape of the hull, the type of machines driving the jacking systems or the general design of the legs cannot changed, but their characteristic values can, e.g. the mass of the hull, the power of the machines or the dimensions of the legs.

B.2 | The software of the simulation model

This section provides a description of the software and Python packages used in the simulation model, as well as how the code is structured.

The programming language, packages and software used

One of the key characteristics of this model is that the simulation is executed within the same environment: Python. During simulation, even when changing the values of parameters, no external software is required to obtain certain values; all is processed within. For example, the hydrodynamics of the hull are evaluated within the Python code, rather than using an external tool such as WAMIT or NEMOH. External FE software,

however, has been used during development to assess certain relations in the rack-and-pinion interface and the spudcan-and-seabed interface, but these models have been normalised (unit loads and stiffness) and are scaled accordingly within Python. In Table B.1 and Table B.2, the programs and Python packages used, their versions and purpose are presented.

Table B.1: Overview of software used.

Program	Version	Purpose
Python	3.8.16	primary programming language
Spyder	5.4.1	ide for Python
Abaqus	6.12-1	FE-software used for spudcan-and-seabed interface
Ansys APDL	2022 R2	FE-software used for rack-and-pinion interface and validation of internal FE-model
WAMIT	7.311	validation of internal hydrodynamic model

Table B.2: Overview of Python packages used.

Python package	Version	Purpose
Numpy	1.23.5	math, linear algebra
Matplotlib	3.7.0	creating figures and animations
Scipy	1.10.0	numerical time-integration
Capytaine	1.5	hydrostatics and hydrodynamics
vtk	9.0.3	auxiliary package to Capytaine
xarray	2022.11.0	auxiliary package to Capytaine

The structure of the Python code

The code of the model has been divided into multiple files and folders to keep the code structured and easy to use. For a certain build the structure is as follows,

```
Build 0.xx.xx
├── output
├── salacia
│   ├── seabed penetration curves
│   │   ├── seabedHorizontal.csv
│   │   ├── seabedRotational.csv
│   │   └── seabedVertical.csv
│   ├── __init__.py
│   ├── config.py
│   ├── geometrybuilder.py
│   ├── neptunus.py
│   └── triton.py
├── animator.py
├── config.ini
├── solver.py
└── visualiser.py
```

The root folder contains three executable Python files and a configuration file. Executing `solver.py` runs the simulation according to the configuration of parameters as provided in `config.ini`. It is dependent on three files: `config.py` loads `config.ini` into Python and checks the parameters for validity, `geometrybuilder.py` performs time-independent calculations (creation of matrices, calculation of hydrodynamic parameters etc.) and `triton.py` performs time-dependent calculations, which is the time-integration. When it is finished running the simulation, the parameters and simulation data are saved to the `output` folder with a unique identifier—the number of seconds since 1 January 1970 00:00:00. The other two files, `visualiser.py` and `animator.py`, take

as input this unique identifier and consequently produce figures and a 3D animation of the data respectively and are dependent on the `neptunus.py` file. The flowchart found in Figure B.1 presents the structure of the code.

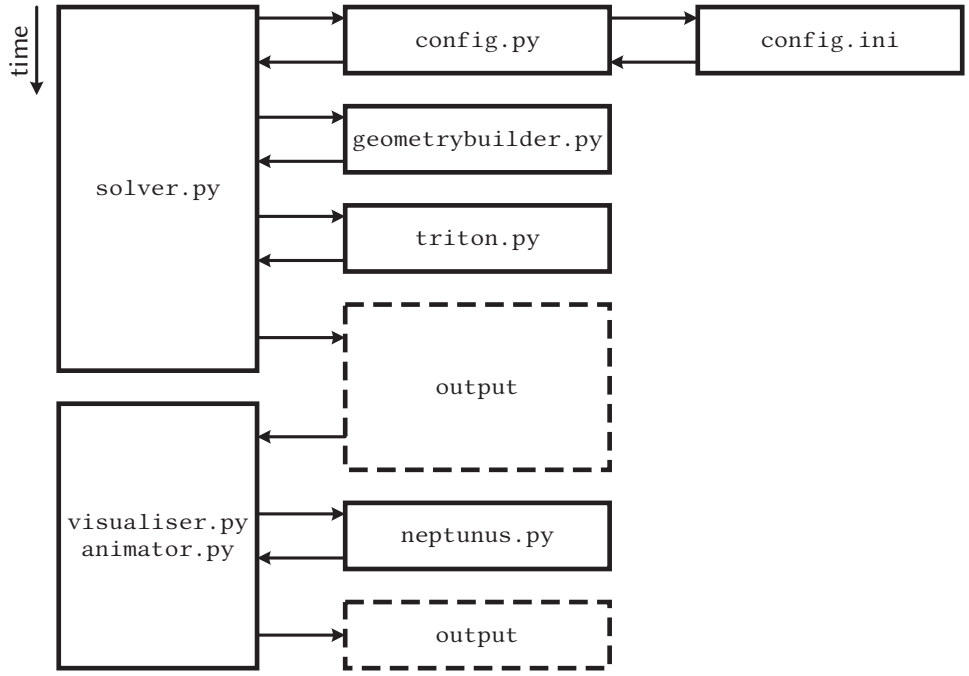

Figure B.1: Structure and flow of the Python code of the model.

B.3 | Running the simulation

This section provides insight into what steps occurs between configuring the simulation with `config.ini` and plotting the results with `visualiser.py`.

Additional settings affecting the simulation procudure

The first step is to configure the configuration file. Besides the parameters listed extensively throughout Chapter 5, additional configurations are available that affect how to simulation is solved. These settings are given in Table B.3.

Table B.3: Overview of settings for the simulation procedure.

Setting	Type	Clarification
`simulationDuration`	Float	Simulation starts at $t = 0$, ends at this time
`simulationUseConsistentMassMethod`	Bool	If `False`, lumped mass method used
`simulationAllowRotaryInertia`	Bool	Rotary inertia effects in consistent mass method
`simulationAllowShear`	Bool	Shear effects in stiffness and consistent mass matrix
`simulationLegHandlingVelocity`	Float	Velocity objective of the control system
`simulationAllowWaveOscillations`	Bool	If `False`, still water used
`simulationStructuralDampingRatio`	Float	Default value of 2 % used

The load case evaluated during simulation

The load case that is simulated with the model is that of leg lowering including the transient phase of spudcan penetration into the seabed. This is the first load case that occurs when a WTIV arrives at a location, as schematised in Figure 1.3. To prevent unnecessary computations into leg lowering without any spudcan penetration, the simulation starts with a vertical clearance $\Delta z_{\text{spudcan}}$ as described in Section 5.2.3. The simulation continues until the given simulation duration as given in `config.ini` is reached. Because the equations of the model describe all dynamics of WTIVs generally, the simulation can switch to the platform lifting load case if a sufficiently large

simulation duration is given as input. These results will not be accurate, as such load cases are generally modelled with a different spudcan-and-seabed model, as described in Section 3.2.4.1, and because the hydrodynamics and wave-exciting forces are calculated for the initial draught.

Besides the leg lowering load case, the simulation model would also allow to simulate the load case of leg lifting (see Figure 1.3) as this does not involve the spudcan-and-seabed model. Though, this is not considered in this thesis.

The initial conditions

This section has been removed as it contains confidential information provided by the research partner GustoMSC

The simulation procedure

This section has been removed as it contains confidential information provided by the research partner GustoMSC

appendix C

Validation of the model

It is important that every addition or change to the model is validated, before moving to the next build. However, as the model created in this thesis is first-of-its-kind, it is not straightforward to perform validation as no single equivalent software exists with similar capabilities. Validation of the entire model must therefore be performed differently. One method is to validate the sub-models of the model separately with equivalent software or literature, such as an existing FE-software package to validate the FE-model of the legs. An overview of validation methods of the sub-models is found in Table C.1.

Table C.1: Overview of the validation methods of sub-models.

Sub-model	Validation method
Internal FE-model of the legs	Validated with existing software (Ansys)
Induction motor model	Validated using theory reference and data sheets
Internal hydrodynamic model	Validated using existing software (WAMIT)

C.1 | Validation of the internal FE model

The internal FE model of the leg is validated using the well-established FE solver Ansys APDL. Two levels of validation are distinguished. In the first level the element mass and stiffness matrices from Sections 2.3 and 2.4 are validated and in the second level the procedure to represent a structure with multiple beam elements from Section 2.7 is validated.

C.1.1 ‖ Validation of the element mass and element stiffness matrices

In the first level the mass and stiffness matrices of a single beam element are exported from Ansys and compared to the element mass matrix $\mathbf{M}_e$ and element stiffness matrix $\mathbf{K}_e$ from the internal FE model. Both consistent and lumped mass matrices are checked. The matrices matched perfectly, confirming that the procedure to formulate these matrices is formulated and implemented correctly into Salacia.

C.1.2 ‖ Validation of the procedure to represent a structure with multiple beam elements

This section has been removed as it contains confidential information provided by the research partner GustoMSC

C.2 | Validation of the induction motor model

The induction motor model is validated using data sheets and references. Two levels of validation are distinguished. In the first level the formulation and implementation of the EOM of the induction motor is validated and in the second level the procedure of parameter estimation is validated.

C.2.1 ‖ Validation of the equation of motion of the induction motor

In the first level the EOM of the induction motor is validated: are the currents, rotational frequency and response to loads the same as found in reference? An example of a 2250 horsepower induction motor from Krause et al. (2013) is used in the validation. The results are shown in Figures C.1–C.5 showing both the acceleration characteristics as well as response to an external load. The parameters of the induction motor used by Krause et

al. (2013) are listed in Table C.2. The results of the induction motor model developed here, match those found in reference. This confirms the equations for the induction motor are formulated and implemented correctly in the simulation model.

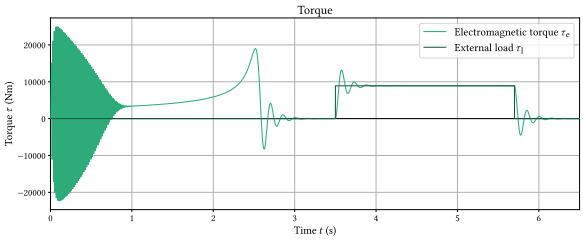

Figure C.1: Electromagnetic torque generated by the induction motor, and the external load.

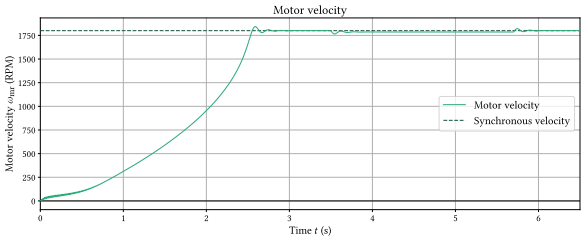

Figure C.2: Motor velocity in rpm. Slight drop in velocity visible due to the external load.

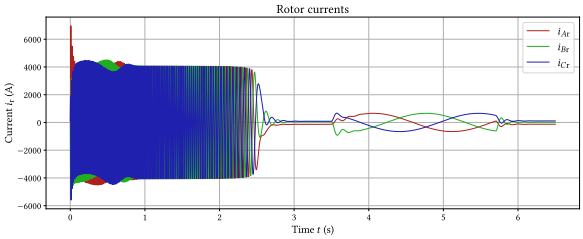

Figure C.3: Currents in the rotor.

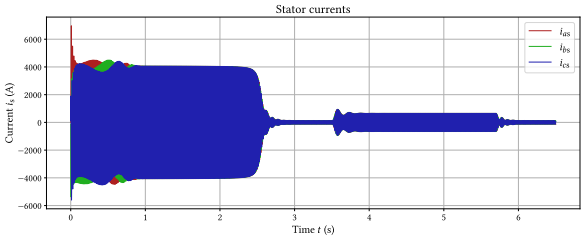

Figure C.4: Currents in the stator.

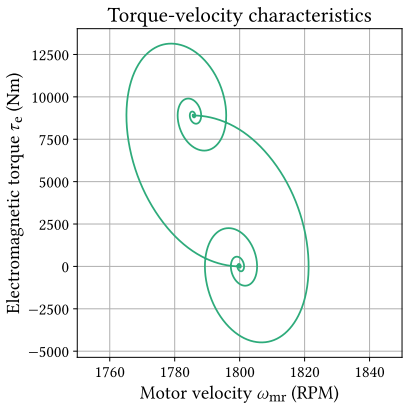

Figure C.5: Torque-velocity characteristics during the change in external load.

Table C.2: Induction motor parameters (Krause et al., 2013).

Quantity	Symbol	Value
Rotor mass moment of inertia	j_r	63.87 kg m^2
Number of poles	p	4
Rated voltage frequency	ω_e	60 Hz
Line-to-neutral voltage	v_{DC}	1837 V
Rotor resistance	R_r	22 mΩ
Stator resistance	R_s	29 mΩ
Rotor inductance	L_r	35.2 mH
Stator inductance	L_s	35.2 mH
Mutual inductance	L_m	34.5 mH

C.2.2 ‖ Validation of the induction motor parameters

This section has been removed as it contains confidential information provided by the research partner GustoMSC

C.3 | Validation of the internal BEM model

In the simulation model, the hydrostatics, hydrodynamics and wave-exciting forces of the hull are evaluated with the `Capytaine` package. The same geometry is created with commercial BEM solver WAMIT in order to validate this implementation. In Figures C.6–C.8 the diagonal terms of the added mass matrix $\mathbf{M}_h$, the diagonal terms of the damping matrix $\mathbf{C}_h$ and the amplitudes of the wave-exciting forces $\mathbf{f}_h$ are presented as function of the angular frequency of the waves ω_h. It can be seen that the convergence is excellent, confirming the `Capytaine` package has been implemented correctly.

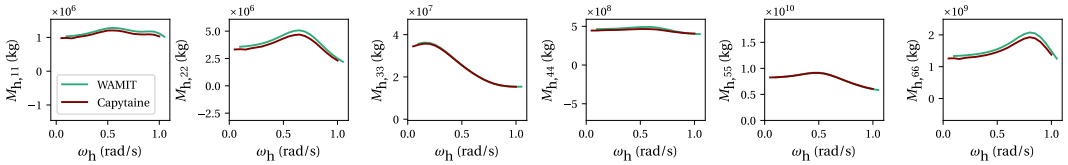

Figure C.6: Diagonal terms of the added mass matrix $\mathbf{M}_h$.

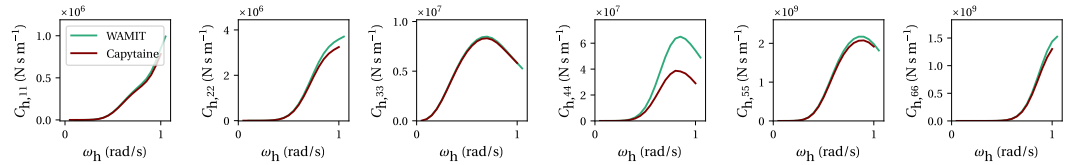

Figure C.7: Diagonal terms of the damping matrix $\mathbf{C}_h$.

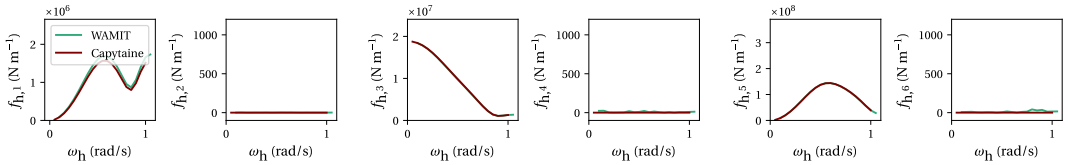

Figure C.8: Wave-exciting force amplitudes $\mathbf{f}_h$.